

1  
2  
3  
4

# The Arctic Subpolar gyre sTate Estimate (ASTE): Description and assessment of a data-constrained, dynamically consistent ocean-sea ice estimate for 2002–2017

5  
6

An T. Nguyen<sup>1\*</sup>, Helen Pillar<sup>1</sup>, Victor Ocaña<sup>1</sup>, Arash Bigdeli<sup>1</sup>, Timothy A. Smith<sup>1</sup>, Patrick Heimbach<sup>1,2,3</sup>

7  
8  
9

<sup>1</sup>Oden Institute for Computational Engineering and Sciences, University of Texas at Austin  
<sup>2</sup>Jackson School of Geosciences, University of Texas at Austin  
<sup>3</sup>Institute for Geophysics, University of Texas at Austin

10

## Key Points:

11  
12  
13  
14  
15  
16

- The 2002–2017 medium-resolution Arctic Subpolar gyre sTate Estimate (ASTE) is constrained to 10<sup>9</sup> satellite and in situ observations.
- Strict adherence to conservation laws ensures all sources/sinks can be accounted for, enabling application for meaningful budget analyses.
- ASTE captures the large-scale dynamics of the Arctic ocean-sea ice system including variability and trends in heat and freshwater storage.

---

\*Oden Institute for Computational Engineering and Sciences  
The University of Texas at Austin  
201 East 24th St., POB 4.234, C0200, Austin, TX, 78712, USA

Corresponding author: An T. Nguyen, [atnguyen@oden.utexas.edu](mailto:atnguyen@oden.utexas.edu)

**Abstract**

A description and assessment of the first release of the Arctic Subpolar gyre state Estimate (*ASTE\_R1*), a data-constrained ocean-sea ice model-data synthesis, is presented. *ASTE\_R1* has a nominal resolution of  $1/3^\circ$  and spans the period 2002-2017. The fit of the model to an extensive ( $O(10^9)$ ) set of satellite and in situ observations was achieved through adjoint-based nonlinear least-squares optimization. The improvement of the solution compared to an unconstrained simulation is reflected in misfit reductions of 77% for Argo, 50% for satellite sea surface height, 58% for the Fram Strait mooring, 65% for Ice Tethered Profilers, and 83% for sea ice extent. Exact dynamical and kinematic consistency is a key advantage of *ASTE\_R1*, distinguishing the state estimate from existing ocean reanalyses. Through strict adherence to conservation laws, all sources and sinks within *ASTE\_R1* can be accounted for, permitting meaningful analysis of closed budgets at the grid-scale, such as contributions of horizontal and vertical convergence to the tendencies of heat and salt. *ASTE\_R1* thus serves as the biggest effort undertaken to date of producing a specialized Arctic ocean-ice estimate over the 21st century. Transports of volume, heat, and freshwater are consistent with published observation-based estimates across important Arctic Mediterranean gateways. Interannual variability and low frequency trends of freshwater and heat content are well represented in the Barents Sea, western Arctic halocline, and east subpolar North Atlantic. Systematic biases remain in *ASTE\_R1*, including a warm bias in the Atlantic Water layer in the Arctic and deficient freshwater inputs from rivers and Greenland discharge.

**Plain Language Summary**

A 2002–2017 ocean-sea ice reconstruction, *ASTE\_R1*, is distributed for use in climate studies over the early 21st century in the northern high latitudes. The product is a model-data synthesis, using a numerical model to interpolate approximately a billion satellite and in situ observations. The primary strength of *ASTE\_R1* compared to most existing ocean reanalyses is that strict adherence to the equations describing the fluid flow and conservation laws is built into the product, thus making *ASTE\_R1* free from artificial un-physical sources or sinks and associated “jumps” in the time-evolving state. Furthermore, the product is consistent with most available observations, both used in the synthesis and retained for independent verification. This indicates good large-scale representation of evolving sea-ice, ocean currents and water properties, including year-to-year variability and decadal trends in heat and freshwater storage in the Arctic and subpolar North Atlantic. Some systematic data-model differences remain in the product and highlight where extra data and/or model development will improve the next release. The product and underlying model configuration are freely available to the research community.

**1 Introduction**

The Arctic region has experienced large changes in recent decades. These include near-surface air temperature warming at twice the global rate (Richter-Menge & Jeffries, 2011), rapid decline in multi-year sea ice (Kwok & Cunningham, 2015), enhanced solar radiation absorption in the Western Arctic upper ocean (Timmermans et al., 2018), increased river and glacial discharge (Bamber et al., 2012, 2018; Proshutinsky et al., 2020), and increased influxes of freshwater from the Pacific (Woodgate, 2018) and heat from the Atlantic (Polyakov et al., 2011). Many of these changes have been suggested to trigger positive feedbacks. Enhanced shortwave absorption (Jackson et al., 2010; Perovich et al., 2011; Timmermans et al., 2018), enhanced air-ice-sea momentum transfer (Rainville & Woodgate, 2009; Martin et al., 2014), shoaling of the Atlantic Water layer (Polyakov et al., 2017, 2020), and enhanced heat flux through Fram Strait (Q. Wang et al., 2020) have all been identified to both result from and further amplify sea-ice thinning.

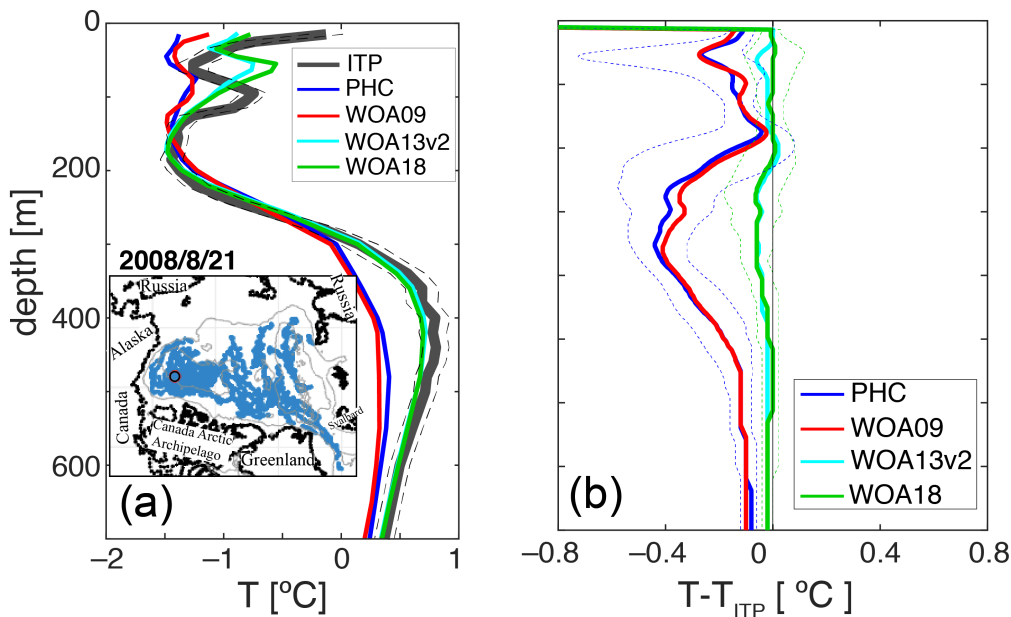


**Figure 1.** Comparison between ITP-derived temperature and the climatologies from the Polar Hydrography Center (PHC, blue), World Ocean Atlas 2009 (WOA09, red), 2013 version 2 (WOA13v2, cyan), and 2018 (WOA18, green). Panel (a) shows this comparison for a single ITP profile on August 21, 2008 (thick dark gray, with the observational uncertainty shown by the thin dashed black lines). The location of the profile is shown in the inset. Panel (b) shows the 50th percentile difference between all ITP temperature profiles in the Canada Basin and the four climatologies. The dotted lines show the 30th and 70th percentile differences.

67 Some of the recent changes in the observed Arctic Ocean heat content have been  
 68 linked to pulsed warming of the Atlantic Water (AW) inflow (Polyakov et al., 2017; Muil-  
 69 wijk et al., 2018) and can be traced back upstream into the subpolar North Atlantic (SPNA;  
 70 e.g., Årthun & Eldevik, 2016). Given the importance of Arctic changes and their inter-  
 71 action with the SPNA to the global climate system (Carmack et al., 2016), investiga-  
 72 tions of mechanisms setting the time-mean and evolving state of the Arctic Ocean and  
 73 exchanges with surrounding ocean basins must be supported by basin-scale estimates of  
 74 the ocean-sea ice state.

75 Historically, due to extremely sparse observations, efforts to construct decadal Arctic-  
 76 focused gridded datasets have been hampered. Realistic simulation of the Arctic and sub-  
 77 Arctic ocean-sea ice state has remained difficult due to highly uncertain initial condi-  
 78 tions. Beginning in the early 2000s, increased availability of *in situ* observations of sub-  
 79 surface ocean hydrography and of oceanic transports across Arctic gateways has improved  
 80 our understanding of key processes, including interior eddy activity and mixing (Timmermans  
 81 et al., 2012; Cole et al., 2014; Zhao et al., 2016; Bebieva & Timmermans, 2016), and the  
 82 transformation and redistribution of watermasses (Proshutinsky et al., 2009; Rabe et al.,  
 83 2014; Pnyushkov et al., 2015; Timmermans & Jayne, 2016; von Appen et al., 2015a; Polyakov  
 84 et al., 2017; Timmermans et al., 2018). Over the same time period, new satellite altimetry  
 85 (Kwok & Morison, 2016), gravimetry (Peralta-Ferriz et al., 2014), and sea ice observa-  
 86 tions have allowed a more accurate estimate of Ekman transport (Meneghello et al.,  
 87 2018) and inventory of freshwater in the Western Arctic (Proshutinsky et al., 2019, 2020).

88 In parallel with increased observational coverage, great progress has also been made  
89 using theoretical and modeling frameworks to advance our understanding of Arctic Ocean  
90 dynamics, for example, elucidating the importance of eddies in gyre equilibration (Manucharyan  
91 & Isachsen, 2019; Meneghello et al., 2017) and vertical heat redistribution (Polyakov et  
92 al., 2017). Despite this progress, confident assessment of the time-mean state, interan-  
93 nual variability and identification of robust decadal trends remains challenging (Balmaseda  
94 et al., 2015; Timmermans & Marshall, 2020) due to multiple factors (Holloway et al., 2007;  
95 Q. Wang et al., 2016b, 2016a; Ilicak et al., 2016; Docquier et al., 2019). The most im-  
96 portant amongst these factors is the lack of direct observations throughout the full wa-  
97 ter column, including at the air-ice-ocean interface, in and just below the mixed layer,  
98 along the Atlantic Water (AW) boundary current pathway, and at the shelf-basin regions  
99 that connect the dynamics of this energetic current and the relatively quiescent Arctic  
100 Ocean interior (Timmermans & Marshall, 2020).

101 To fill these gaps, the community has constructed climatologies (e.g., WOA13 ver-  
102 sion 2 and WOA18, Locarnini et al., 2018; Zweng et al., 2018) and data-model synthe-  
103 ses (Stammer et al., 2016; Uotila et al., 2019; Carton et al., 2019) which are assumed to  
104 have higher fidelity as the repository of incorporated data grows. The improved fit be-  
105 tween the latest climatology and existing observations is far superior to that seen in older  
106 climatologies. For example, in the Western Arctic interior, Ice Tethered Profilers (ITP)  
107 consistently report warmer temperatures (Fig. 1) than provided by both the Polar Hy-  
108 drographic Climatology (PHC, Steele et al., 2001) and the World Ocean Atlas 2009 (WOA09,  
109 Locarnini et al., 2010; Antonov et al., 2010), but are in close agreement with WOA18.  
110 Here it is important to note that this close agreement at the time/location of data ac-  
111 quisition is built into the majority of these climatologies and other existing Arctic model-  
112 data syntheses. These products are constructed using statistical methods such as opti-  
113 mal interpolation (e.g., PHC, WOA), 3D-Var, or sequential 4D-Var with short assim-  
114 ilation windows (Stammer et al., 2016; Uotila et al., 2019; Mu et al., 2018; Carton et al.,  
115 2019). The advantage of these methods is that the synthesis ensures a local fit to avail-  
116 able observations (Fig. 1, Carton et al., 2019). Away from observed locations, however,  
117 the interpolator relies on incomplete, unavailable or unobtainable information. Missing  
118 values are, for example, determined via spatial/temporal correlations, potentially derived  
119 from regions/times of very different dynamics. By construction, high frequency variabil-  
120 ity cannot be fully accounted for and as a result spectral agreement with observations  
121 can be poor (Verdy et al., 2017). Importantly, this type of interpolation – and that used  
122 in 3D-Var or sequential 4D-Var – can introduce artificial sources/sinks (e.g., of mass, en-  
123 thalpy and momentum, Wunsch & Heimbach, 2013; Griffies et al., 2014; Stammer et al.,  
124 2016), which make a large contribution to the total energy budget (Balmaseda et al., 2015).  
125 This violation of basic conservation principles has been shown to obfuscate the use of  
126 these products for robust identification and attribution of change, creating spurious trends  
127 (Bengtsson et al., 2004), and triggering artificial loss of balance (Pilo et al., 2018), re-  
128 sulting in adjustments that may propagate and amplify to corrupt the large scale solu-  
129 tion (Sivareddy et al., 2017).

130 To lend additional support to studies of the Arctic ocean-sea ice system over the  
131 early 21st century we have developed a new model-data synthesis utilizing the non-linear  
132 inverse modeling framework developed within the consortium for Estimating the Circu-  
133 lation and Climate of the Ocean (ECCO, Stammer et al., 2002; Wunsch & Heimbach,  
134 2007; Heimbach et al., 2019). The use of the primitive equations as a dynamical inter-  
135 polator distinguishes our effort from purely statistical approaches. The inversion con-  
136 sists of an iterative, gradient-based minimization of a least-squares model-data misfit func-  
137 tion. Unlike most reanalysis products that are based on sequential data assimilation, only  
138 independent, uncertain input variables, i.e. initial conditions, surface boundary condi-  
139 tions and model parameters are adjusted. No periodic analysis increments during the  
140 estimation period that would incur artificial sources or sinks are permitted. Through strict  
141 adherence to conservation laws, all sources and sinks within the state estimate can be

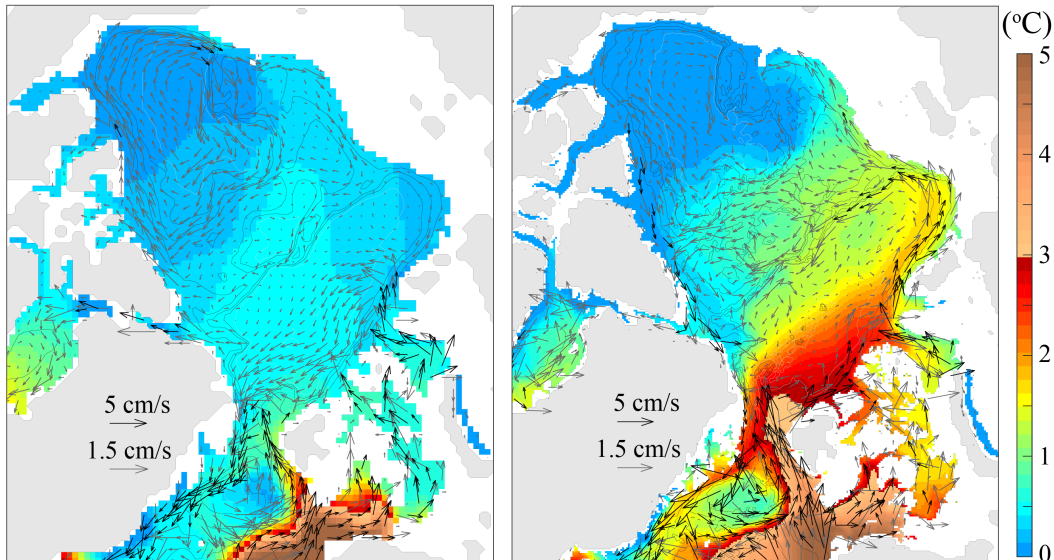


**Figure 2.** 2002–2015 mean circulation in the Arctic at depth 250 m as represented in ECCOv4r3 (left, averaged over 2x2 grids) and *ASTER1* (right, averaged over 6x6 grids). The color scale shows temperature at the same depth from the two solutions. Vector arrows are grouped into speed ranges of [0–1.5] cm/s (gray) and [1.5–5] cm/s (black), with the vector length scales provided.

142 accounted for over the full estimation period, permitting meaningful analysis of closed  
 143 budgets (Buckley et al., 2014; Piecuch & Ponte, 2012).

144 Our work builds upon extensive prior efforts of the ECCO community to produce  
 145 optimal (in a least-squares sense) kinematically- and dynamically-consistent data-constrained  
 146 estimates of the ocean state across the globe and in various regional domains. Among  
 147 the publicly available ECCO state estimates is ECCO Version 4 Release 3 (ECCOv4r3,  
 148 Forget et al., 2015a; Fukumori et al., 2018a), which has been constrained to satellite and  
 149 in situ data (including Argo and elephant seal data) outside of the Arctic, ITP data in  
 150 the Arctic, and other mooring data at important Arctic gateways. The ECCOv4 releases  
 151 have been widely used, with applications including investigation of global vertical heat  
 152 and salt redistribution (Liang et al., 2017; Liu et al., 2019), heat budgets in the North  
 153 Atlantic (Buckley et al., 2014, 2015; Piecuch et al., 2017; Foukal & Lozier, 2018) and the  
 154 Nordic Seas (Asbjørnsen et al., 2019), high-latitude freshwater budgets (Tesdal & Haine,  
 155 2020), and sea level change (Piecuch & Ponte, 2013).

156 The state-estimation procedure entails reducing the total time- and space-integrated  
 157 model-data misfit. Since ECCOv4r3 is a global solution, reduction of the relatively well-  
 158 sampled misfit at lower latitudes dominates the production of this solution. As a result,  
 159 ECCOv4r3 possesses notable biases in the Arctic (Carton et al., 2019; Tesdal & Haine,  
 160 2020), including a strong anticyclonic circumpolar circulation of Atlantic Water (Fig. 2).  
 161 Furthermore, the ECCOv4r3 horizontal grid spacing of 40–45 km is well above the Rossby  
 162 deformation radius in the Arctic and Nordic Seas (Nurser & Bacon, 2014). This has moti-  
 163 vated a dedicated effort to build a higher resolution regional state estimate for use in  
 164 Arctic inter-annual to decadal climate research, covering the early 21st century, culmi-  
 165 nating in the Arctic Subpolar gyre sTate Estimate (*ASTE*).

166 Here we describe the first release of *ASTE* (*ASTER1*), providing an estimate of  
 167 the ocean-sea ice state for the period 2002–2017. We describe the model configuration,

168 observational constraints and the state estimation machinery (section 2) and present the  
 169 model-data misfit reduction (section 3). We then compare our estimates of volume, heat  
 170 and freshwater transports through important Arctic gateways with those in the exist-  
 171 ing literature as well as present an analysis of *ASTE\_R1* heat and freshwater budgets  
 172 for the Arctic Ocean, Greenland-Iceland-Norwegian (GIN) Seas and subpolar North At-  
 173 lantic (section 4). In section 5 we examine how an improved fit is achieved, identifying  
 174 key adjustments of our independent control variables, and review remaining issues in *ASTE\_R1*  
 175 . In section 6 we summarize key findings and discuss future directions.

## 176 2 Methodology

### 177 2.1 Model Description

178 The coupled ocean-sea ice model underlying the estimation framework is an evolved  
 179 version of the Massachusetts Institute of Technology general circulation model (MIT-  
 180 gcm; Marshall et al., 1997; Adcroft et al., 2018). The model solves the primitive equa-  
 181 tions in rescaled  $z^*$  coordinates (Adcroft & Campin, 2004) with a full non-linear free sur-  
 182 face (Campin et al., 2004). The dynamic-thermodynamic sea ice model is an evolved ver-  
 183 sion of Menemenlis et al. (2005); Losch et al. (2010); Heimbach et al. (2010). Eddy-induced  
 184 tracer mixing and transports along isopycnal surfaces are parameterized following Redi  
 185 (1982); Gent and McWilliams (1990).

186 The model uses a finite-volume discretization in a so-called “latitude-longitude-polar-  
 187 cap” grid configuration (LLC grid, Forget et al., 2015a). The LLC grid is topologically  
 188 equivalent to a cubed-sphere grid (Adcroft et al., 2004), but reverts to a regular latitude-  
 189 longitude grid equatorward of  $\sim 57^\circ\text{N}$ . The computational cost associated with solving  
 190 the non-linear optimization problem for eddy-resolving simulations, which would require  
 191 resolutions well below 4–15 km for the Arctic Mediterranean (Nurser & Bacon, 2014),  
 192 is prohibitively high. As a compromise, *ASTE* is based on the medium-resolution LLC-  
 193 270 grid, providing a nominal grid spacing of  $1/3^\circ$ , which corresponds to  $\sim 22$  km in the  
 194 North Atlantic,  $\sim 16$  km in the Nordic Seas, and  $\sim 14$  km in the high Arctic interior (Fig 3).

195 The *ASTE* domain covers the entire Atlantic northward of  $32.5^\circ\text{S}$ , the entire Arctic  
 196 and its surrounding seas (Labrador, Nordic, Barents, Bering north of  $47.5^\circ\text{N}$ ) and the  
 197 Canadian Archipelago. The model has 50 unevenly spaced vertical height levels; thick-  
 198 nesses range from 10 m at the surface to 500 m at 5000 m depth. The 10 m thickness  
 199 at the surface cannot fully resolve surface boundary layer processes or the shallowest sum-  
 200 mer mixed layer of  $\sim 5$  m, but is deemed sufficient for capturing the 10–100 m seasonal  
 201 MLD in the Arctic (Rudels et al., 2004; Rudels, 2015; Peralta-Ferriz & Woodgate, 2015;  
 202 Bigdeli et al., 2017) and is a reasonable choice given the size and expense of our com-  
 203 putations. Partial cells (Adcroft et al., 1997) are used to improve the representation of  
 204 topography. The domain has boundaries at  $35^\circ\text{S}$  in the South Atlantic,  $48.6^\circ\text{N}$  in the  
 205 Pacific, and at the Gibraltar Strait. Rationales for choosing a full Atlantic-Arctic do-  
 206 main for *ASTE* – rather than limiting it to the Arctic Mediterranean – are to extend the  
 207 applicability of the solution to investigation of latitudinal connectivity between Atlantic  
 208 and Arctic variability on decadal timescales, and to displace the imposed open bound-  
 209 ary conditions far from the region of key interest.

210 We prescribe lateral open boundary conditions from the global ECCOV4r3 solu-  
 211 tion, which has been shown to be in good agreement with large-scale constraints from  
 212 satellite and in situ data (including Argo). The bathymetry is a merged version of W. Smith  
 213 and Sandwell (1997), version 14.1, below  $60^\circ\text{N}$  and the international bathymetric chart  
 214 of the Arctic Ocean (IBCAO, Jakobsson et al., 2012) above  $60^\circ\text{N}$ , blended over a range  
 215 of  $\pm 100$  km about this latitude. Special attention was paid to remove abrupt jumps over  
 216 the merged region. Model depths within important canyons (e.g. Barrow) and across im-  
 217 portant gateways (e.g., Florida Straits, Greenland-Iceland-Faroe-Scotland ridge, Aleu-

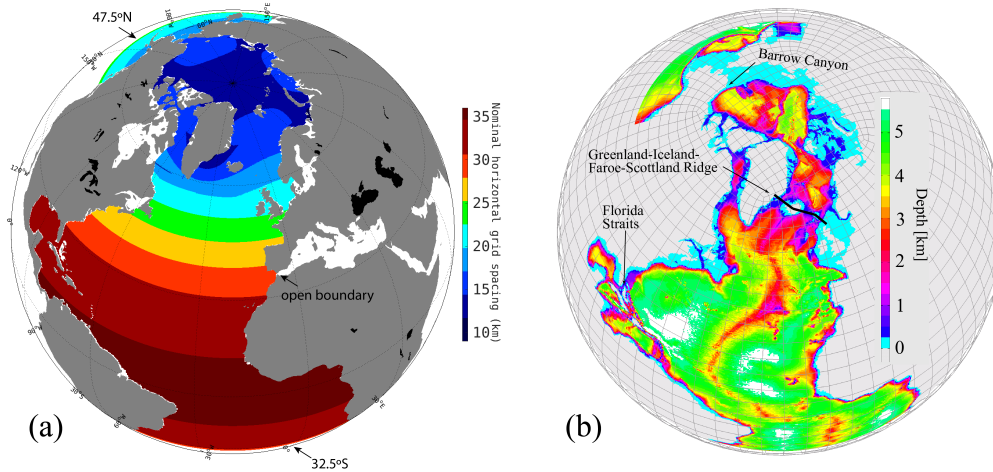


**Figure 3.** (a) Nominal horizontal grid spacing (km) and (b) the bathymetry in ASTE. The lateral open boundaries of the ASTE domain are at  $47.5^{\circ}\text{N}$  in the North Pacific,  $32.5^{\circ}\text{S}$  in the South Atlantic, and at the Gibraltar Strait. White areas in (a), which include the Hudson Bay, Baltic Sea, White Sea, Gulf of St. Lawrence, and all channels in the Canadian Arctic Archipelago except Nares and Barrow Straits, are masked. Depths of several important channels, including the Barrow Canyon, Greenland-Iceland-Faroe-Scotland Ridge and the Florida Straits, were carefully inspected to ensure transports consistent with published observations.

218 tian islands chain, Gibraltar Strait) were enforced to be consistent with observations in  
 219 order to realistically simulate key transports and regional circulations.

220 Atmospheric forcing is applied via bulk formulae (Large & Yeager, 2008) over the  
 221 open ocean, with the initial estimate of the atmospheric state variables from JRA-55 (Kobayashi  
 222 et al., 2015). We considered taking ERA-Interim (Dee et al., 2011) – employed by EC-  
 223 COv4r3 (Forget et al., 2015a; Fukumori et al., 2018a) – as our first guess. However, this  
 224 product has a well documented warm bias of up to  $2^{\circ}\text{C}$  in the Arctic (Beesley et al., 2000;  
 225 Freville et al., 2014; Jakobson et al., 2012; Lupkes et al., 2010) that causes excessive sea  
 226 ice melt. ECCOv4r3 accommodated this warm bias through increased sea ice and snow  
 227 wet albedos. Nguyen et al. (2011) showed reasonable modeled sea ice concentration and  
 228 thickness using the Japanese Reanalysis (JRA-25) without the need to increase sea ice  
 229 albedos above their observed values. For this reason, the updated three-hourly, higher-  
 230 resolution JRA-55 was chosen as the initial surface boundary forcing. Monthly-mean es-  
 231 tuarine fluxes of freshwater are based on the Regional, Electronic, Hydrographic Data  
 232 Network for the Arctic Region (R-ArcticNET) dataset (Lammers & Shiklomanov, 2001;  
 233 Shiklomanov et al., 2006).

234 As shown in Fig. 2 the ECCOv4r3 solution does not exhibit the cyclonic circula-  
 235 tion of Atlantic water in the Arctic that is inferred from hydrographic observations (Rudels,  
 236 2012). For this reason, we elected to initialize from alternative products. Table 1 sum-  
 237 marizes our first-guess model input parameters for sea ice, ocean mixing and momen-  
 238 tum dissipation, along with our choice of ocean-sea ice state to initialize the unconstrained  
 239 simulation. This run serves as iteration 0 of the optimization and will be referred to as  
 240 *it0* for the remainder of the paper. Our selection is informed by existing observation/model-  
 241 based estimates. Importantly, sea ice albedos and drag coefficients are chosen within the  
 242 range of observed and previously optimized estimates Nguyen et al. (2011).

243 The three-dimensional parametric horizontal stirring fields for temperature and salin-  
 244 ity are based on typical values used in the literature (Pradal & Gnanadesikan, 2014; Campin,

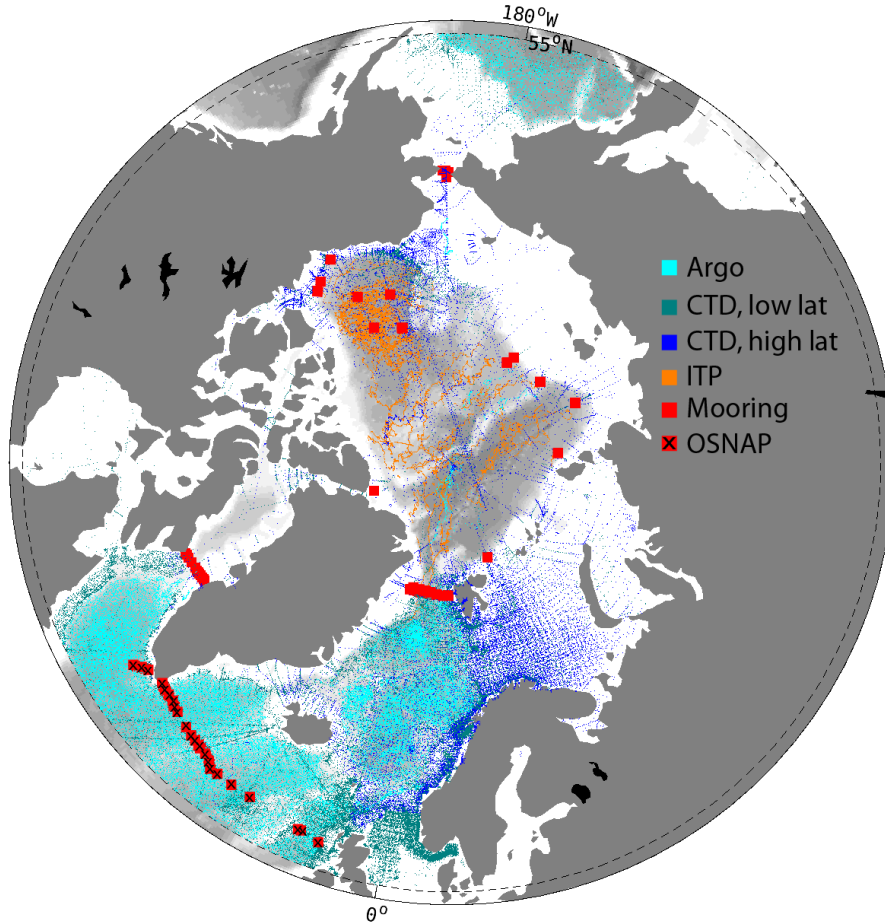


**Figure 4.** In situ observations used to constrain ASTE. Red squares with “x” are additional OSNAP mooring data, used for independent evaluation but not part of the cost function.

245 2014, *pers. comm.*) with consideration for where the ASTE grid resolves the baroclinic  
 246 deformation radius as follows. The vertical background diffusivity  $\mathcal{K}_d$  was set based on  
 247 typical values at latitudes below  $79^\circ\text{N}$  of  $\sim 10^{-5} \text{ m}^2/\text{s}$  and limited observed and mod-  
 248 elled ranges of  $10^{-7}$  to  $10^{-6} \text{ m}^2/\text{s}$  at high latitudes (Padman & Dillon, 1988; Zhang &  
 249 Steele, 2007; Nguyen et al., 2011; Fer, 2014; Sirevaag & Fer, 2012; Cole et al., 2014). Ver-  
 250 tical diffusivities are enhanced by a factor of 10 near the sea floor to mimic lee wave-driven  
 251 mixing (Toole, 2007; Mashayek et al., 2017). Horizontal dissipation is applied as a com-  
 252 bination of biharmonic Leith and Laplacian viscosity (Griffies, 2004; Fox-Kemper & Men-  
 253 emenlis, 2008). At lower latitudes, where eddy effects are better resolved, we follow the  
 254 formulation of Leith (1996) to represent the direct enstrophy cascade at mesoscales. Within  
 255 the attached Gulf Stream, a higher Laplacian viscosity is initially required to reduce the  
 256 Reynolds number and prevent premature separation (Dengg, 1993; Chassignet & Gar-  
 257 raffo, 2001; Chassignet & Marshall, 2013). In the Arctic Mediterranean, where the de-  
 258 formation radius is 4–10 km, an ad-hoc combination of biharmonic Leith and Laplacian  
 259 viscosity is used to ensure consistency of inflow velocity at Fram Strait and an approx-  
 260 imate cyclonic circumpolar AW circulation inside the Arctic (Jochum et al., 2008, see  
 261 Table 1). The model is spun up for 6 years using repeated year 2002 atmospheric forc-  
 262 ing and open boundary conditions (Table 1). The ocean, sea ice and snow states at the  
 263 end of this 6 year spin up became the initial condition for the unconstrained *it0* in the  
 264 optimization procedure described next.

Field	Value	Reference	Note
<b>Unconstrained run (<i>it0</i>)</b>			
<b>Ocean-sea ice state for Jan/2002 obtained after 6-yr spin up from:</b>			
$\theta_0$	WOA09	Locarnini et al. (2010)	Temperature
$S_0$	WOA09	Antonov et al. (2010)	Salinity
$\mathbf{u}_0$	0.0	–	Ocean velocity
$A_{SI_0}$	PIOMAS	Zhang and Rothrock (2003)	Sea ice concentration
$h_{SI_0}$	PIOMAS	Zhang and Rothrock (2003)	Sea ice thickness
$\mathbf{u}_{SI_0}$	0.0	–	Sea ice velocity
<b>Sea ice parameters:</b>			
$\alpha_{SI_{wet,dry}}$	0.7, 0.68	Johnson et al. (2007)	sea ice albedo
$\alpha_{sn_{wet,dry}}$	0.84, 0.77	Johnson et al. (2007)	snow albedo
$C_{da,dw}$	0.00114, 0.0054	Nguyen et al. (2011)	sea ice-[air,ocean] drag
<b>Mixing and dissipation parameters:</b>			
		Nguyen et al. (2011)	Below 50 m in
	–6.5 to –6.0	Zhang and Steele (2007)	eastern Arctic &
		Padman and Dillon (1988)	below 75 m
$\log_{10}(\mathcal{K}_z)$		Sirevaag and Fer (2012); Fer (2014)	in western Arctic
	–5	Munk (1966)	Outside the Arctic & near
	value plus 1	Mashayek et al. (2017)	surface in the Arctic
	50	Pradal and Gnanadesikan (2014)	Grid points next to land
$\mathcal{K}_\sigma$	17		South of 60°N
			North of 60°N
	50	Pradal and Gnanadesikan (2014)	South of 60°N
$\mathcal{K}_{gm}$	50		North of 60°N
	Leith	Leith (1968)	Ocean interior
$\nu$	Ah=0.0005		Coastal south of 40.5°N
	Ah=0.003	Forget et al. (2015a)	Coastal north of 40.5°N
<b>Optimized run (<i>ASTE.R1</i>)</b>			
$\theta_0, S_0, \mathcal{K}_\sigma, \mathcal{K}_{gm}, \log_{10}(\mathcal{K}_z)$ : optimized.			
$\alpha_{SI_{wet,dry}}, \alpha_{sn_{wet,dry}}, C_{da,dw}, \mathbf{u}_0, A_{SI_0}, h_{SI_0}, \mathbf{u}_{SI_0}$ : same as <i>it0</i>			
	Leith	Leith (1968)	South of [70,73]°N in
$\nu$			[Pacific, Atlantic] sector
	Ah=0.0054	Griffies (2004)	North of [70,73]°N in
			[Pacific, Atlantic] sector

**Table 1.** Values of initial ocean and sea ice state, sea ice parameters, and ocean mixing and dissipation for the unconstrained run *it0* and optimized *ASTE.R1* solution.  $\nu$  is either the biharmonic ( $\text{m}^4/\text{s}$ ) or harmonic ( $\text{m}^2/\text{s}$ ) viscosity, and Ah is the harmonic viscosity coefficient (Griffies, 2004). Units for the mixing coefficients  $\mathcal{K}_{[\sigma, gm, z]}$  are  $\text{m}^2/\text{s}$

265

## 2.2 State Estimation Framework

266

267

268

269

270

271

272

ASTE is formally fit to observations through a gradient-based iterative least-square minimization of the model-data misfit function that takes into account data and model parameter uncertainties (Nguyen et al., 2017). The gradient with respect to a high-dimensional space of uncertain input variables, the “controls”, is obtained via the adjoint of the model, derived by means of algorithmic differentiation (AD; Giering et al., 2005; Heimbach et al., 2005). The model-data misfit (or “cost”) function is defined as (Wunsch & Heimbach, 2007):

$$\begin{aligned}
 J = & \sum_{t=t_0+\Delta t}^{t_f} [\mathbf{y}(t) - \mathbf{E}(t)\mathbf{x}(t)]^T \mathbf{R}(t)^{-1} [\mathbf{y}(t) - \mathbf{E}(t)\mathbf{x}(t)] \\
 & + [\mathbf{x}_0 - \mathbf{x}(t_0)]^T \mathbf{B}(t_0)^{-1} [\mathbf{x}_0 - \mathbf{x}(t_0)] \\
 & + \sum_{t=t_0}^{t_f-\Delta t} \mathbf{u}(t)^T \mathbf{Q}(t)^{-1} \mathbf{u}(t)
 \end{aligned} \tag{1}$$

273

274

275

276

277

278

279

280

281

282

283

284

285

286

287

288

289

290

291

292

293

where time  $t \in [t_0, t_f]$ ,  $t_0$  and  $t_f$  are the initial and final time, and  $\Delta t$  the time-stepping of the forward model.  $\mathbf{y}(t)$  is the observation vector and  $\mathbf{x}(t)$  the state vector containing the model ocean (e.g., temperature, salinity, velocities, sea surface height) and sea ice variables (e.g., concentration, ice and snow thickness, velocities) at all grid points (Wunsch & Heimbach, 2007). The combined initial model state  $\mathbf{x}_0$  and input parameter adjustments  $\mathbf{u}(t)$  collectively comprise the control vector  $\boldsymbol{\Omega} \ni \{\mathbf{x}_0, \mathbf{u}(t)\}$ .  $\mathbf{E}$  is the operator mapping the state variables to the observations. The model-data misfit  $\mathbf{y}(t) - \mathbf{E}(t)\mathbf{x}(t)$  is weighted by the inverse error covariance matrix  $\mathbf{R}(t)$ . This accounts for both observational uncertainty and model representation error, where the latter considers the extent to which real variability cannot be represented at the chosen model resolution (Nguyen et al., 2020a).  $\mathbf{B}(t_0)$  and  $\mathbf{Q}(t)$  are error covariances of  $\mathbf{x}_0$  and  $\mathbf{u}(t)$ , respectively. Full knowledge of  $\mathbf{R}$ ,  $\mathbf{B}$ , and  $\mathbf{Q}$  is often unattainable (Wunsch & Heimbach, 2007). As a result, the misfit  $\mathbf{y}(t) - \mathbf{E}(t)\mathbf{x}(t)$  and variables  $\boldsymbol{\delta}\mathbf{x}_0 = \mathbf{x}_0 - \mathbf{x}(t_0)$  and  $\mathbf{u}(t)$  are often assumed Gaussian, with zero means and standard deviations whose squares fill the diagonal entries of their respective covariance matrices (Wunsch & Heimbach, 2007). In the absence of better information, we resort to the simplified representation of the error covariances, consistent with existing state estimation efforts (e.g., Mazloff, Heimbach, & Wunsch, 2010; Forget et al., 2015a; Fukumori et al., 2018a). These error estimates play an important role in any least squares optimization (both ECCO-related and other data assimilation efforts), and their improved estimation is itself an important area of ongoing research (Wunsch, 2018). We will discuss these further below.

294

295

296

297

298

299

300

301

302

303

304

305

There are three distinct contributions to the misfit cost function, eqn. (1). The first term describes the normalized model-data squared misfit to be minimized. This term sums weighted contributions from all observational data considered. The second term penalizes deviation of the initial state  $\mathbf{x}(t_0)$  from the initial guess  $\mathbf{x}_0$  (Table 1). Similarly, the third term describes moderation of input parameter adjustments  $\mathbf{u}(t)$  so that the adjustment amplitude does not far exceed the uncertainties. The adjoint (or Lagrange multiplier) method consists of augmenting the cost function (eqn. (1)) to a Lagrangian function  $\mathcal{L}$  by adding an additional term that enforces the strict adherence of the solution to the model equations. In this manner, the constrained optimization problem (find extrema of  $J$  subject the constraint that the model equations be fulfilled exactly) is converted into an unconstrained problem of finding stationary points of the Lagrangian (Wunsch & Heimbach, 2007).

306

307

308

The optimization problem is solved via gradient-based optimization, in which the gradient of the cost function with respect to the control variables informs an iterative minimization algorithm. In our case, this is the quasi-Newton method following Gilbert

and Lemaréchal (1989). Once the cost function  $J$  is defined, beneficial control adjustments that reduce the misfit are informed by the gradient  $\nabla_{\Omega}J$ . This gradient can be efficiently computed for very high-dimensional control spaces using the adjoint model (Wunsch & Heimbach, 2007). These adjusted controls are then used in a new integration of the forward model for the full period (2002–2017), during which model-data misfits are recomputed. At the end of this forward integration, contributions to the cost-function are accumulated, the adjoint model is integrated, and the gradient information is re-computed informing updated control adjustments for the next integration of the forward model. The optimization thus proceeds in an iterative manner, whereby each iteration entails execution of both the forward and adjoint model, providing updated control adjustments to obtain further reduction of the total model-data misfit in successive iterations. The optimization is continued until little further misfit reduction is achieved between successive iterations. This is expected when the state estimate is in agreement with the observations within the error  $\mathbf{R}(t)$  (expressed, e.g., in terms of a  $\chi^2$  distribution of the squared normalized misfit residuals).

The space of control variables for ASTE,  $\{\mathbf{x}_0, \mathbf{u}\} \in \Omega$ , comprises the 3D hydrographic initial conditions, potential temperature and salinity ( $\theta_0, S_0$ ), the time-varying 2D surface atmospheric state variables, spatially-varying but temporally invariant model coefficients of vertical diffusivity ( $\mathcal{K}_z$ ) and parameterized eddy activity ( $\mathcal{K}_\sigma, \mathcal{K}_{gm}$ ), denoting the strength of eddy-induced isopycnal diffusivity and potential energy transfer, respectively (Forget et al., 2015b). The atmospheric state control variables are 2 m air temperature,  $T_{air}$ , specific humidity,  $q_{air}$ , downward short- and long-wave radiation,  $R_{sw}, R_{lw}$ , precipitation,  $P$ , and 10 m winds  $u_w, v_w$ . Although runoff and evaporation are not control variables, in practice they project onto the precipitation sensitivities, interpreted as the linear combination of net surface freshwater fluxes (evaporation minus precipitation minus runoff,  $E-P-R$ ).

To ensure the adjustments are physically reasonable, *a-priori* uncertainties (i.e. the square-roots of the diagonal terms of  $\mathbf{B}$  and  $\mathbf{Q}$ ) are estimated following Forget and Wunsch (2007); Fenty and Heimbach (2013a); Fukumori et al. (2018b) for oceanic hydrography and Chaudhuri et al. (2013, 2014) for atmospheric forcing. Whilst the estimate from Forget and Wunsch (2007) and Fenty and Heimbach (2013a) quantifies climatological variability, the additional contribution from Fukumori et al. (2018b) accounts for model representation error inferred from a high resolution ( $1/48^\circ$ ) simulation to estimate unresolved variance in ASTE. Uncertainties in the atmospheric state as derived by Chaudhuri et al. (2013, 2014) are based on the spread between atmospheric reanalysis products, which is particularly large over the Arctic.

The vector  $\mathbf{y}(t)$  contains as many available ocean and sea ice observations as we were able to access. The observational backbone of *ASTE\_R1* includes the standard ECCOv4r3 suite (Table A1) of in situ and remotely-sensed ocean data: temperature and salinity profiles from Argo, GO-SHIP and other research cruises, instrumented pinnipeds, gliders, and moorings, and ice-tethered profilers; ocean bottom pressure anomalies from GRACE (Watkins et al., 2015; Wiese et al., 2018); sea surface height from Ocean Surface Topography Mission/Jason 2 and Jason 3 (Zlotnicki et al., 2019); Mean Dynamic Topography DTU13 (Andersen et al., 2015); and infrared and microwave-derived sea surface temperature (JPL\_MUR\_MEaSURES\_Project, 2015). For details on how the data and their uncertainties were obtained and prepared we refer the readers to Fukumori et al. (2018b). In addition to the ECCOv4r3 suite, the data are augmented by updated high latitude in situ profiles, ship-based CTD, and mooring observations at important Arctic gateways and in the Arctic interior (see Table 2, Fig. 4).

The estimation period chosen for ASTE, 2002–2017, leverages the increase in satellite (GRACE, ICESat-1/2, CryoSat-2) and in situ (ITP) observations in the Arctic, as well as the beginning of the quasi-global Argo float deployment. In total, approximately  $1.2 \times 10^9$  observations were employed to constrain distinct aspects of the modeled ocean

Data Type	Spatial coverage	Temporal coverage	Description	Source
<b>Sea ice</b>				
Velocity <sup>1</sup>	N.Hemis	2002–2012	passive microwave & AVHRR & IABP	<a href="http://rkwok.jpl.nasa.gov/radarsat/3dayGr_table.html">rkwok.jpl.nasa.gov/radarsat/3dayGr_table.html</a> <a href="http://nsidc.org/data/docs/daac/nsidc0116_icemotion.gd.html">nsidc.org/data/docs/daac/nsidc0116_icemotion.gd.html</a> Kwok and Cunningham (2008), Fowler et al. (2013)
	N.Hemis	2012–2015	ASCAT & SSMI	<a href="http://ftp.ifremer.fr/ifremer/cersat/products/gridded/psi-drift">ftp.ifremer.fr/ifremer/cersat/products/gridded/psi-drift</a>
Thickness <sup>1</sup>	N.Hemis	2011–2017	CryoSat-2	<a href="http://www.meereisportal.de/datenportal.html">www.meereisportal.de/datenportal.html</a> & Ricker et al. (2017)
	N.Hemis	2010–2017	SMOS	<a href="http://icdc.zmaw.de/l3c-smos_sit.html">icdc.zmaw.de/l3c-smos_sit.html</a> & Tian-Kunze et al. (2014)
	N.Hemis	2003–2008	ICESat	<a href="http://rkwok.jpl.nasa.gov/icesat/index.html">rkwok.jpl.nasa.gov/icesat/index.html</a> & Kwok and Cunningham (2008); Kwok et al. (2009)
Concentration	N.Hemis	2002–2017	SSMI & OSISaf	<a href="http://osisaf.met.no/p/ice/index.html">osisaf.met.no/p/ice/index.html</a> & Lavergne et al. (2019)
<b>Ocean</b>				
ITP (T,S)	Arctic	2004–2017	Profilers	<a href="http://www.whoi.edu/itp/data/">www.whoi.edu/itp/data/</a> Krishfield et al. (2008), Toole et al. (2011); Krishfield (2020),
Hydrographic Survey (T,S)	GINs	2002–2006	ASOF	<a href="http://www.pangaea.de/">www.pangaea.de/</a>
	Beaufort Sea	2003–2017	BGOS	<a href="http://www.whoi.edu/beaufortgyre/home/">www.whoi.edu/beaufortgyre/home/</a> <a href="https://doi.org/10.1594/PANGAEA.761766">doi.pangaea.de/10.1594/PANGAEA.761766</a> & Bauch et al. (2009)
	Laptev Sea	2002–2003		<a href="https://doi.org/10.1594/PANGAEA.763451">doi.pangaea.de/10.1594/PANGAEA.763451</a> & Bauch et al. (2011)
	East Arctic	2007		<a href="https://doi.org/10.1594/PANGAEA.763451">doi.pangaea.de/10.1594/PANGAEA.763451</a> & Bauch et al. (2011)
Mooring (T,S,currents)	GINs	2002–2013		Våge et al. (2015)
	Fram Strait	2002–2017	ASOF	Fahrbach et al. (2001), Beszczynska-Möller et al. (2012)
	East Arctic	2002–2015	NABOS	<a href="http://nabos.iarc.uaf.edu/">nabos.iarc.uaf.edu/</a> , Pnyushkov et al. (2013) and
	West Arctic	2002–2015	CABOS	Polyakov et al. (2012)
	Beaufort Gyre	2004–2017	BGOS	<a href="http://www.whoi.edu/website/beaufortgyre/data">www.whoi.edu/website/beaufortgyre/data</a>
	Bering Strait	2002–2017		<a href="http://psc.apl.washington.edu/HLD/Bstrait/Data/">psc.apl.washington.edu/HLD/Bstrait/Data/</a> & Woodgate (2018)
Transports <sup>1</sup> of Vol & Heat & Freshwater	Davis Strait	2004–2015		<a href="http://iop.apl.washington.edu/data.html">iop.apl.washington.edu/data.html</a> , Curry et al. (2011)
	Fram Strait	2002–2017	ASOF	Schauer and Fahrbach (2004) & Beszczynska-Möller et al. (2012)
T,S	Bering Strait	2002–2017	mooring	Woodgate (2018)
	High Latitude	2002–2015	IARC	<a href="http://oregon.iarc.uaf.edu/dbaccess.html">oregon.iarc.uaf.edu/dbaccess.html</a>
			IARC	<a href="http://climate.iarc.uaf.edu/geonetwork/srv/en/main.home">climate.iarc.uaf.edu/geonetwork/srv/en/main.home</a>
			ICES	<a href="http://ocean.ices.dk/HydChem/HydChem.aspx?plot=yes">ocean.ices.dk/HydChem/HydChem.aspx?plot=yes</a>
	CAA	2002–2015	SBI	<a href="http://www.eol.ucar.edu/projects/sbi/">www.eol.ucar.edu/projects/sbi/</a>
Arctic	2002–2015	BIO	<a href="http://www.bio.gc.ca/science/data-donnees/base/run-courir-en.php">www.bio.gc.ca/science/data-donnees/base/run-courir-en.php</a>	
Arctic	2002–2015	ACADIS	<a href="http://www.aoncadis.org/home.htm">www.aoncadis.org/home.htm</a>	
	Arctic	2002–2015	WHOI	(Krishfield, 2020)

**Table 2.** Satellite and *in situ* data used to constrain or assess ASTE in addition to the ECCOV4r3 dataset. <sup>1</sup>Datasets that are used only for assessment and not part of the cost function.

362 and sea-ice state, culminating in the optimized *ASTER1* solution. Key among these are  
 363 satellite-based observations of sea level anomalies (SLA) to aid removal of the precip-  
 364 itation bias in JRA-55, Argo and lower latitude CTD to improve surface and sub-surface  
 365 hydrography in the North Atlantic and Nordic Seas, and a suite of moorings in the Arc-  
 366 tic. This suite includes the Fram Strait mooring array to constrain the boundary cur-  
 367 rent strength and heat flux from the Nordic-Seas into the Arctic, and the combined ITP  
 368 and Beaufort Gyre moorings to constrain the Canada Basin hydrography. Finally, OS-  
 369 ISaf daily sea ice concentration was essential for constraining the ice edge and upper ocean  
 370 hydrography in the Arctic and its surrounding marginal seas.

371 The error  $\mathbf{R}$  associated with the observations  $\mathbf{y}(t)$  is the combined data uncertainty  
 372 and model representation error. For hydrographic data, the derivation is as described  
 373 above for the *a-priori* uncertainties  $\mathbf{B}$ . For satellite data, errors are a combination of the  
 374 corresponding satellite mission’s provided uncertainty and model representation errors,  
 375 as described in (Fukumori et al., 2018b). These representation errors were derived from  
 376 the data variance within (and weighted by the area of) ASTE horizontal grid box. They  
 377 generally exceed the stated mission uncertainty. As seen in eqn. (1),  $\mathbf{R}$  plays an impor-  
 378 tant role in weighting the individual model-data misfit terms. Careful assessment of  $\mathbf{R}$   
 379 is thus required to ensure an appropriate and balanced contribution of the diverse datasets  
 380 to the total  $J$ .

381 The practical implementation of eqn. (1) follows that described in Forget et al. (2015a).  
 382 Several approximations to parameterization in the adjoint model were made to ensure  
 383 stable behaviour. Maximum isopycnal slopes are limited in the GM/Redi parameteri-  
 384 zation, the vertical mixing scheme (K-Profile Parameterization, Large et al., 1994) is omit-  
 385 ted in the adjoint, and increased horizontal and vertical momentum dissipation are em-  
 386 ployed in the adjoint to suppress fast growth of unstable sensitivity.

387 The full sea ice adjoint, as described in Fenty and Heimbach (2013a); Fenty et al.  
 388 (2015), was not used in this study (nor in ECCOv4), due to persistent instability issues.  
 389 In its place, the sea ice concentration model-data misfit is used to relate air-sea fluxes  
 390 to the enthalpy of the integrated surface ocean-sea ice system as follows. Where the model  
 391 has an *excess/deficiency* of sea ice, extra heat is added to, or removed from the system  
 392 to bring the sea surface to above or below the freezing temperature. In these two cases,  
 393 the pseudo-sea ice cost function contributions  $J_{\text{seaice\_conc.}[ex,de]}$  are in enthalpy units rather  
 394 than normalized model-data misfits. Normalization is chosen to obtain amplitudes com-  
 395 parable to other model-data misfits  $J_i$  contributing to the total cost function  $J$ , so that  
 396 these terms play an active role in the optimization. Lastly, convergence – if achievable  
 397 for these two pseudo-sea ice costs – is when they approach zero and not unity.

398 After 62 iterations, a substantial reduction in model-data misfit has been achieved  
 399 compared to the unconstrained simulation, such that the solution is deemed suitable as  
 400 ASTE first release. The initial conditions of the optimized state, ASTE Release 1 (*ASTER1*),  
 401 are derived by adding the adjustments  $[\Delta\theta, \Delta S]_{i62}$  to the first guess fields  $[\theta, S]_{i0}$ . The  
 402 same holds for the optimized mixing fields and surface atmospheric state (see Table 1).  
 403 Adjustments to the uncertain control variables obtained as a result of the gradient-based  
 404 optimization enable the improvement in the model fit to observations while retaining dy-  
 405 namical consistency. Fig. 5 shows the uncertainty and adjustments for four of the seven  
 406 surface atmospheric state variables,  $T_{air}$ ,  $R_{sw}$ ,  $R_{lw}$ , and  $v_w$ . The uncertainty, derived from  
 407 Chaudhuri et al. (2013, 2014), shows some of the largest disagreements amongst the at-  
 408 mospheric reanalyses to be in the Arctic (Fig. 5a1–a4). The percentile (pctl) thresholds  
 409 indicate that for these four fields the adjustments are within the uncertainty. Overall,  
 410 the 99-pctl adjustments are within  $2\sigma$  for all time-dependent atmospheric variables ex-  
 411 cept downward shortwave where it is within  $3\sigma$ .

412 The full monthly mean state of *ASTER1* is distributed via the ECCO & ASTE  
 413 data portal at the Texas Advanced Computing Center (TACC). In addition, the model

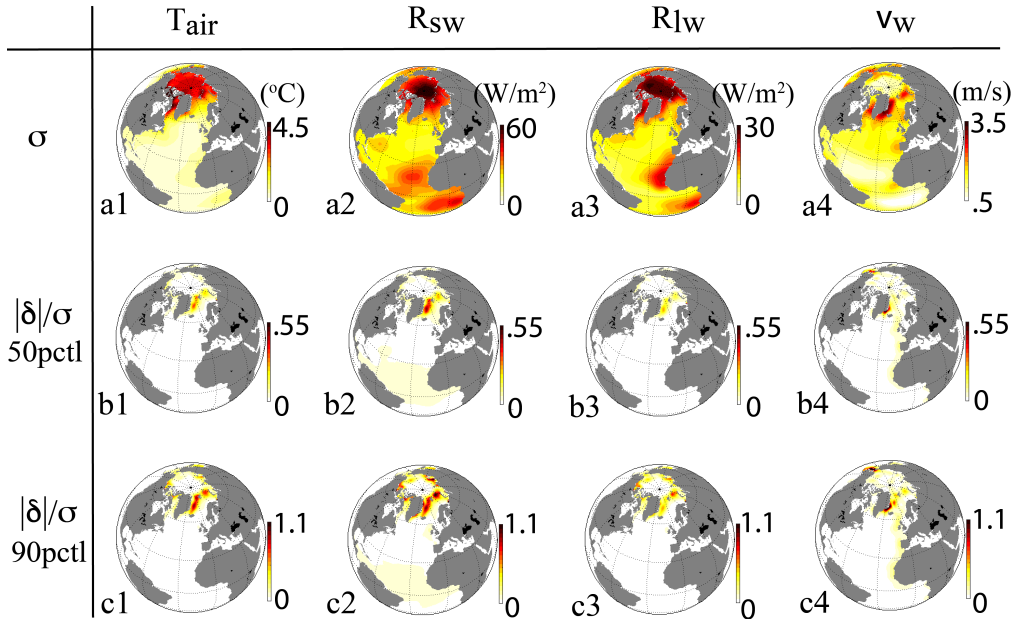


**Figure 5.** The atmospheric forcing field (a1–a4) uncertainty  $\sigma$  and (b1–b4) the 50-percentile and (c1–c4) 90-percentile normalized adjustment magnitudes  $|\delta|/\sigma$ . The uncertainty fields have units given above the color scale for a1–a4. Note that the reciprocal of the squared value of these uncertainties are entries in the weight matrix  $\mathbf{Q}$ . The normalized adjustment magnitudes are dimensionless.

414 configuration, required input fields and code are distributed to enable reruns (see Ap-  
 415 pendix A). Since the focus of *ASTE* is on the North Atlantic and the Arctic Ocean, we  
 416 restrict both the discussion presented below and the distributed *ASTE\_R1* fields to lat-  
 417 itudes above  $10^\circ\text{N}$ . As for ECCOv4r3, the mass, salt, and heat budgets in *ASTE\_R1*  
 418 are accurately closed when computed using the distributed standard ECCO diagnostics that  
 419 we provide. In Appendix B, we show how lateral transports may be accurately computed  
 420 and provide estimates for the errors incurred in offline calculations using the *ASTE\_R1*  
 421 monthly mean diagnostics.

### 422 2.3 Making Meaningful Model-Observation Comparisons

423 A meaningful assessment of *ASTE\_R1* through comparison with observations is non-  
 424 trivial and requires careful consideration. One of the biggest challenges is properly ac-  
 425 counting for the sparse spatio-temporal sampling and the potential for aliasing. For ex-  
 426 ample, measurements might only be taken at a discrete location (e.g. a mooring) or along-  
 427 track (i.e., with high along-track coverage and drastically lower resolution in the cross-  
 428 track direction) or only during summer months (e.g., ship-based CTD). “Averages” of  
 429 these measurements (e.g., average Argo or ITP data over 1 month or 1 year) incur alias-  
 430 ing in both space and time as well as potential spatial or seasonal biases. “Averages”  
 431 of *ASTE\_R1* outputs at the smallest spatial scale (grid cell size), on the other hand, are  
 432 over a spatial area of  $\sim 200 \text{ km}^2$ . Unless observations are well sampled over this grid-  
 433 area, a direct comparison between observations and *ASTE\_R1* can be problematic. Fur-  
 434 thermore, *ASTE\_R1* does not resolve eddies in the Arctic and GIN Seas. As a result,  
 435 we should neither expect nor demand a perfect fit to discrete (in space/time) measure-  
 436 ments. As is common in data assimilation (Janjić et al., 2017) the ECCO framework uti-

437 lizes “representation errors” - described above - in the weighting of the model-data mis-  
 438 fits, eqn. (1), to safeguard against over-fitting and facilitate more meaningful model-data  
 439 comparison (Wunsch & Heimbach, 2007). However, these representation errors are them-  
 440 selves highly uncertain, often relying on unconstrained high-resolution model runs from  
 441 which they are inferred (see Nguyen et al., 2020a, for a more detailed discussion).

442 In Section 3 we present both normalized misfit reductions as well as comparisons  
 443 of dimensional transports and heat/freshwater contents. For the dimensional quantities,  
 444 we encounter several potential challenges related to resolution and bias issues, which we  
 445 briefly discuss in the following. A serious challenge stems from the need to compare wa-  
 446 termasses in the presence of hydrographic biases. From observations, watermasses are  
 447 often defined in temperature, salinity, and density (T, S,  $\sigma$ ) space with tight thresholds/bounds  
 448 reflecting the measurement precision (e.g. to the first or second decimal place). These  
 449 definitions can be problematic to adopt in *ASTE\_R1*, where we are averaging over grid-  
 450 cell areas of  $\sim 200 \text{ km}^2$  and thicknesses of 10–500 m. Furthermore, in some regions the  
 451 model representation errors may be up to an order of magnitude larger than measure-  
 452 ment precision. In these regions, the normalized misfit can be within acceptable range,  
 453 but *ASTE\_R1* can still possess notable absolute (T, S,  $\sigma$ ) biases if the representation er-  
 454 rors are large. For this reason, a watermass is likely to exist in *ASTE\_R1* but with mod-  
 455 ified thresholds/bounds. Where appropriate, we analyzed *ASTE\_R1* carefully in (T, S,  
 456  $\sigma$ ) space to identify suitable classifications for calculation of watermass transports. De-  
 457 tails on the modified bounds are provided in Appendix C.

458 A second challenge is related to the region over which derived quantities are com-  
 459 puted. In cases where these regions are defined with geographic bounds based on avail-  
 460 ability of observations rather than dynamical regimes, the equivalent derived quantities  
 461 in *ASTE\_R1* can be highly sensitive to small shifts in bounding region, especially when  
 462 the grid resolution and uncertainties in the control input parameters (e.g., forcing, in-  
 463 ternal mixing) are taken into account. For this reason, we also explore the sensitivity of  
 464 area/volume integrals to choice of geographical bounds in Appendix C.

465 Lastly, comparison of (dimensional) integrated transports can be problematic due  
 466 to spatial sampling issues and representation error, preventing precise estimation of nar-  
 467 row boundary currents in *ASTE\_R1*. An example is at Fram Strait, where the *ASTE\_R1*  
 468 grid cannot resolve the e-folding scale of the West Spitsbergen Current (Beszczynska-  
 469 Möller et al., 2012). Enforcing fit to the observed mooring velocity would likely result  
 470 in an overestimation of the net inflow volume transport here. In *ASTE\_R1*, velocities  
 471 at gateways were not employed as active constraints but were used for offline assessment  
 472 of the derived transports. Ultimately, however, the spacing between discrete moorings  
 473 offers incomplete information on the total volume transports across a given gateway, and  
 474 existing observation-based estimates generally require various assumptions on spatial/temporal  
 475 correlations in order to interpolate between the mooring measurements. As a result, our  
 476 direct comparisons of *ASTE\_R1* and observation-based transports presented below seeks  
 477 consistency in terms of sign and order of magnitude rather than exact agreement of am-  
 478 plitude. This is especially true for assessment of *ASTE\_R1* heat and freshwater trans-  
 479 ports, computed relative to the wide range of reference values used in the literature.

### 480 3 Model-data misfit reduction and residuals

481 In what follows, we will assess the *ASTE\_R1* solution in the context of existing observation-  
 482 based estimates of the circulation and hydrography in the Arctic. We first compare *it0* and  
 483 *ASTE\_R1* using the online and offline cost metrics described in Section 2 and listed in  
 484 Table 3, and summarize the reduction in the integrated model-data misfits and costs achieved  
 485 in the production of *ASTE\_R1*. We then expand this discussion, considering the *ASTE\_R1*  
 486 fit to constraints in the Arctic, GIN Seas, and Subpolar North Atlantic (sections 3.1-3.3).  
 487 Note that assimilation aids – but by no means guarantees – model-data consistency due

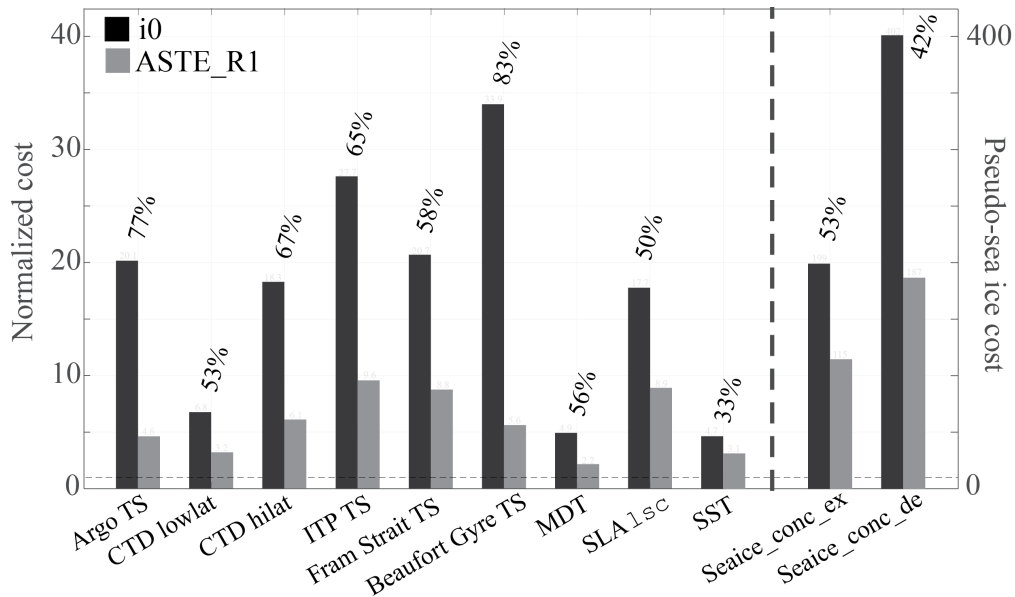


**Figure 6.** Aggregated cost reductions calculated from key data sets that were used in the optimization. The numbers listed above each data set are the percentage of cost reduction in *ASTE\_R1* compared to *it0*. The magnitudes of the two pseudo-sea ice costs are indicated on the right abscissa.

488 to errors and/or deficiencies in the data, model, and/or state estimation framework. This  
 489 point will be revisited in our discussion in section 5. We refer to “misfit” as the dimen-  
 490 sional model minus data difference, “normalized misfit” as misfit scaled by the respec-  
 491 tive uncertainty (dimensionless), and “normalized cost” or “cost” as the square of the  
 492 normalized misfit (dimensionless). The overall cost reductions in *ASTE\_R1* have been  
 493 grouped into several categories as shown in Fig. 6 and summarized in Table 3.

### 494 3.1 Arctic

#### 495 3.1.1 Sea ice

496 Improved representation of sea ice extent in *ASTE\_R1* (compared to the uncon-  
 497 strained simulation) is indicated by a significant reduction of  $J_{\text{seaiice\_conc[ex,de]}}$  by 53%  
 498 and 42%, respectively (Table 3, Fig. 6). Fenty and Heimbach (2013b) showed that these  
 499 improvements can be effectively achieved through small adjustments of atmospheric con-  
 500 trols, within their uncertainty range. These improvements are independently confirmed  
 501 by the reduction in offline misfits for sea ice area ( $J_{\text{seaiice\_area15}}$ , 64%) and extent ( $J_{\text{seaiice\_extent15}}$ ,  
 502 83%) (Table 3). The largest improvements occur in the seasonal ice zones e.g., Green-  
 503 land and Barents Seas and Southern Beaufort Gyre (Fig. 7a) associated with a systemat-  
 504 ic decrease in total simulated area/extent without alteration of the seasonal cycle (Fig. 7b).

505 The improved sea ice edge representation in *ASTE\_R1* (Fig. 7e,h) is accompanied  
 506 by a reduction in the offline misfits for sea ice velocities ( $J_{\text{seaiice\_vel}}$ , Table 3), primar-  
 507 ily in locations where nonzero ice velocities in *it0* were accompanied by observations of  
 508 zero ice concentration and vice versa. Unlike velocity, however, the sea ice thickness costs  
 509  $J_{\text{seaiice\_thickness}}$  did not decrease (Table 3), primarily because the pseudo-sea ice adjoint  
 510 does not contain physics relating ice thickness to the atmospheric forcing or ocean in-  
 511 teraction from below. We will return to this in section 6.

Cost name	Normalized cost		Percentage reduction (%)
	<i>it0</i>	<i>ASTE_R1</i>	
$J_{\text{Argo\_TS}}$	20.1	4.6	77
$J_{\text{CTD\_lowlat}}$	6.8	3.2	53
$J_{\text{CTD\_hilat}}$	18.3	6.1	67
$J_{\text{ITP}_{\text{TS}}}$	27.7	9.6	65
$J_{\text{FramStrait}_{\text{TS}}}$	20.7	8.8	58
$J_{\text{BeaufortGyre}_{\text{TS}}}$	33.9	5.6	83
$J_{\text{BeringStrait}_{\text{TS}}}$	6.3	4.2	33
$J_{\text{DavisStrait}_{\text{TS}}}$	3.8	4.3	-11
$J_{\text{NABOS}_{\text{TS}}}$	43.1	25.3	41
$J_{\text{StAnnaTrough}_{\text{TS}}}$	22.9	7.2	69
$J_{\text{seaice\_conc\_ex}}$	402	187	53
$J_{\text{seaice\_conc\_de}}$	199	115	42
$J_{\text{SST}_{\text{[Reynolds+TMI/AMSRE]}}}$	4.7	3.1	33
$J_{\text{MDT}}$	4.9	2.2	56
$J_{\text{SLA}_{\text{[gfo+ers+tp]}}}$	2.7	1.4	49
$J_{\text{SLA}_{\text{lsc}}}$	17.7	8.9	50
<hr/> <hr/>			
$J_{\text{seaice\_area15}}^{(o)}$	1.0	0.36	64
$J_{\text{seaice\_extent15}}^{(o)}$	1.0	0.17	83
$J_{\text{seaice\_thickness}}^{(o)}$	22.0	25.8	-17
$J_{\text{seaice\_UV}}^{(o)}$	2.1	1.6	23
$J_{\text{FramStrait\_vNorth}}^{(o)}$	1.3	1.0	26
$J_{\text{NABOS\_mmpUV}}^{(o)}$	2.0	1.6	23
$J_{\text{OSNAP}_{\text{TS}}}$	6.3	3.5	44
$J_{\text{lineW}_{\text{TS}}}$	3.3	2.5	26

**Table 3.** Active and offline costs and reductions in *ASTE\_R1* compared to *it0*. The quantities listed above the triple horizontal lines contribute directly to the total  $J$  in eqn. (1), i.e., contribute to the gradient-based minimization, whereas those listed below the triple horizontal lines ( $J^{(o)}$ ) are purely diagnostic, i.e. are used only for offline assessment and do not influence the optimization. The offline sea ice area and extent (both defined using the common 15% cutoff threshold) costs are normalized by the Arctic Mediterranean’s area.

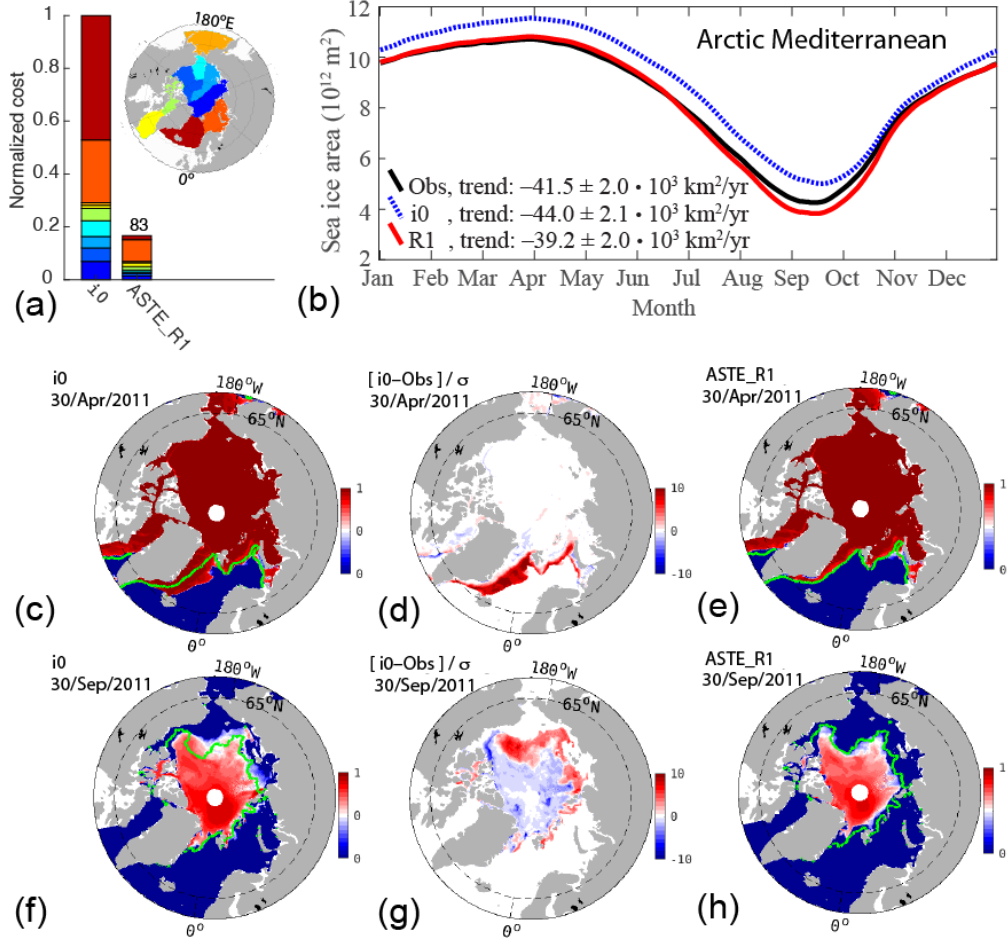


**Figure 7.** Comparison of sea ice misfits in the Arctic Mediterranean, for the unconstrained *it0* and the optimized *ASTE\_R1* solution, assuming the standard 15% cutoff threshold for both total ice area and extent. (a) Comparison of cost (misfit squared) to observed sea ice extent,  $J_{\text{seaice\_extent15}}^{(o)}$ , showing contributions from individual basins. (b) Comparison of 12-month climatology of sea ice area, also showing observation-based climatology from OSSISaf (black). The climatology and the trends listed in the legend were derived from the 01/Jan/2002–31/Dec/2017 time-series. Comparison of daily sea ice concentration between *it0* (c,f), and *ASTE\_R1* (e,h), for days selected at times of maximum (c,e) and minimum (f,h) ice extent. The green contour in panels (c,e,f,h) delineates the observed sea ice concentration from OSSISaf at the indicated dates. The optimization acts to reduce concentration at the ice margin where notable biases exist in *it0*. These biases are shown normalized by uncertainty in the OSSISaf observations for (d) 30/Apr/2011 and (g) 30/Sep/2011.

512

### 3.1.2 Fram Strait

513

514

515

516

517

518

519

520

The dynamics in the vicinity of Fram Strait are highly complex, governed by strong air-ice-ocean interaction, vigorous generation of eddies associated with highly sheared boundary currents and their recirculations in the presence of significant topographic steering (Beszczynska-Möller et al., 2012; de Steur et al., 2014; von Appen et al., 2015a, 2015b; Hattermann et al., 2016). Given the complexity and challenge to realistically simulate watermass properties and transports across this gate (e.g., Nguyen et al., 2011; Ilicak et al., 2016; Docquier et al., 2019) the Fram Strait moorings provide an invaluable constraint.

521

522

523

524

525

526

527

528

529

530

531

532

In view of the importance of AW for the wider Arctic region, we paid particular attention to skillfully represent AW inflow at Fram Strait as follows. Early in the development of *ASTER1* and prior to the gradient-based optimization, we compared the simulated volume transport to daily-average moored velocity (available for the years 2002–2011) at various depths along the entire array (Beszczynska-Möller et al., 2011, 2012). The model viscosity was prescribed (section 2.1, Table 1) to ensure we obtained a representative volume transport across the strait. During the iterative optimization, the mooring temperature and salinity were included in the active costfunction ( $J$ ) to directly constrain  $T/S$  at the strait. Via these steps, indirect constraint of the tracer transports (i.e.,  $v * T$  and  $v * S$ ) and their constituents (e.g., “inflow/outflow of AW”) at Fram Strait was achieved, as shown by comparison to additional data for the years 2012–2017 (von Appen et al., 2015b) that were withheld from the optimization for offline evaluation.

533

534

535

536

537

538

539

540

541

542

543

544

545

546

547

Fig. 8 shows the unconstrained *it0* and *ASTER1* misfits to moored  $T, S$ , and northward velocity, as a function of longitude. For the region occupied by AW inflow, the normalized misfit in temperature is reduced by 71% compared to the unconstrained *it0* simulation (Fig. 8a). On the continental shelf, west of  $4^\circ\text{W}$ , *ASTER1* has a warm bias compared to the observations, which resulted in higher misfits here (red bar between longitude  $8.1^\circ\text{W}$  and  $4.1^\circ\text{W}$  in Fig. 8a). The reduction in misfits for inflow of the AW, however, is more important for the large-scale Arctic hydrography, as AW passing through this important gateway propagates along the entire boundary of the Eastern Arctic and into the Canada Basin. Here its properties can be compared to ITP data, which serve as the main constraint on subsurface  $T/S$  over the entire pathway from the Fram Strait (see section 3.2.3). The misfit reduction can be seen for one example mooring at approximately  $8^\circ\text{E}$  (Fig. 8d–f) at multiple depths. The significant improvement in salinity at the surface (dashed blue in Fig. 8e) is related to the improved ice edge (see also Fig. 7c–e). Another significant improvement is in the AW core temperature at depth  $\sim 250$  m (solid blue and red lines in Fig. 8d).

548

### 3.1.3 Canada Basin hydrography

549

550

551

552

553

554

555

556

Once the AW, via the West Spitsbergen Current, crosses Fram Strait and traverses the Eastern Arctic along the continental slope (Rudels, 2015; Pnyushkov et al., 2018; Polyakov et al., 2017), the watermass properties (e.g., current strength and direction, density, temperature) are not as well constrained due to extreme data paucity in the Eastern Arctic. In particular, along the boundary current path (shoreward of the red contour in Fig. 9a), only 1% of the total 2004–2016 ITP data are acquired within the Nansen Basin; only 4.5% are acquired in the combined Amundsen and Makarov Basins (Fig. 9b–d). The majority of the ITP data (71%) are within the Canada Basin (Fig. 9e).

557

558

559

560

561

562

Fig. 10 shows the misfit reduction between the unconstrained *it0* and *ASTER1* as a function of basins and depths. The reduction is throughout the upper 800 m of the water column. Seawater density in the Arctic is primarily controlled by salinity, whereas temperature behaves more like a passive tracer and can be more flexibly impacted by the optimization procedure. As a result, the reduction in *ASTER1* temperature misfits greatly exceeds the reduction in salinity misfits in the Arctic, with the most notable

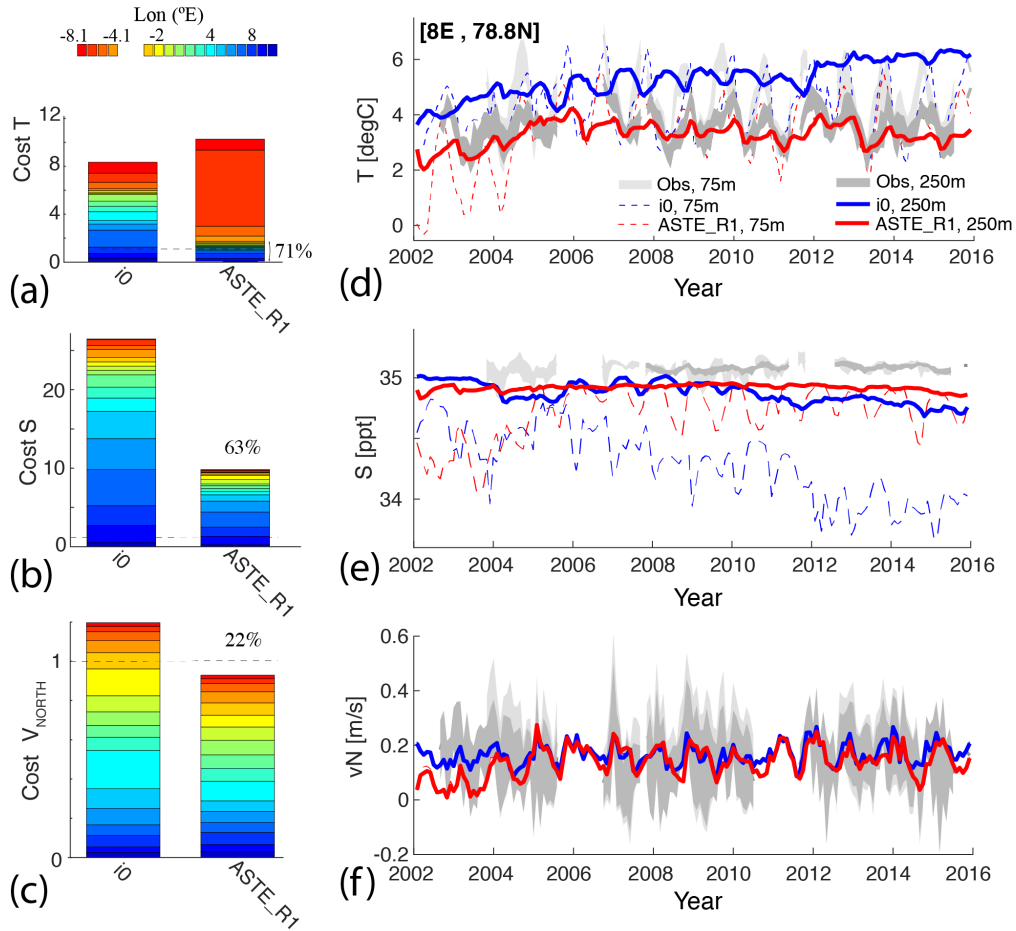


**Figure 8.** Normalized cost at Fram Strait for (a) temperature, (b) salinity, and (c) northward velocity between moored observations and unconstrained *it0* and *ASTE\_R1* solutions, plotted as a function of longitude. Time series of (d) temperature, (e) salinity, and (f) northward velocity at one example mooring at [8°E,78.8°N] for depths 75 m and 250 m show that these properties are improved over the entire observed record. Grey envelopes in (d,e,f) show observed monthly-mean  $\pm$  monthly-std values, with monthly values derived from the daily-mean values for each observed variable. Dashed lines in (a–c) delineate the normalized cost value of 1, targeted during the iterative optimization. Percentages listed in (a–c) are the cost reduction in (a) temperature, (b) salinity and (c) northward velocity. For (b–c) salinity and velocity, these cost reductions are summed across all longitudes, reflecting improvements across the entire mooring array. For (a) temperature, we see a degradation of the solution at the western end of the array during production of *ASTE\_R1*, with a net cost increase of 23%. In this case, the 71% reduction in normalized cost cited is computed using only the eastern moorings, reflecting important improvements in the incoming Atlantic Water carried by the West Spitsbergen Current.

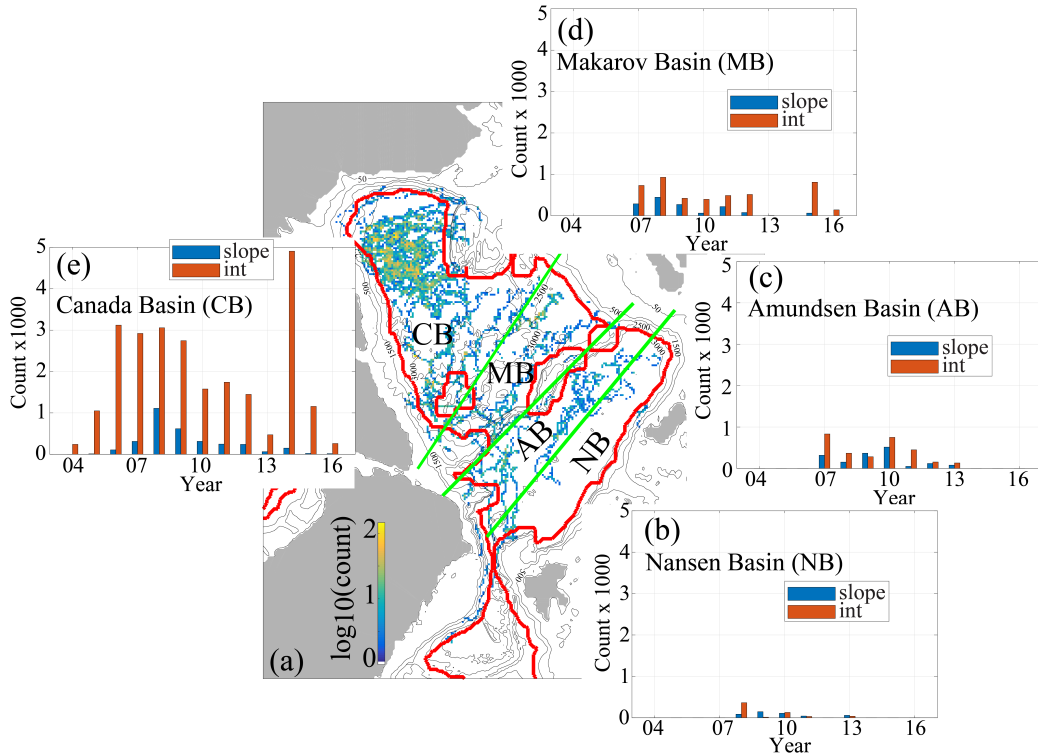


**Figure 9.** Distribution of ITP data as a function of year and geography. In (a), the red contour serves as a proxy for the separation between the continental shelf/slope (slope) and basin interior (int). It is defined as  $\sim 100$  km offshore of the 300 m isobath. The thick green lines approximately separate the Nansen Basin (NB), Amundsen Basin (AB), Makarov Basin (MB) and Canada Basin (CB). In (b)–(e), histograms of the number of ITP profiles for the continental shelf/slope (blue) and Arctic interior (orange) are normalized by the maximum number available for the Canada Basin (5000). The years of ITP data coverage are 2004–2016. There are a total of 39,904 ITP profiles.

563 improvement occurring within the AW core (120–450 m, Fig. 10a-c). The remaining notable temperature misfits in *ASTER1* are at depths occupied by the mixed layer (10–65 m) and below the AW core (450–800 m, Fig. 10c). Large salinity misfits also persist in the mixed layer and in the halocline (120–250 m, Fig. 10d–f). The optimization has, nevertheless, significantly narrowed the misfit distribution, eliminating the largest amplitude biases throughout the water column in temperature and especially below 400 m depth in salinity. The overall reduction is 85% for temperature and 56% for salinity.

570 An example of how temperature misfits are reduced in the water column is shown in Fig. 11 for ITP #55, whose trajectory began in the Canada Basin interior (red circle in Fig. 11a) and ended at the slopes of the Chukchi Plateau (green square). In the observations several watermasses can be seen, including the surface cold layer above  $\sim 30$  m, warm Pacific Summer Water (PSW) at  $\sim 40$ –100 m, Cold Halocline Waters at  $\sim 110$ –250 m, and the Atlantic Water core at depths  $\sim 300$ –750 m (Fig. 11b). In the unconstrained *it0*, both the AW boundary current and the halocline are too warm, the AW layer is too thick, and the PSW is too cold. In *ASTER1*, closer consistency is obtained with temperature observations for all watermasses. We emphasize that we have not applied direct adjustments to the time-varying simulated ocean state to achieve this fit (i.e., no “analysis increments” were applied). Instead, it is achieved through adjustments of the con-

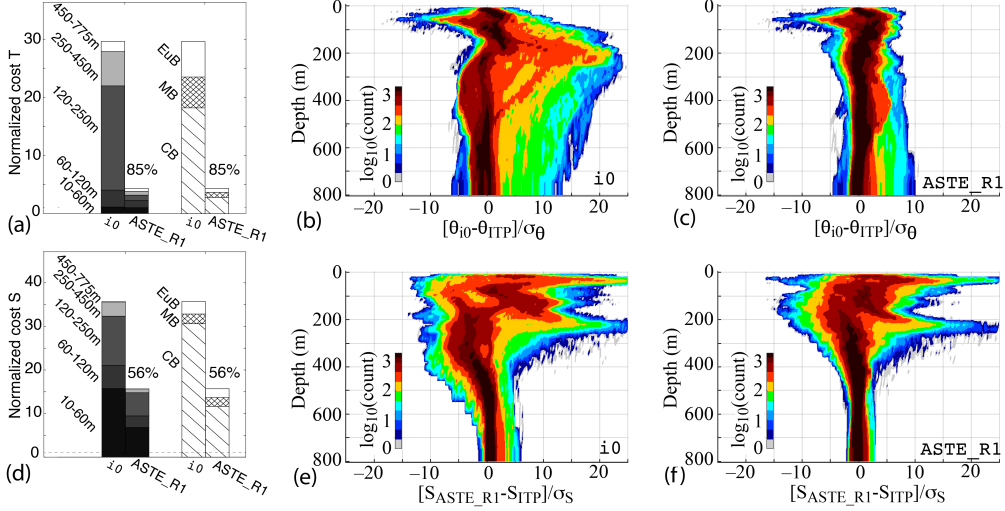


**Figure 10.** Normalized cost for ITP (a–c) temperature and (d–f) salinity. Costs to all ITP data are grouped by depth range and basin in (a) and (d). For the Canada Basin, histograms as a function of depths (b–c, e–f) show a narrowing of the misfit distributions for both temperature and salinity, especially in the AW layer below 250 m.

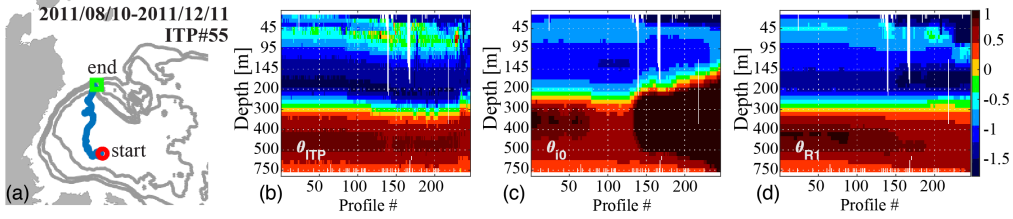


**Figure 11.** ITP #55 (a) trajectory, (b) potential temperature  $\theta$  for all observed profiles along the trajectory, and the model equivalent for (c) *it0* and (d) *ASTE\_R1*. In (a), the red circle and green square mark the first and last profile positions.

581 trol variables, i.e., the initial hydrography in 2002, time-averaged internal mixing param-  
 582 eters, and surface atmospheric forcing. As a result, a “near-perfect” fit, such as that of  
 583 the WOA18 hydrography to the mean ITP data seen in Fig. 1, is not possible for this  
 584 under-determined problem. The fit is, nevertheless, within the specified temperature and  
 585 salinity uncertainties, with improved watermass representation for all ITP data (e.g., Fig. 11),  
 586 Beaufort Gyre Moorings, NABOS moorings, and Fram Strait moorings.

### 587 3.2 The Greenland Iceland Norwegian Seas

588 The Greenland-Iceland-Norwegian (GIN) Seas are defined here as bounded to the  
 589 south by the Greenland-Scotland Ridge (GSR) and to the north and north east by the  
 590 Fram Strait and the Barents Sea Opening, respectively (see Fig. 12b). The sea ice near  
 591 Fram Strait and along the East Greenland coast is seasonal and the largest misfits in *it0* were  
 592 due to excessive ice here, including the Odden ice tongue (Wadhams et al., 1996) reach-  
 593 ing further to the east during winter months (Fig. 7c–d and Fig. 12a). Surface winds and  
 594 air temperature have been found to play an important role in controlling the eastern ext-  
 595 ent of the ice edge in this region (Germe et al., 2011; Moore et al., 2014). Adjustments

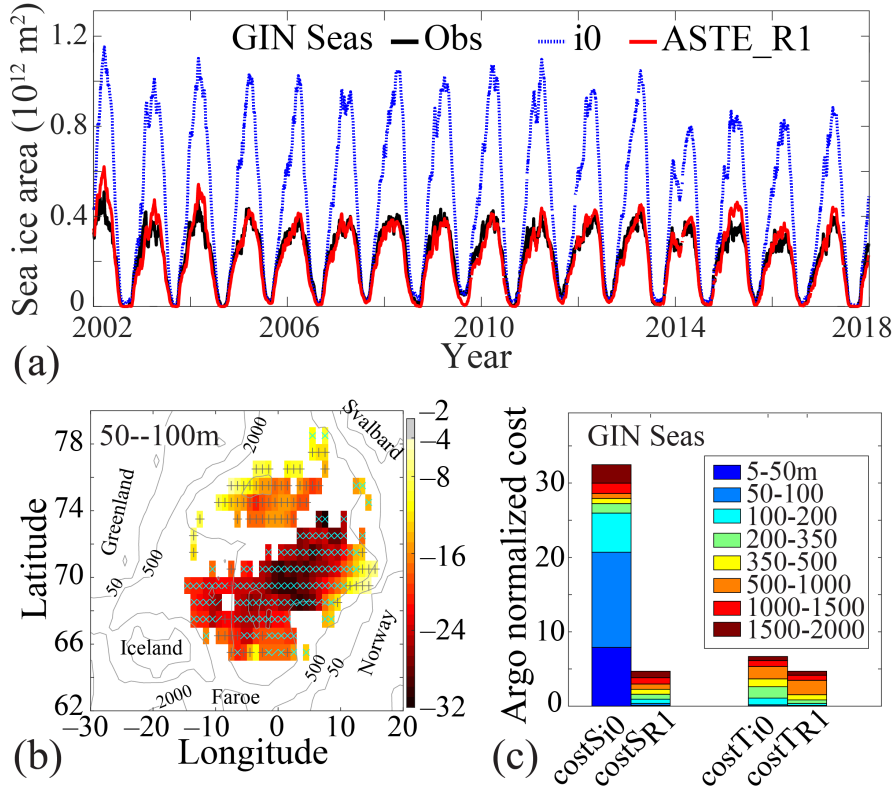


**Figure 12.** Improvements in GIN Seas sea ice and hydrography in *ASTE\_R1* compared to *it0*. (a) Time-series of daily sea ice area for OSSISaf observations (black), *it0* (blue) and *ASTE\_R1* (red). (b) Normalized misfits in salinity in the GIN Seas at depths 50–100 m, defined as  $(S_m - S_o)/\sigma_S$ , where “m” and “o” are model and observed Argo. For *it0*, which has a large negative bias, dimensionless misfits are indicated by the color scale ranging from  $-32$  to  $-2$ . For *ASTE\_R1*, in which the negative bias still persists but at significantly reduced amplitudes, the dimensionless misfits are indicated by symbols, with “x” and “+” corresponding to ranges  $[-6, -2]$  and  $[-2, 0]$ , respectively. The breakdown of cost reductions for all other depth ranges are shown in (c) for the GIN Seas, with overall reductions of costs of 81% and 19% in salinity and temperature relative to Argo data.

596 of these atmospheric state variables during the optimization, within their specified un-  
 597 certainties, drove a reduction in sea ice area (Fig. 12a) to improve the model-data fit.

598 The Nordic Seas host the interaction of several important watermasses. Warm and  
 599 salty Atlantic water enters across the GSR along three major branches, meeting locally  
 600 modified water recirculating in the Lofoten, Greenland and Iceland Basins, and the south-  
 601 ward flowing cold, fresh East Greenland Coastal Current (Hansen & Østerhus, 2000).  
 602 This region is characterized by very weak stratification, resulting in a very small defor-  
 603 mation radius of 4–7 km throughout the region (Nurser & Bacon, 2014), which further  
 604 challenges realistic representation of watermass distribution in models (Drange et al., 2005;  
 605 Heuzé & Årthun, 2019) and *ASTE\_R1*. Nevertheless, the improvements obtained in *ASTE\_R1*  
 606 are substantial, with overall reductions of  $\sim 85\%$  and  $30\%$  for salinity and temperature  
 607 costs, respectively, through the 2000 m water column (Fig. 12c). The largest improve-  
 608 ments are associated with reduction of a fresh bias in the upper 100 m (Fig. 12b–c), across

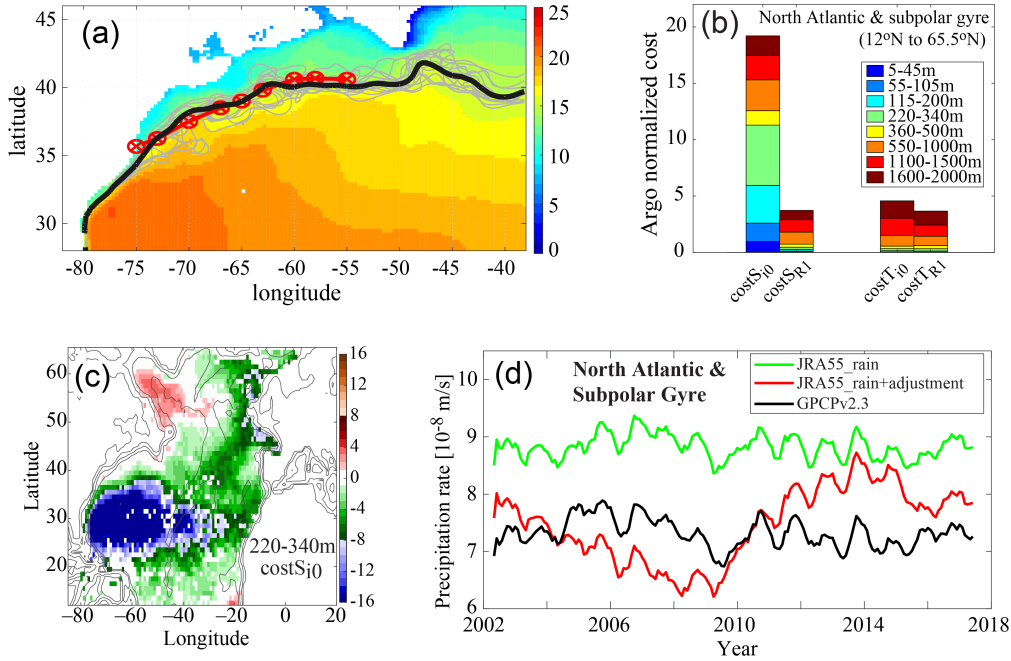


**Figure 13.** (a) The 2002–2017 mean proxy path of the Gulf Stream in *ASTER1* (black) and the World Ocean Atlas 2009 mean 15°C isotherm at 200 m depth (red, Wolfe et al. (2019)). The gray lines are the paths in *ASTER1* for each year. (b) Normalized cost for salinity and temperature in the North Atlantic and subpolar gyre region (latitudes 12°N–65.5°N) for *it0* and *ASTER1* as a function of depth range. (c) Normalized misfits in *it0* (relative to observed Argo salinity) in the water column at depth range 220–340 m. (d) Net precipitation into the North Atlantic and subpolar Gyre from JRA55 (Kobayashi et al., 2015), observational based product GPCPv2.3 (Adler et al., 2018), and adjusted rain used to force *ASTER1*.

609 the Lofoten, Iceland, and Greenland basins, which are important regions for deep wa-  
 610 ter formation.

### 611 3.3 The Subpolar Gyre and North Atlantic

612 Although the primary focus of the study is on the assessment of *ASTER1* in the  
 613 Arctic Mediterranean, the North Atlantic ocean serves as both the source of near sur-  
 614 face heat and salt to the Arctic and the sink of dense deep water and surface freshwa-  
 615 ter from the Arctic Mediterranean, and so will be briefly assessed here.

616 One of the greatest challenges in modeling the North Atlantic is to correctly sim-  
 617 ulate the observed Gulf Stream pathway. Capturing a realistic Gulf Stream separation  
 618 is non-trivial in  $z$ -level numerical models (Ezer, 2016; Chassignet & Xu, 2017). In *ASTE*,  
 619 a combination of coastal biharmonic and off-shore Leith viscosity as described in Sec-  
 620 tion 2.1 was used to achieve an observationally-consistent mean Florida Strait transport  
 621 of  $\approx 32 Sv$  (Baringer & Larsen, 2001; Johns et al., 2002) and a separation near Cape  
 622 Hatteras. After separation, the Gulf Stream path can be approximately tracked using  
 623 a proxy of the 15°C isotherm at 200 m depth (from the WOA13, Wolfe et al., 2019). Fig. 13a  
 624 shows this proxy of the Gulf Stream path for the years 2002–2017 in *ASTER1* compared  
 625 to that derived from WOA13.

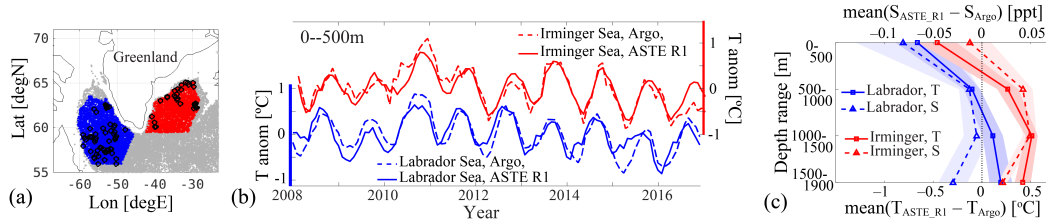


**Figure 14.** (a) Distribution of Argo data in the Irminger Sea (red dots) and Labrador Sea (blue dots) for the full period 2002–2017. To provide an impression of temporal coverage, black circles show data acquired within the month of January 2016. (b) Upper 500 m ocean mean temperature anomalies for the Labrador Sea (blue) and Irminger Sea (red) from Argo observations (dashed) and *ASTER1*. Anomalies are defined as the full time-series minus its respective mean, showing that *ASTER1* captures both the seasonal and interannual ocean temperature variability in both the Irminger and Labrador Seas. The biases are shown in (c) for temperature and salinity at various depth ranges sampled by Argo.

626 The dynamical mechanisms underlying the transports of warm AW from the Gulf  
 627 Stream extension to the subpolar North Atlantic (SPNA) and into the GIN Seas across  
 628 the GSR is poorly understood and its representation in state-of-the-art models remains  
 629 a great challenge (Heuzé & Årthun, 2019). Compared with Argo data, the eastern SPNA  
 630 hydrography (south of the GSR) contains large biases in *it0* (Fig. 13b–c) but is signif-  
 631 icantly improved in *ASTER1*, with a net reduction of misfit over the entire North At-  
 632 lantic (north of 12°N) of ~80% and ~21% in salinity and temperature, respectively (Fig. 13b).  
 633 Closer inspection reveals that, just south of the GSR, in the Irminger and Labrador Seas,  
 634 *ASTER1* can reliably reproduce the observed hydrographic variability (Fig. 14a–b). How-  
 635 ever, the solution exhibits a widespread systematic warm bias between 500–2000 m un-  
 636 derlying a cold bias in the upper ~500 m over the subpolar region (shown for the Labrador  
 637 and Irminger Seas in Fig. 14c). Overall, salinity is biased fresh in the Labrador Sea, whereas  
 638 a salty bias characterizes the Irminger Sea (Fig. 14c) and the wider eastern subpolar North  
 639 Atlantic region (not shown).

640 In the subtropical North Atlantic, a large fraction of the salinity misfit in *it0* is due  
 641 to an excess freshwater flux from the atmosphere. Comparison to the independent Global  
 642 Precipitation climatology Project version 2.3 product (GPCPv2.3, Adler et al., 2018) re-  
 643 veals an excess precipitation bias in JRA55, that is most pronounced in the North At-  
 644 lantic and subpolar gyre region of the *ASTE* domain (Fig. 13d), and that resulted in a  
 645 large fresh bias in the upper ~500 m of the unconstrained *it0* solution (Fig. 13c). The  
 646 adjoint-based optimization provided a systematic approach for removing this excess pre-  
 647 cipitation bias, such that after approximately 12 iterations the misfits to Argo salinity  
 648 in the upper ocean reduced to within the observed uncertainty (Fig. 13b). Consequently,  
 649 this improvement also yields better agreement in the mean with an independent GPCPv2.3  
 650 data set (Fig. 13d). It is important to stress again that these adjustments are made whilst  
 651 retaining the ocean model dynamical and kinematical consistency.

#### 652 4 Transports through Key Oceanic Gateways and Regional Storage

653 Complementing the assessment of *ASTER1* in terms of residual model-data mis-  
 654 fit (previous section), we provide in the following an initial comparison of widely used  
 655 oceanographic indices, including volume, heat, and freshwater transports across impor-  
 656 tant Arctic and GIN Seas gateways (Table 4, Fig. 15–17) to all known observation-based  
 657 estimates (Skagseth et al., 2008; Schauer & Beszczynska-Möller, 2009; de Steur et al.,

<i>Transports</i>				
Gate	Volume [Sv]	Heat [TW]	FW [mSv]	
(1)Bering Strait	1.11 ± 0.35	4.70 ± 7.25	54.24 ± 20.62	
(2)CAA	-1.72 ± 0.39	7.95 ± 2.99	-94.19 ± 31.60	
(3)Fram Strait	-1.50 ± 0.66	54.15 ± 13.24	-84.83 ± 23.29	
(4)Svalbard-FJL <sup>1</sup> -SZ <sup>2</sup>	2.04 ± 0.64	-0.85 ± 8.03	45.23 ± 31.14	
(5)Barents Sea Opening	1.98 ± 0.66	62.33 ± 15.06	-3.25 ± 3.30	
(6)Davis Strait	-1.72 ± 0.39	25.40 ± 4.71	-103.32 ± 19.59	
(7)Denmark Strait	-2.00 ± 0.76	11.92 ± 7.81	-42.61 ± 12.21	
(8)Iceland-Faroe	2.26 ± 0.90	119.11 ± 24.09	-0.29 ± 0.69	
(9)Faroe-Shetland	0.71 ± 1.30	95.00 ± 38.12	6.25 ± 4.29	
(10)Newfoundland-Gr	-1.74 ± 0.38	67.30 ± 17.41	-110.67 ± 23.44	
(11)48.3°N	-1.39 ± 0.36	449.66 ± 75.75	-111.60 ± 22.80	

<i>Heat Budget [TW]</i>				
Domain	Lateral conv	Vertical conv	Tendency	Bounded Gates
Arctic	65.95 ± 13.57	-39.53 ± 39.48	26.39 ± 41.34	1,2,3,4
CAA	17.46 ± 5.84	-18.08 ± 12.55	-0.63 ± 15.60	2,6
Barents	63.18 ± 19.94	-63.63 ± 37.27	-0.45 ± 47.98	4,5
GINs	109.55 ± 34.28	-110.06 ± 60.55	2.19 ± 78.36	3,5,7,8,9
Labrador Sea	41.90 ± 16.81	-49.40 ± 39.83	-7.50 ± 47.30	6,10
East SPNA	156.33 ± 96.91	-146.97 ± 92.94	6.65 ± 165.61	7,8,9,10,11

<i>FW Budget [mSv]</i>				
Domain	Lateral conv	Vertical conv <sup>a</sup>	Tendency	Bounded Gates
Arctic	-79.55 ± 40.31	74.57 ± 10.28	-9.45 ± 35.83	1,2,3,4
CAA	-9.13 ± 26.29	5.78 ± 2.86	-0.51 ± 22.68	2,6
Barents	-48.48 ± 30.96	57.54 ± 7.89	-4.17 ± 30.29	4,5
GINs	51.43 ± 23.16	34.52 ± 17.74	1.20 ± 16.89	3,5,7,8,9
Labrador Sea	-7.35 ± 23.15	20.55 ± 9.58	4.56 ± 22.35	6,10
East SPNA	35.72 ± 16.92	93.94 ± 26.42	2.41 ± 20.32	7,8,9,10,11

**Table 4.** *ASTER1* budgets of volume, heat ( $\theta_r = 0^\circ\text{C}$ ), and FW ( $S_r=34.8$  ppt) for the combined ocean and ice system for the period 2006–2017. All uncertainties provided are given in terms of standard deviations based on monthly estimates after the seasonal climatology has been removed. FW transport is computed using eqn. (B3.2) of Appendix B. <sup>a</sup>The vertical convergence of FW, from air-ice-sea fluxes, is the same as that for volume and is exact. Lateral convergence and tendency of FW, however, are approximate. As a result, the budget for FW is not fully closed (see Appendix B). <sup>1</sup> Franz Josef Land, <sup>2</sup> Severnaya Zemlya.

2009; Beszczynska-Möller et al., 2011; Curry et al., 2011, 2014; Hansen et al., 2015; Woodgate, 2018; Rossby et al., 2018; Østerhus et al., 2019). Where available, we also assess *ASTER1* transports against previously published estimates from coordinated modeling studies (Q. Wang et al., 2016b, 2016a; Ilicak et al., 2016; Heuzé & Årthun, 2019), ocean reanalyses (Uotila et al., 2019), and an independent inverse estimate (Tsubouchi et al., 2018).

The published literature offers notable differences in tracer reference values employed in the computation of reported heat, freshwater and volumetric watermass transports. These range from regional basin means (Smedsrud et al., 2010; Beszczynska-Möller et al., 2012; de Steur et al., 2018; Tesdal & Haine, 2020) to gateway and surface means (Tsubouchi et al., 2018) to freezing temperature in the Arctic (Beszczynska-Möller et al., 2012; Woodgate, 2018). In some cases, transports were computed along a particular range of isopycnals (Tsubouchi et al., 2018). Heat transport computed in *ASTER1* assumes a reference temperature  $\theta_r = 0^\circ\text{C}$  (most accurate numerically, see Appendix B). For the Bering Strait, we also compute heat transport referenced to the freezing temperature of seawater  $\theta_r = -1.9^\circ\text{C}$  to facilitate comparison with published estimates. For the computation of freshwater transports, we assume a reference salinity  $S_r = 34.8$  ppt and integrate from the surface down to the reference isohaline. We refer the reader to Appendix B for details on potential errors incurred when computing transports using non-zero reference values. Due to the difference in reference values employed here and in some of the studies listed above, we seek consistency in terms of comparable transport magnitudes as opposed to exact agreement.

To provide a useful comparison of *ASTER1* mean transports with those reported in the literature, it is important to note whether published estimates are based on historic data or more recent acquisitions, given how fast the high latitudes are observed to be changing. In the first four years of the *ASTER1* period, 2002–2005, transports in both the North Atlantic and the Arctic exhibit distinctly different characteristics compared to the period 2006–2017. This transition of hydrographic properties and circulation patterns around 2005–2006 has been extensively discussed, with studies noting a strong increase in volume and heat transports into the Barents Sea (Skagseth et al., 2008), increased salinity and density in the lower halocline in the Eastern Arctic (Dmitrenko et al., 2011), abrupt changes in North Atlantic heat (Piecuch et al., 2017; Foukal & Lozier, 2018) and freshwater (Dukhovskoy et al., 2019) content, and rapid freshening of the Nordic Seas (Tesdal & Haine, 2020). To avoid averaging over these two apparently distinct regimes, we chose to report all mean transports for the most recent period, following the abrupt transition. Reported associated standard deviations to the 2006–2017 mean transports are computed based on the monthly values after the seasonal cycle has been removed. Details of the calculation of *ASTER1* transports are given in Appendix B, and watermass definitions are given in Appendix C.

#### 4.1 Volume Transports

Østerhus et al. (2019) summarized existing estimates of volume transports across the main Arctic–Nordic Seas gateways, including the Bering Strait (BS), Davis Strait (DaS), and the Greenland–Scotland Ridge (GSR). The latter comprises the Denmark Strait (DS), Iceland–Faroe channel (IF) and Faroe–Shetland channel (FSh). Time-mean transports in *ASTER1* are given in Table 4 and Fig. 15, listed alongside previously published estimates from observations (Beszczynska-Möller et al., 2012; de Steur et al., 2014; Beszczynska-Möller et al., 2011; Woodgate, 2018; Curry et al., 2014; Skagseth et al., 2008; Hansen et al., 2015), and modeling studies (Tsubouchi et al., 2018; Heuzé & Årthun, 2019; Ilicak et al., 2016). In addition to net transports, we also provide estimates of transports of important watermasses at Fram Strait (as defined in Beszczynska-Möller et al., 2011) and through the GSR (as defined in Hansen & Østerhus, 2000; Østerhus et al., 2019). For the in/outflow transport estimates given in Fig. 15, we follow watermass definitions of Beszczynska-Möller et al. (2012) for Fram Strait and Østerhus et al. (2019) for the GSR.

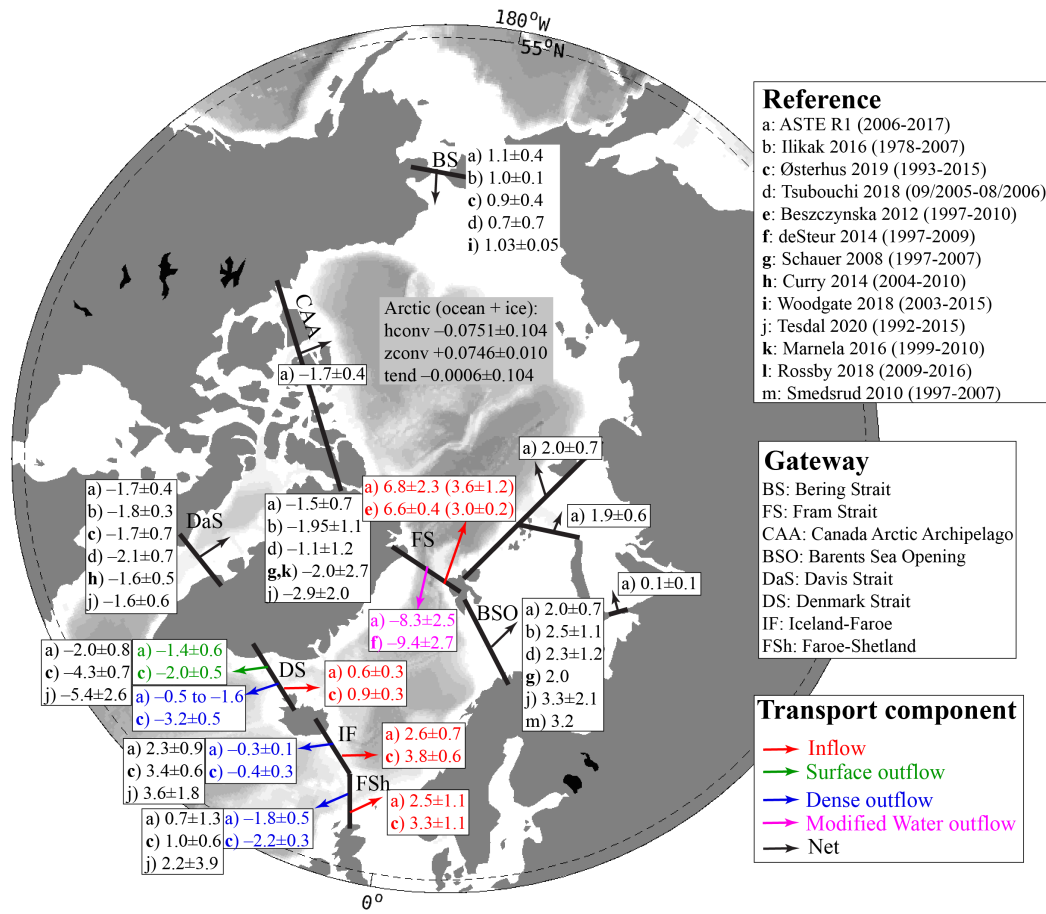


**Figure 15.** Volume transports across important Arctic and Nordic Seas gateways listed for (a) *ASTE\_R1* and (b-m) published estimates referenced in the legend. Net transports across the full width and depth of each section are written in black; transport component contributions to this total are written in color for (red) total inflow, (green) surface outflow, (blue) dense outflow, and (magenta) modified water outflow, where arrows show the direction ascribed to in/outflow. Positive (negative) transport indicates Northward and Eastward (Southward and Westward). Quantities listed are 2006–2017 mean and standard deviation after the seasonal cycle has been removed. All net transports in *ASTE\_R1* are diagnosed online, while separate transport components through FS, DS, IF, and FSh are diagnosed offline using archived monthly advection terms. See text and Appendix C for further discussion on watermass identification used in determining the in/outflow transport components. For Fram Strait inflow, the two provided estimates are for the West Spitsbergen current only, and we give both the total current transport and, in parenthesis, the fraction above  $2^\circ\text{C}$  (Beszczynska-Möller et al., 2011). Numbers in parentheses in the Reference legend refer to the period covered by the respective studies.

710 All uncertainties provided are given in terms of standard deviations based on monthly  
711 estimates after the seasonal climatology has been removed.

712 The net volume transport of approximately  $1.1 \pm 0.4$  Sv across the Bering Strait  
713 is northward into the Arctic. Across the Davis Strait, there is a southward transport of  
714 freshwater near the surface and northward transport of warm water from the Irminger  
715 Current (Curry et al., 2014). At this gate, *ASTE\_R1* estimates a net volume transport  
716 of  $1.7 \pm 0.4$  Sv, consistent with observed values of  $1.6 \pm 0.5$  and  $1.7 \pm 0.7$  from Curry  
717 et al. (2014) and Østerhus et al. (2019), respectively. Across the GSR, there is a net near-  
718 surface northward transport of AW across the Denmark Strait (DS), Iceland-Faroe (IF)  
719 and Faroe-Shetland (FSh) channels (shown in red in Fig. 15), southward surface flow of  
720 freshwater across DS and dense overflow across the entire ridge (green and blue color in  
721 Fig. 15).

722 Watermass definitions for surface outflow, dense outflow, modified water, and in-  
723 flow AW in *ASTE\_R1* can differ from Østerhus et al. (2019) and Hansen and Østerhus  
724 (2000) for the reasons outlined in Section 2.3. Our choice for  $\sigma_\theta$  is justified in Appendix  
725 C. For the overflow through DS, the range of  $27.4 \leq \sigma_\theta \leq 27.8$  used in *ASTE\_R1* is  
726 associated with southward transports of  $-1.6 \pm 0.9$  to  $-0.5 \pm 0.3$  Sv (shown in blue  
727 in Fig. 15), corresponding to 16%–50% of the observed estimate using  $\sigma_\theta = 27.8$  from  
728 Østerhus et al. (2019). Similar considerations for  $\sigma_\theta$  of dense overflow water across the  
729 IF and FSh ridges (Appendix C) yield  $-0.3 \pm 0.1$  Sv and  $-1.8 \pm 0.5$  Sv, respectively,  
730 in *ASTE\_R1*, compared to  $-0.4 \pm 0.3$  Sv and  $-2.2 \pm 0.3$  Sv of water with  $\sigma_\theta \geq 27.8$   
731 in Østerhus et al. (2019). For surface outflow, *ASTE\_R1* underestimates the observed  
732 estimate at the DS by approximately 30%. In total, the net volume transport across DS  
733 in *ASTE\_R1* is about 47% of that reported by Østerhus et al. (2019).

734 For the Arctic Ocean and GIN Seas heat and freshwater budgets, transports through  
735 Fram Strait (FS) and the Barents Sea Opening (BSO) are also important. Across FS,  
736 the inflow of warm AW along the West Spitsbergen Current (red color in Fig. 15) is  $6 \pm$   
737  $1$  Sv in *ASTE\_R1*, with  $3.4 \pm 1.1$  Sv carrying the core AW water warmer than  $2^\circ\text{C}$ .  
738 This is consistent with corresponding estimates of  $6.6 \pm 0.4$  and  $3.0 \pm 0.2$  from Beszczynska-  
739 Möller et al. (2012) based on observations from an earlier period of 1997–2010. The out-  
740 flow across FS includes freshwater carried by the East Greenland Current at the surface  
741 and return of modified AW at depth (magenta color in Fig. 15, Beszczynska-Möller et  
742 al., 2011). For the southward return of modified AW, *ASTE\_R1* estimates a flux of of  
743  $-8.3 \pm 2.5$  Sv over the period 2006–2017, consistent with  $-9.4 \pm 2.7$  Sv from de Steur  
744 et al. (2014) for the period 1997–2009. Across the BSO, volume transport is dominated  
745 by the eastward Norwegian Coastal Current and the Atlantic inflow which carries warm  
746 AW into the Barents Sea (Smedsrud et al., 2010). The net eastward volume transport  
747 in *ASTE\_R1* of  $2.0 \pm 0.7$  Sv is consistent with observation-based estimate of  $\sim 2.0$  Sv  
748 from Smedsrud et al. (2010).

## 749 4.2 Heat Transports

750 All *ASTE\_R1* net heat transports are northward into the Arctic Basin. Time-mean  
751 transports across key gateways are consistent with observation-based estimates, a result  
752 that is aided – although by no means guaranteed – by constraining the state estimate  
753 using mooring  $T/S$  data (Table 4, Fig. 16).

754 At Bering Strait *ASTE\_R1* heat transport is  $14 \pm 8$  TW (referenced to  $T_r = -1.9^\circ\text{C}$ ),  
755 consistent with the 11.6 TW to 14.3 TW range determined by Woodgate (2018). At Davis  
756 Strait, the *ASTE\_R1* estimate of  $20 \pm 4$  TW is consistent with  $20 \pm 9$  TW obtained  
757 by Curry et al. (2011). Across the GSR, heat transport is in good agreement with pre-  
758 vious published estimates across the two eastern channels (IF and FS, Fig. 16), but is  
759 underestimated across the Denmark Strait. Here, the total poleward diffusive heat flux  
760 dominates and opposes the equatorward advective term in *ASTE\_R1*. This diffusive dom-

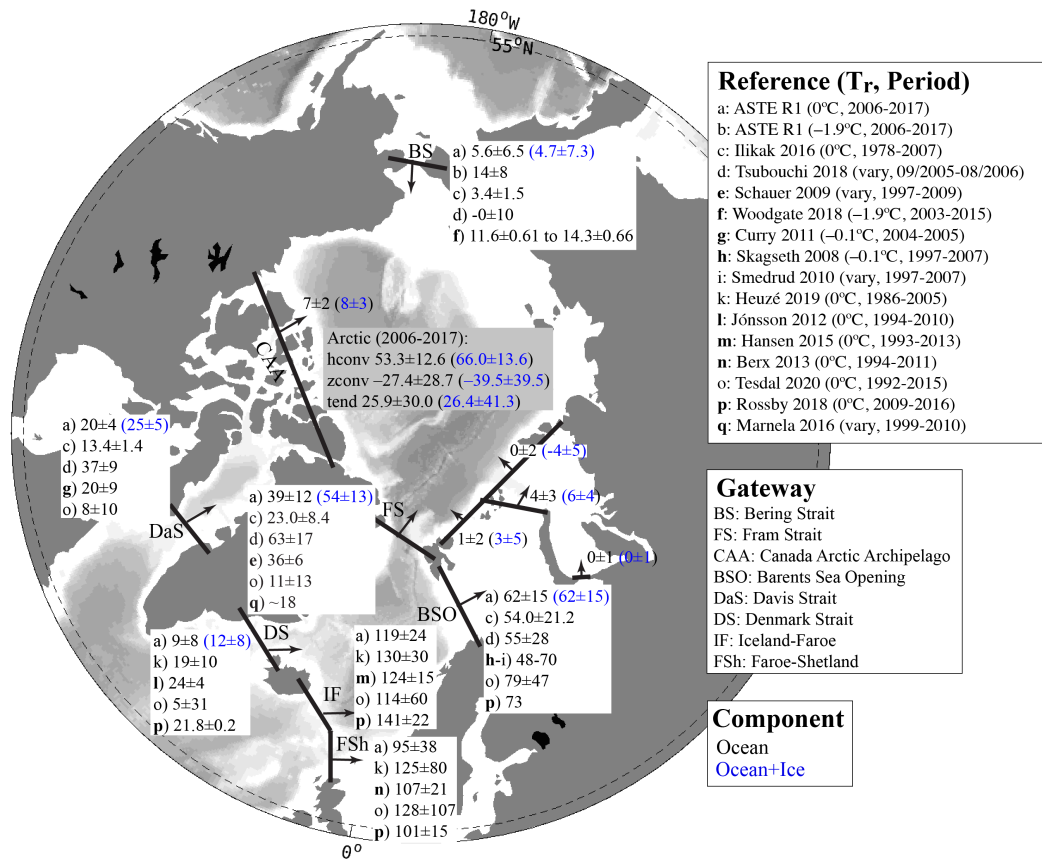


**Figure 16.** As for Fig. 14 but showing net ocean heat transport across important Arctic and Nordic Seas gateways. For select gateways the combined ocean+ice heat transport is also given (in blue). *ASTER1* transports (listed under (a)) are computed assuming a reference temperature  $T_r=0^\circ\text{C}$ . For the Bering Strait we also provide *ASTER1* transports computed using  $T_r=-1.9^\circ\text{C}$  (listed under (b)). Since previously published estimates (c-q) vary in their choice of  $T_r$  (see main text) we assess agreement between estimates as consistency in order of magnitude. Positive (negative) transport indicates Northward and Eastward (Southward and Westward) flow. Quantities listed are 2006–2017 mean and standard deviation after the seasonal cycle has been removed. Numbers in parentheses in the Reference legend refer to the  $T_r$  used and the period covered by the respective studies.

761 inance has also been suggested using heat budget analyses in ECCOv4 (Buckley et al.,  
 762 2015). A more detailed discussion of the full time-series and contributions of advective  
 763 and diffusive fluxes to the total transport is given in Appendix B.

764 Further north, at Fram Strait, *ASTER1* poleward heat transport is  $39 \pm 12$  TW  
 765 (referenced to  $T_r=0^\circ\text{C}$ ), consistent with  $36 \pm 6$  TW from Schauer and Beszczynska-Möller  
 766 (2009) and Beszczynska-Möller et al. (2011). The Fram Strait heat transport is increased  
 767 by approximately one third (15 TW) on accounting for sea ice advection. Heat trans-  
 768 port into the Barents Sea across BSO of  $62 \pm 15$  TW is consistent with observa-  
 769 tion-based estimates of between 48 TW and 73 TW (Skagseth et al., 2008; Smedrud et al.,  
 770 2010; Rossby et al., 2018). Most of this heat is lost via air-sea exchange in the Barents  
 771 and Kara Seas (Lind et al., 2018), yielding negligible heat transports from this shallow  
 772 region into the Arctic Basin (Fig. 16). Air-sea exchange also accounts for significant loss

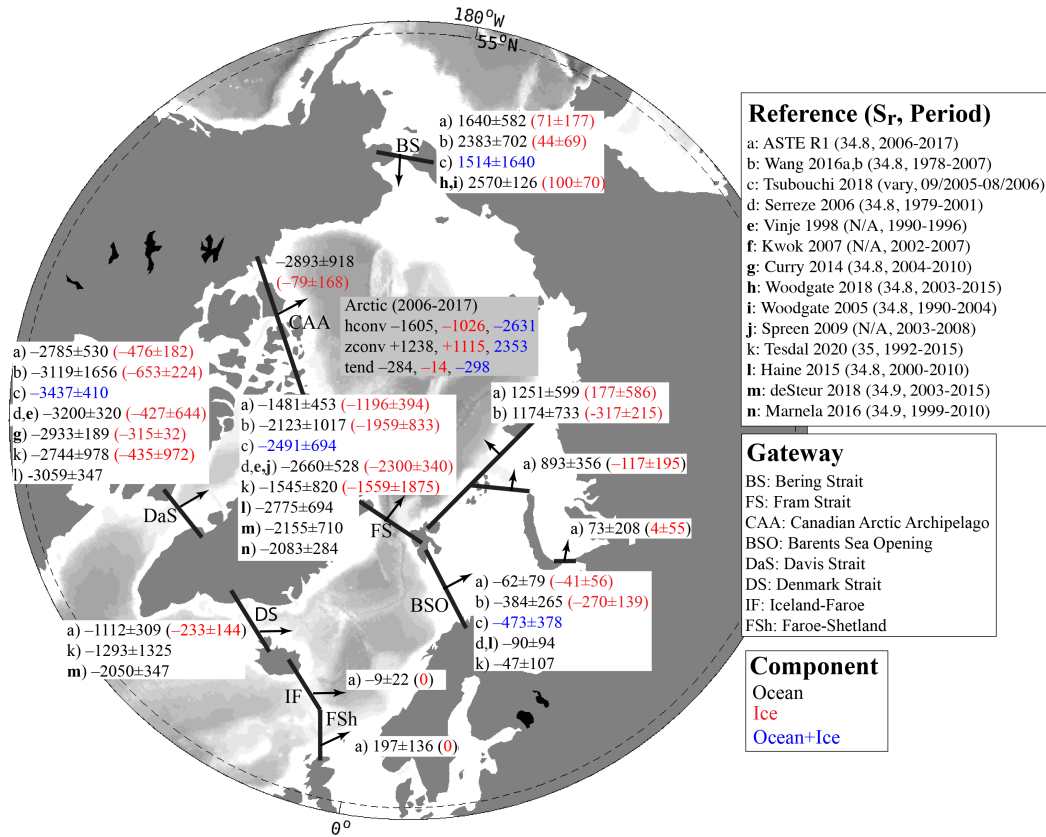


**Figure 17.** FW flux across important Arctic and Nordic Seas gateways from (a) *ASTE\_R1* and (b-n) published estimates. Units are in  $\text{km}^3 \text{yr}^{-1}$ .  $S_r=34.8$  ppt is used in *ASTE\_R1* calculations for all FW transports and content/tendency terms for the ocean. A fixed salinity  $S_r=4$  ppt is used for sea ice transports and tendency terms. Positive (negative) values indicate Northward and Eastward (Southward and Westward) transports. Quantities listed are 2006–2017 mean and standard deviation after the seasonal cycle has been removed. Numbers in parentheses in the Reference legend refer to the  $S_r$  used and the period covered by the respective studies.

773 of heat in the Canadian Arctic Archipelago, such that only  $\sim 35\%$  of the amount trans-  
 774 ported across the Davis Strait reaches the Arctic Basin.

775 There is a large spread amongst existing observation- and model-based studies with  
 776 significant disagreements even after accounting for uncertainty (Fig. 16), due in part to  
 777 the lack of common data period and reference temperature used in the calculations. Over-  
 778 all, nevertheless, the poleward heat transports in *ASTE\_R1* are in good agreement with  
 779 previous estimates (Fig. 16).

### 780 4.3 Freshwater Transports

781 The practice of reporting ocean freshwater (FW) transport/content in place of ab-  
 782 solute salt transport/content is ubiquitous in the literature, but plagued by the need to  
 783 specify a reference salinity,  $S_r$ , and to choose the vertical extent over which the integral  
 784 is computed (i.e., full depth versus to the depth of the reference salinity,  $z_{S_r}$ ). No unique  
 785 choice emerges from consideration of seawater physics. Instead,  $S_r$  is selected inconsis-  
 786 tently between studies. As cautioned by Schauer and Losch (2019), this not only com-

787 plicates comparisons but can give very different impressions of the changing ocean state,  
 788 due to strong sensitivity to the choice of  $S_r$ . Acknowledging this issue, we nevertheless  
 789 elect to report FW transport below (as did Tesdal and Haine (2020) in their recent study  
 790 focusing on the subpolar North Atlantic and Nordic Seas), in order to conduct our as-  
 791 sessment of *ASTER1* hydrography in the context of existing estimates. To the best of  
 792 our knowledge no published observational estimates report Arctic salt transports that  
 793 would provide a basis for comparison (the modeling study by Treguier et al., 2014 is one  
 794 known exception). We proceed with caution and flag comparisons for which calculations  
 795 differ. *ASTER1* FW fluxes are reported using a reference salinity of  $S_r=34.8$  ppt and  
 796 integrated down to  $z_{S_r}$ . Our calculation uses monthly averages of both the Eulerian ve-  
 797 locity and salinity. In Appendix B we provide a detailed discussion of the potential er-  
 798 rors in FW calculations with these choices, along with errors incurred in omitting bo-  
 799 lus and diffusive terms. Salt transport or salt content changes in *ASTER1* will be re-  
 800 visited in future work.

801 Similar to our assessment of volume and heat transports, we start by examining  
 802 FW transports across the gates into the Arctic Mediterranean. At the Bering Strait, *ASTER1*  
 803 combined liquid and solid FW import of  $1711 \pm 608$  km<sup>3</sup>/yr is lower than the  $2670 \pm$   
 804  $144$  km<sup>3</sup>/yr estimated by Woodgate et al. (2015) and Woodgate (2018). There are sev-  
 805 eral candidates to explain this  $\sim 960$  km<sup>3</sup>/yr FW transport deficit at this gate. Most im-  
 806 portantly, the river runoff climatology used in *ASTER1* has likely not taken into ac-  
 807 count potential increased discharge from the Yukon River into the Bering Sea just up-  
 808 stream of the strait (Toohey et al., 2016; Holmes et al., 2012). Another likely candidate  
 809 is any remaining error in the wind forcing. Nguyen et al. (2020b) showed that wind stress  
 810 in both the Pacific and Arctic sectors play an important role in controlling the Bering  
 811 Strait volume transports and reliably modelling the transport trends observed in Woodgate  
 812 (2018), which are not present in the volume and FW transport here in *ASTER1* (Nguyen  
 813 et al., 2020b).

814 At Davis Strait, *ASTER1* liquid and solid FW exports of  $-2785 \pm 530$  km<sup>3</sup>/yr  
 815 and  $-476 \pm 182$  km<sup>3</sup>/yr are consistent with estimates of  $-2933 \pm 189$  km<sup>3</sup>/yr and  $-315 \pm$   
 816  $32$  km<sup>3</sup>/yr from Curry et al. (2014), on accounting for uncertainty/variability. Freshwa-  
 817 ter transports across the Iceland-Faroe and Faroe-Shetland channels are negligible. At  
 818 Denmark Strait, *ASTER1* estimate of  $-1112 \pm 309$  km<sup>3</sup>/yr is approximately half of  
 819 the value reported by Marnela et al. (2016) of  $-2050 \pm 347$  km<sup>3</sup>/yr. This is consistent  
 820 with the 50% underestimation of both volume and heat transports in *ASTER1* across  
 821 this gate compared to independent observations.

822 Further north, at Fram Strait, the liquid and solid FW exports of  $-1465 \pm 463$   
 823 km<sup>3</sup>/yr and  $-1195 \pm 394$  km<sup>3</sup>/yr in *ASTER1* are lower than the  $-2150 \pm 710$  km<sup>3</sup>/yr  
 824 liquid and  $-2300 \pm 340$  km<sup>3</sup>/yr solid FW exports estimated by de Steur et al. (2009)  
 825 and Spreen et al. (2009), respectively. A main reason for the lower (by  $\sim 1800$  km<sup>3</sup>/yr)  
 826 liquid plus solid export in *ASTER1* across Fram Strait is the lower (by  $\sim 960$  km<sup>3</sup>/yr)  
 827 net FW import through the Bering Strait relative to observations. An additional incon-  
 828 sistency is the use of a runoff climatology in *ASTER1*, which fails to account for Green-  
 829 land solid/liquid discharge and its observed recent increase into the Arctic sector by ap-  
 830 proximately 105 km<sup>3</sup>/yr (Bamber et al., 2012), as well as increased river outputs (as re-  
 831 ported in Bamber et al., 2012; Proshutinsky et al., 2020). With respect to the latter, *ASTER1*  
 832 has a deficit of  $\sim 220$  km<sup>3</sup>/yr. The climatology also does not account for Greenland FW  
 833 (combined solid and liquid) discharge into the GIN Seas and Baffin Bay of nearly 150 km<sup>3</sup>/yr  
 834 and 250 km<sup>3</sup>/yr, respectively (Bamber et al., 2012). In the Canadian Arctic Archipelago,  
 835 *ASTER1* has a FW flux deficit of  $\sim 226$  km<sup>3</sup>/yr from land ice (Carmack et al., 2016).  
 836 These omissions likely contribute to the underestimation of southward FW transports  
 837 across both the Denmark Strait (by  $\sim 940$  km<sup>3</sup>/yr) and Davis Strait (by  $\sim 150$  km<sup>3</sup>/yr).

838 The net lateral convergence of the combined liquid and solid freshwater flux in *ASTER1*  
 839 of  $-2510 \pm 1272$  km<sup>3</sup>/yr is nearly balanced by the net vertical convergence of  $2353 \pm$

840 324 km<sup>3</sup>/yr, yielding a net tendency of  $-298 \pm 1131$  km<sup>3</sup>/yr. For the liquid flux alone,  
 841 the tendencies are  $-1484 \pm 1123$  for lateral convergence,  $1238 \pm 2478$  vertical conver-  
 842 gence, and  $-284 \pm 2169$  km<sup>3</sup>/yr total tendency.

843 **4.4 Heat and Freshwater Storage**

844 Complementing the transport estimates, we conclude our initial assessment of *ASTE\_R1*  
 845 with an overview of derived basin-scale 2002-2017 time-mean and time-variable heat and  
 846 freshwater budgets, focusing on comparisons between *ASTE\_R1* and existing estimates.  
 847 A full assessment of the mechanisms underlying Arctic Mediterranean and subpolar North  
 848 Atlantic heat and freshwater content change over the *ASTE\_R1* period will be addressed  
 849 in a separate study. As noted earlier, decisions made in our tracer transport/budget cal-  
 850 culations facilitate these comparisons but are non-unique. For freshwater transports/budgets  
 851 this introduces ambiguity that is best resolved prior to detailed dynamical investigation.

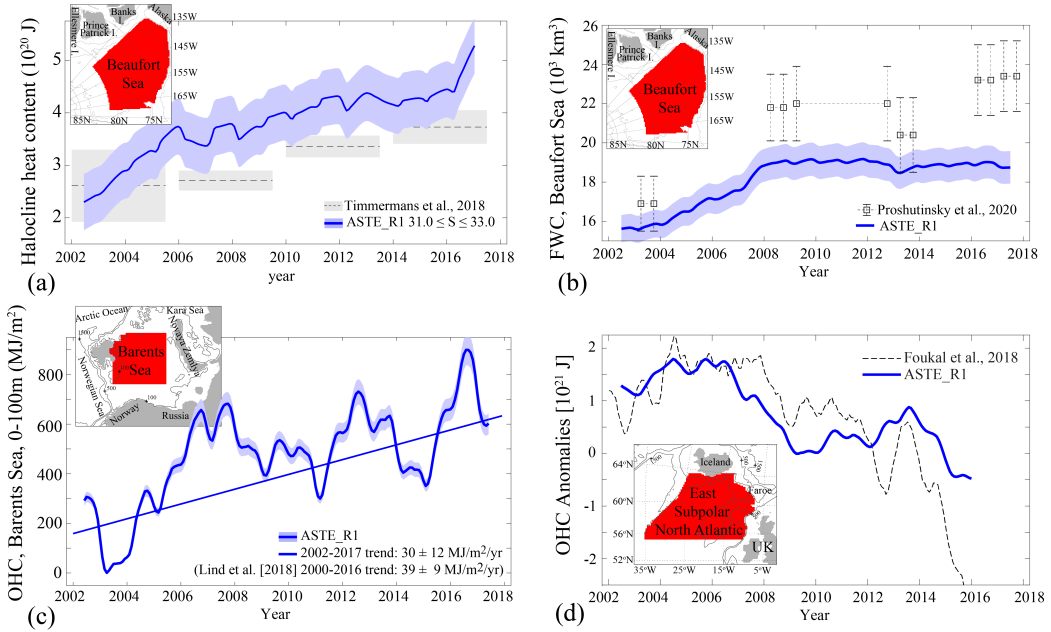


**Figure 18.** Comparison of *ASTE\_R1* (a) Beaufort Sea halocline (defined as  $31.0 \leq S \leq 33.0$ ) heat content, (b) Beaufort Sea freshwater content above the 34.8 ppt isohaline, (c) Barents Sea 0–100 m heat content and, (d) East Subpolar North Atlantic full-depth heat content with existing observational-based estimates, as given in the legend of each panel. Insets show the spatial mask defining each region. A 12-month running mean has been applied to filter the seasonal cycle from the *ASTE\_R1* time-series, facilitating comparison with observed trends. Shading in *ASTE\_R1* time-series indicate the sensitivity of the (a,c) heat content to a 5% change in (a) the northern and (c) eastern spatial mask, or the sensitivity of the (b) freshwater content to a 0.5 ppt change in the lower limit employed in the halocline watermass definition (see Appendix C).

852 **4.4.1 Heat Content**

853 Considering the Arctic region of *ASTE\_R1* in its entirety, the net heat input from  
 854 convergence of horizontal (ocean plus ice) heat transports ( $53.3 \pm 12.0$  TW) exceeds  
 855 the net heat loss due to local air-ice-sea fluxes ( $-27.4 \pm 28.7$  TW) by a factor  $\sim 2$ , yield-  
 856 ing a net heating rate of  $25.9 \pm 30.0$  TW when averaged over the period 2006–2017 (Ta-

ble 4). Relative to horizontal convergence, vertical exchange at the air-ice-sea interface is significantly less well constrained due to large uncertainties in atmospheric reanalyses at high northern latitudes (Beesley et al., 2000; Chaudhuri et al., 2014; C. Wang et al., 2019). Partitioned by basins, similar enthalpy gains are estimated for both the western ( $14.0 \pm 24.3$  TW) and eastern ( $12.5 \pm 14.0$  TW) Arctic region. In the water column, heat gain is concentrated mainly in the AW layer (240–1000 m) in both the western ( $9.3 \pm 2.7$  TW) and eastern ( $6.4 \pm 4.6$  TW) Arctic. In the upper 60 m of the water column, the tendency is negligible but with large variability ( $0.2 \pm 25.3$  TW) due to mixed layer processes and exchange with the atmosphere.

Warming since the early 2000s has been reported in the Arctic, documented alongside enhanced “Atlantification” in the Eastern Arctic (Polyakov et al., 2017, 2020) and a fivefold increase in solar absorption by near surface waters in the Western Arctic (Jackson et al., 2010; Timmermans et al., 2018). This warming proceeds at a sustained rate, with recent studies suggesting a doubling of OHC in the Beaufort Gyre halocline between 2003 and 2013 (Timmermans et al., 2018).

Fig. 18a shows a comparison of the time-series of the halocline heat content in *ASTER1* and estimates based on ITP and mooring data in the Beaufort Sea. As discussed in Section 2.3, adopting exact watermass classifications from observational studies may be inappropriate for model analysis, due to representation error of subgrid scales. Thus in addition to the salinity limits used to identify the upper halocline layer of  $31.0 \leq S \leq 33.0$  in Timmermans et al. (2018), we also compute the heat content sensitivity to the salinity bounds. By changing the near-surface lower salinity bound within the range 31–31.5 ppt, the mean halocline heat content changes by 2–3% per 0.1 ppt increment, but the variability and trend remain unchanged. This confirms that despite the systematic warm bias, the positive trend in halocline heat content is well-captured in the *ASTER1* solution.

In the Canada Basin, *ASTER1* exhibits a warming rate of  $9.3 \pm 2.7$  TW for the period 2006–2017 (Fig. 16). There are insufficient observations to validate this directly, but we can corroborate our estimate with a back of the envelope calculation as follows. Recent ITP acquisitions report core AW temperatures in this region  $\sim 0.5^\circ\text{C}$  warmer than the PHC climatology (Fig. 19a), where the latter is representative of the second half of the 20th century. Since ITPs only measure to  $\sim 800$  m depth, we conservatively assume a depth-average warming of  $0.20$ – $0.25^\circ\text{C}$  over the 170–1000 m range in the Western Arctic basin interior (area  $4400 \times 10^3$  km<sup>2</sup>), yielding a warming rate of  $\sim 5.7$ – $7.2$  TW, about two thirds of the rate estimated in *ASTER1*. Compared to ITP data, *ASTER1* shows a positive bias of  $\sim 0.15^\circ\text{C}$  in the core AW temperature in the Western Arctic basin, which accounts for the higher tendency here. However, we note that this *ASTER1* bias is within the combined data and representative error  $\sigma_T$ , which is not the case for the PHC bias (Fig. 19b).

The Eastern Arctic suffers from an extreme paucity of data, such that even back of the envelope estimates of basin-wide heat content (and its tendency) are not possible. Instead, we turn to recent observations for evidence of warming in this basin. Pulsed injection of AW at Fram Strait has been documented by Polyakov et al. (2011). A notable warm anomaly pulse of  $\sim 1^\circ\text{C}$  entered the Arctic in 2004. It has subsequently been observed crossing the NABOS section at  $126^\circ\text{E}$ , and has been recorded further downstream at numerous sections along the eastern basin’s rim (Polyakov et al., 2011). In addition, the seasonal amplitude within the halocline has been observed to increase by  $0.75^\circ\text{C}$  between 2004 and 2015 (Dmitrenko et al., 2009; Polyakov et al., 2017; Baumann et al., 2018). These observations provide evidence for a warming Eastern Arctic and a weakened halocline. The latter is accompanied by shoaling of the AW layer toward the bottom of the mixed layer and increasing heat ventilation (Polyakov et al., 2020). This is a mechanism by which heat along the AW pathway is removed instead of being sequestered at depth. To determine the relative importance of these two mechanisms (ventilation ver-

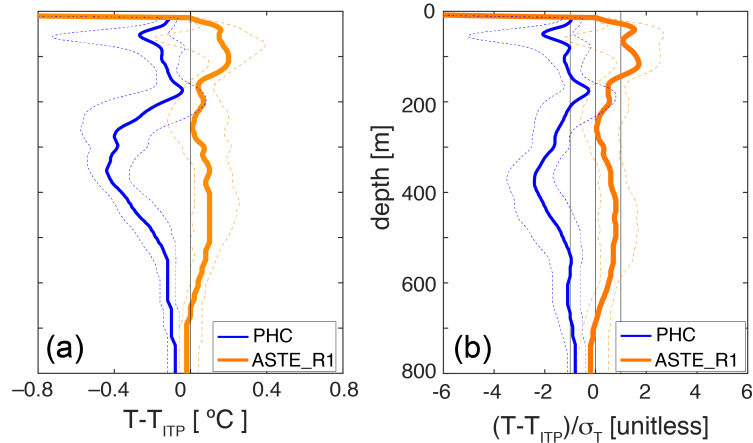


**Figure 19.** Comparison between all ITP-derived temperature profiles in the Canada Basin and PHC (blue) and *ASTE\_R1* (orange). Panel (a) shows the normalized 50th percentile difference (dimensionless) and (b) the 50-percentile difference ( $^{\circ}\text{C}$ ). The two vertical black lines in (b) at  $\pm 1$  indicate the limits within which the difference is within the uncertainty  $\sigma_T$ . The dotted lines show the 30th and 70th percentile differences.

910 sus sequestration) in contributing to the positive heat content tendency at different depths  
 911 and throughout the Arctic in *ASTE\_R1*, a more detailed analysis of AW circulation and  
 912 ventilation will be needed in future work.

913 In the Barents Sea, Lind et al. (2018) documented pronounced increases in decadal  
 914 mean OHC in the upper 100 m of the water column, which they attributed to an increase  
 915 in AW inflow through the Barents Sea Opening. In Fig. 18c we compare OHC trend (up-  
 916 per 100 m) from Lind et al. (2018) with *ASTE\_R1* illustrating that *ASTE\_R1* captures  
 917 the 2002–2016 positive trend. Further south, Piecuch et al. (2017) and Foukal and Lozier  
 918 (2018) have quantified OHC trends in the SPNA (between  $46^{\circ}\text{N}$  and  $65^{\circ}\text{N}$ ) using SST,  
 919 ECCOv4r3 and OHC derived from the Hadley Centre EN4 gridded product. The compar-  
 920 ison between Foukal and Lozier (2018) and *ASTE\_R1* (Fig. 18d) shows good quan-  
 921 titative agreement, with an increase in OHC between 2002–2005, a decrease in OHC be-  
 922 tween 2005–2009, and a hiatus between 2009–2014, followed finally by a further decrease  
 923 in OHC after 2014.

#### 924 4.4.2 Freshwater Content

925 Based on observations, predominantly from satellite altimetry and ITPs in the Beau-  
 926 fort Sea, the liquid freshwater content (FWC) in the Arctic has been estimated to be in-  
 927 creasing (Proshutinsky et al., 2019). Proshutinsky et al. (2020) summarized recent works  
 928 attributing this FWC increase to several factors, including shifts in atmospheric circula-  
 929 tion, increased FW fluxes through the Bering Strait, and increased runoff from the MacKen-  
 930 zie river. A comparison between *ASTE\_R1* and Proshutinsky et al. (2019) estimates for  
 931 FWC in the Beaufort Gyre shows that *ASTE\_R1* captures the observed increase in FWC  
 932 between the 2004 to 2008. With the exception of a small decrease in 2015 – also seen  
 933 in the observations – the Beaufort Gyre FWC in *ASTE\_R1* remains relatively constant  
 934 for the period 2008–2017 (Fig. 18b). Proshutinsky et al. (2019) report an increase from  
 935 2015–2017 which is likely missing from *ASTE\_R1* due to the omission of both increased  
 936 river runoff and land ice discharge in our forcing climatology and absence of the observed  
 937 increase in FW import through the Bering Strait as previously discussed (Fig 17).

938 The connection between the Arctic FWC increase and circulation changes in the  
 939 GIN Seas and North Atlantic has been the subject of several investigations (Dukhovskoy  
 940 et al., 2016; Carmack et al., 2016; Tesdal & Haine, 2020). A recent review by Haine et  
 941 al. (2015) summarized Arctic exchanges with the Canadian Arctic Archipelago (north  
 942 of Davis Strait) and the Barents Sea (east of the Barents Sea Opening). These estimates  
 943 heavily rely upon atmospheric reanalyses (for the provision of surface fluxes) and uncon-  
 944 strained model output (for tracer content change). Further south, Dukhovskoy et al. (2019)  
 945 investigated the redistribution of increased Greenland freshwater discharge (solid and  
 946 liquid) in the Subpolar North Atlantic (SPNA) and the GIN Seas, highlighting large un-  
 947 certainty due both to lack of constraint and acute dependency of transports on model  
 948 resolution (see also Weijer et al., 2012).

949 **5 Discussion**

950 A preliminary discussion of how the optimization acts to bring the model into con-  
 951 sistency with the available observations focuses on the question of which control vari-  
 952 ables played a dominant role in achieving a reduction in misfit (Section 5.1). A second  
 953 point of discussion highlights known issues with this first release of ASTE and sugges-  
 954 tions on how to improve future releases (Section 5.2).

955 **5.1 Identifying Key Control Adjustments**

Experiment 1		Experiment 2	
Ensemble Member	optimized control(s) <i>added</i>	Ensemble Member	optimized control(s) <i>withheld</i>
1	$[\theta_0^{R1}, S_0^{R1}]$	1	$[\theta_0^{i0}, S_0^{i0}]$
2	$[\mathcal{K}_\sigma^{R1}, \mathcal{K}_{gm}^{R1}]$	2	$[\mathcal{K}_\sigma^{i0}, \mathcal{K}_{gm}^{i0}]$
3	$\mathcal{K}_z^{R1}$	3	$\mathcal{K}_z^{i0}$
4	$[u_w^{R1}, v_w^{R1}]$	4	$[u_w^{i0}, v_w^{i0}]$
5	$T_{air}^{R1}$	5	$T_{air}^{i0}$
6	$q_{air}^{R1}$	6	$q_{air}^{i0}$
7	$[R_{sw}^{R1}, R_{lw}^{R1}]$	7	$[R_{sw}^{i0}, R_{lw}^{i0}]$
8	$P^{R1}$	8	$P^{i0}$

**Table 5.** Ensemble members for each of the two ensemble experiments. In experiment 1, the control variables listed in column #2 were *added* to unoptimized *it0* ; in experiment 2, the control variables listed in column #4 were *withheld* from optimized *ASTE-R1* .

956 Production of the *ASTE-R1* solution was achieved by gradient-based optimization,  
 957 which iteratively adjusts a set of control variables (Section 2.2). Our control space ( $\Omega$ )  
 958 comprises 3D fields of initial (i.e., 01/01/2002) temperature and salinity ( $\theta_0, S_0$ ), time-  
 959 mean spatially varying ocean mixing coefficients ( $\mathcal{K}_\sigma, \mathcal{K}_{gm}$ , and  $\mathcal{K}_z$ ), and time-varying  
 960 2D fields of near-surface atmospheric state variables ( $T_{air}, q_{air}, u_w, v_w, R_{sw}, R_{lw}$ , and  $P$ ).  
 961 We now seek to identify which of these control variable adjustments had the largest im-  
 962 pact on reducing the model-data misfit in *ASTE-R1* relative to the unoptimized *it0* .

963 To proceed, we performed two forward ensemble experiments, each experiment con-  
 964 sisting of eight members. In the first experiment, individual optimized control variables  
 965 from *ASTE-R1* were substituted into *it0* , which was then re-run. Each ensemble mem-  
 966 ber is characterized by containing one of the *ASTE-R1* optimized control variables or  
 967 variable pairs listed in Table 5 (left two columns). Note that there are 8 variables that

968 come in pairs, thus making 4 total pairs: the optimized initial conditions ( $\theta_0^{R1}, S_0^{R1}$ ), the  
 969 optimized diffusivities for the eddy mixing parameterization ( $\mathcal{K}_\sigma^{R1}, \mathcal{K}_{gm}^{R1}$ ), the two com-  
 970 ponents of the wind speed ( $u_w^{R1}, v_w^{R1}$ ), and the net downward radiation ( $R_{sw}^{R1}, R_{lw}^{R1}$ ). For  
 971 any given ensemble member, large reductions in misfit indicate that the substituted op-  
 972 timized control plays an important role in the *ASTE\_R1* solution.

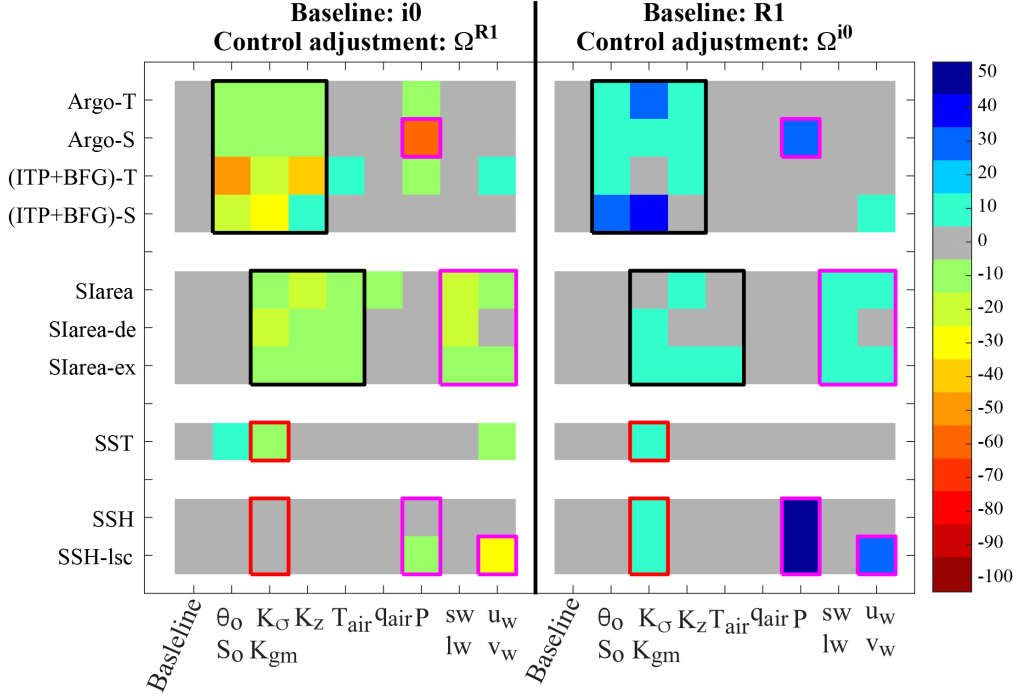


**Figure 20.** Percentage change (color) in cost with respect to the constraint listed on the ordinate, attributable to the control substitutions given on the abscissa. The left group are ensemble members of perturbation experiment 1, for which optimized controls  $\Omega^{R1}$  are substituted into the *it0* re-runs. The right group are ensemble members of experiment 2, for which non-optimized controls  $\Omega^{i0}$  are substituted into the *ASTE\_R1* re-runs. On the left half of the plot, negative values indicate an improved solution i.e., a cost reduction with respect to *it0*, implying that the optimized controls are important for reducing the misfit. On the right half, positive values indicate deterioration of the solution i.e., a cost increase with respect to *ASTE\_R1*, implying that these control adjustments are critical for obtaining the optimized *ASTE\_R1* state. Colored rectangular outlines highlight patterns of most impactful control variables (e.g., precipitation is important for the reduction of costs to Argo salinity and SSH).

973 However, a note of caution is needed. The control variables are not fully independent  
 974 (e.g., some of the atmospheric state variable controls are related via bulk formulae  
 975 or shared physics), and as a result, it is not possible to determine their full impact  
 976 in isolation. For this reason, we performed a second set of experiments, reversing the sense  
 977 of the substitutions, such that the non-optimized controls from *it0* were substituted into  
 978 *ASTE\_R1*, which was then re-run (i.e., the optimized control variables were reset to their  
 979 first guesses). In this experiment, each ensemble member is characterized by containing  
 980 one of the *it0* non-optimized control variables or variable pairs listed in Table 5 (right  
 981 two columns). This second experiment lends confidence to our assessment as follows: an  
 982 optimized control is highly likely to be an important ingredient of the *ASTE\_R1* solu-

983 tion if its incorporation notably improves the *it0* re-run (first ensemble) while its omis-  
 984 sion notably degrades the *ASTE\_R1* re-run (second ensemble).

985 In Fig. 20 we examine the impact of the control substitutions on the costs in both  
 986 ensemble experiments. We show only normalized costs with respect to the following ag-  
 987 gregated data sets: Argo, ITP, Beaufort Gyre moorings, and satellite-based observations  
 988 of SST, SSH and sea ice concentration. This choice enables a more focused discussion  
 989 whilst also informing the large-scale quality of the solution near the ocean surface in the  
 990 Atlantic Ocean (where the majority of SSH and SST data were acquired) and through-  
 991 out the upper ocean in the North Atlantic, GIN Seas, and Labrador Sea interior (from  
 992 Argo *T* and *S* data) and in the western Arctic (from ITP and Beaufort Gyre moorings).  
 993 Lastly, costs for sea ice concentration indicate performance of modelled air-sea fluxes and  
 994 mixed layer properties in marginal ice zones (see Fig. 7 and related discussion).

995 Our analysis, based on Fig. 20, reveals the importance of precipitation (*P*) adjust-  
 996 ments in obtaining realistic subsurface salinity distributions in the North Atlantic through  
 997 the removal of the systematic excess rain bias discussed in Section 3.3 (Fig. 13d). Specif-  
 998 ically, inclusion of the optimized precipitation  $P^{R1}$  in the *it0* re-run (column under “P”  
 999 on the left half of Fig. 20) reduced the cost with respect to Argo salinity by 56% (orange  
 1000 square at row “Argo-S” and column “P” corresponding to large negative, i.e., cost re-  
 1001 duction, values between  $-50$  and  $-60$  as indicated in the color scale). A 31% increase  
 1002 in this cost was seen on omission of the optimized precipitation in the *ASTE\_R1* re-run  
 1003 (blue square at row “Argo-S” and column “P” on the right half of Fig. 20, correspond-  
 1004 ing to positive, i.e., cost increase, values between  $+30$  to  $+40$  in color scale). Large im-  
 1005 provements in SSH can also be attributed in part to corrected precipitation, as well as  
 1006 surface winds. Amongst other atmospheric forcing variables, surface air temperature, down-  
 1007 ward radiative forcing, and winds all have important impact on the sea ice cover (col-  
 1008 lective average of 17% improvement to *it0* and 5% degradation to *ASTE\_R1* ).

1009 Adjustments to the initial conditions, vertical diffusivity and eddy mixing are also  
 1010 found to be important for improving subsurface hydrography throughout the *ASTE\_R1*  
 1011 domain. Optimized eddy mixing-related controls ( $\mathcal{K}_\sigma^{R1}, \mathcal{K}_{gm}^{R1}$ ) alone result in a 14% im-  
 1012 provement (and 14% degradation) of the Arctic hydrography misfit when included (omit-  
 1013 ted) from the *it0* (*ASTE\_R1*) re-runs, respectively. These adjustments to the eddy mix-  
 1014 ing parameters also improve SST and SSH, and – in addition to the adjustments made  
 1015 to the vertical diffusivity and atmospheric conditions – are also seen to be critical for im-  
 1016 proved representation of sea ice cover.

## 1017 5.2 Known Issues and Future Directions

1018 During production of *ASTE\_R1* we have striven to utilize all constraints known to  
 1019 us and that the state estimation machinery could handle. This comprises  $O(10^9)$  obser-  
 1020 vations from diverse data sources (Table 2). Despite this effort, some systematic biases  
 1021 remain in the *ASTE\_R1* solution. As the optimization is ongoing and *ASTE* is still con-  
 1022 verging, we anticipate the costs listed in Table 3 will continue to reduce and some of the  
 1023 remaining biases will be removed. In certain cases, due to model structural errors or non-  
 1024 resolved physics, full convergence might not be attainable (Wunsch & Heimbach, 2007).  
 1025 Here we discuss notable issues remaining in the *ASTE\_R1* solution and possible future  
 1026 directions for developing the next *ASTE* release with improved model physics.

1027 *Eastern Arctic hydrography:* One of the largest remaining systematic biases is found  
 1028 in the Eurasian Basin, where subsurface constraints comprise sparse ITP sampling of the  
 1029 basin interior alone. Although the inflow is constrained by moorings at Fram Strait, down-  
 1030 stream observation of the circulation, eddy-induced stirring and vertical mixing in the  
 1031 Eurasian Basin along the shelf-basin slope and interior are limited (Fig. 21a). The se-  
 1032 rious implications of this paucity of data are highlighted by considering that the AW in-  
 1033 flow takes  $\sim 6$ -10 years to transit this region, during which there are no local observa-

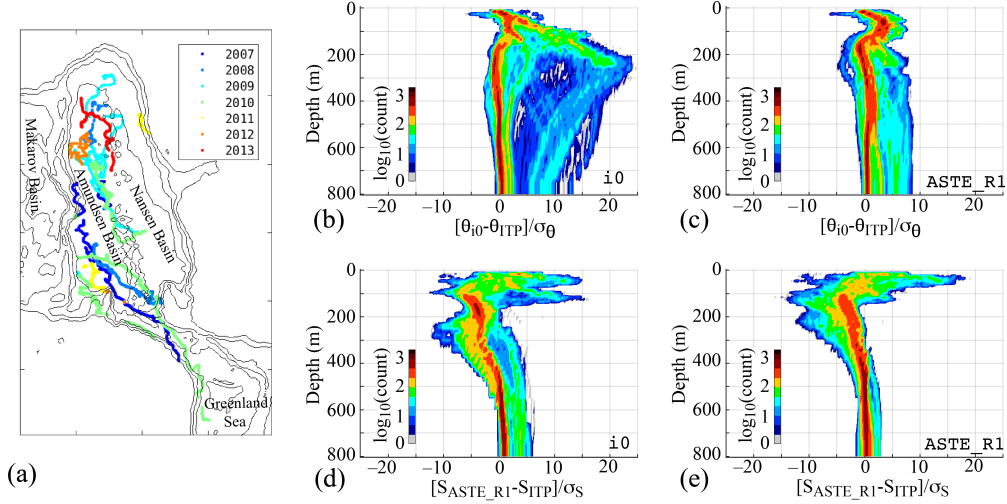


**Figure 21.** (a) Spatial distribution of ITP data used to constrain *ASTE\_R1* in the Eurasian Basin; colors distinguish acquisition year. Histograms of normalized misfit to ITP (b,c) temperature and (d,e) salinity as a function of depth in the Eurasian Basin for (b,d) *it0* and (c,e) *ASTE\_R1*.

1034 tional constraints. As a result, the inverse problem is highly under-determined. In prac-  
 1035 tice, under-determination allows non-unique pathways to misfit minimization. For *ASTE\_R1*  
 1036 , we find that the AW layer in the Eastern Arctic spreads to occupy a greater depth range  
 1037 towards the end of the estimation period. This problem was also present in *it0* and has  
 1038 been partly ameliorated during the optimization, as reflected in the removal of the largest  
 1039 positive temperature misfits with respect to ITP data (Fig. 21b-c). This thickening of  
 1040 the AW layer is also a common problem in many state-of-the-art Arctic Ocean models  
 1041 (Holloway et al., 2007; Ilicak et al., 2016; Docquier et al., 2019; Uotila et al., 2019).

1042 As it is unlikely that widespread observation of 3-D velocity and mixing will be made  
 1043 in the foreseeable future, we anticipate that AW watermass representation in the Eurasian  
 1044 basin will remain an issue for both the next generation of state-of-the-art Arctic Ocean  
 1045 models and the next ASTE release. Although we do not expect large gains from planned  
 1046 changes to the ocean observing system in the near future, we do anticipate improvements  
 1047 in sea ice state, mixed layer representation, and shelf-basin exchanges in the next ASTE  
 1048 release, due to recent improvements to the stability of the adjoint of the sea ice thermo-  
 1049 dynamics (Bigdeli et al., 2020). This will enable a more complete use of sea ice obser-  
 1050 vations as active contributions to the cost function reduction  $J$  (eqn. 1). The sensitiv-  
 1051 ity of the associated model-data misfits to the control space can then be used to better  
 1052 adjust atmospheric forcings. This will allow us to fully leverage the constraint from satellite-  
 1053 based observations of the sea-ice state, which could only be partly exploited in the pseudo  
 1054 sea ice adjoint employed for construction of *ASTE\_R1*. Inclusion of the sea ice thermo-  
 1055 dynamics adjoint could potentially improve AW upward ventilation (Ivanov et al., 2012;  
 1056 Polyakov et al., 2020) and preserve a more stable AW layer thickness, both in the Eurasian  
 1057 Basin and further downstream in the Western Arctic.

1058 *Arctic Circumpolar Current:* In the Laptev Sea it is thought that the circumpolar  
 1059 circulation of AW splits at  $\sim 145^\circ\text{E}$ , with a fraction returning to Fram Strait along  
 1060 the Lomonosov Ridge (Rudels, 2015) and the remainder continuing along the basin’s rim  
 1061 into the Western Arctic, although the exact partitioning is not well constrained. In the  
 1062 Western Arctic it is typically assumed that the AW continues to circulate cyclonically  
 1063 along the basin boundary, although both *ASTE\_R1* (Grabon, 2020) and a modeling ef-

1064 fort informed by observed radionuclide distributions (Karcher et al., 2012) suggest a weak  
 1065 anticyclonic circulation during the last decade. Recent work analyzing all available cur-  
 1066 rent meters (updated from Baumann et al. (2018)) has yielded velocity probability dis-  
 1067 tributions for the Arctic region. This will be investigated as a novel approach to con-  
 1068 strain ocean velocities within the AW circulation in the next *ASTE\_R1* release. In addition,  
 1069 a more detailed examination of the momentum and vorticity budgets along the circum-  
 1070 polar current will offer insights into the role of viscous dissipation and eddies in main-  
 1071 taining the cyclonic sense of circulation (Yang, 2005; Spall, 2020).

1072 *Arctic river runoff and Greenland discharge:* FW transports and content in the  
 1073 late 2010s are low in *ASTE\_R1* relative to independent observations (Section 4.3 and 4.4.2).  
 1074 Near the surface in the Arctic and along the Greenland coast, recent increases in river  
 1075 (Shiklomanov et al., 2020) and tundra runoff (Bamber et al., 2012), surface solid and sub-  
 1076 surface glacial discharge (Bamber et al., 2012, 2018) have been observed. This increase  
 1077 was not included in the *ASTE\_R1* forcing. Meaningful application of these FW fluxes  
 1078 as model forcings, especially in the Arctic marginal seas, requires careful consideration  
 1079 of the following factors. Sub-glacial discharge is observed to enter the outlet glacier fjord  
 1080 at depths near the grounding line instead of at the surface of the fjord’s exit to the con-  
 1081 tinental shelf (Straneo & Cenedese, 2015; Sciascia et al., 2013). Mixing and entrainment  
 1082 of this FW with the surroundings creates modified water whose property is prohibitively  
 1083 difficult to continuously track downstream from the source using observed  $T/S$  (Beaird  
 1084 et al., 2018). Consequently, the pathways of FW redistribution are highly uncertain. Nu-  
 1085 merical simulations with Greenland discharge distributed at the surface yield pathways  
 1086 from the source into the interior of SPNA and GIN seas that vary substantially with model  
 1087 resolution and representation of mean currents (Weijer et al., 2012; Dukhovskoy et al.,  
 1088 2016). The depth to which this FW is mixed down also varies highly with resolution (Dukhovskoy  
 1089 et al., 2016), causing near surface over-freshening in certain cases and a 30–50% decrease  
 1090 in the North Atlantic Meridional Overturning Circulation (AMOC) at time-scales vary-  
 1091 ing between 3–50 years (Weijer et al., 2012). Similarly, preliminary sensitivity experi-  
 1092 ments in *ASTE\_R1* with observed Greenland discharge applied at the surface show over-  
 1093 freshening of the upper ocean in the Greenland Sea and a decrease in the AMOC at 55°N  
 1094 by 40% within 5 years, inconsistent with observations (not shown). Prior to the next *ASTE*  
 1095 release, a dedicated study will be required to implement updated estimates of Greenland  
 1096 discharge as a subsurface freshwater forcing, consistent with observations (Straneo & Cenedese,  
 1097 2015). This will entail incorporation of a melt water plume parameterization into the  
 1098 *ASTE* framework. Lastly, instead of being absorbed into net surface freshwater flux  $E-P-R$ ,  
 1099 a new control variable for runoff could be introduced to isolate and fully inter-  
 1100 rogate sensitivity to subsurface forcing from subglacial discharge.

1101 *Subpolar North Atlantic hydrography:* A warm bias in *ASTE\_R1* at 500–2000 m  
 1102 depth persists both in the Irminger Sea (Fig. 14c) and throughout the eastern SPNA (not  
 1103 shown), and is associated with a weaker poleward transport of Atlantic warm water across  
 1104 the GSR (Fig. 15). Poor representation of AW inflow across the GSR is a common prob-  
 1105 lem in coarse to medium resolution ocean models (Heuzé & Årthun, 2019). Specifically,  
 1106 these models produce lower volume and heat transports across the GSR compared to ob-  
 1107 servations (Heuzé & Årthun, 2019). Since the resolution of *ASTE\_R1* is  $\sim 18$  km in the  
 1108 subpolar gyre, we anticipate incomplete representation of both eddy/diffusive mecha-  
 1109 nisms – estimated to be important across the shallow Denmark Strait and Iceland-Faroe  
 1110 Ridge (Buckley et al., 2015) – and watermass transformations in the *ASTE\_R1* solution.  
 1111 Thus, although *ASTE\_R1* can capture the mean transports of volume and heat between  
 1112 Iceland and Scotland (Fig. 15–17), the remaining warm bias across Denmark Strait and  
 1113 south of the GSR likely impacts our estimate of heat content in both the eastern SPNA  
 1114 and Nordic Seas and alters the optimized air-sea heat flux in both regions. Recent data  
 1115 from the Overturning in the Subpolar North Atlantic Program (OSNAP) observing sys-  
 1116 tem (Lozier et al., 2017, 2019) mooring array (deployed in 2014) will provide important

1117 information in the subpolar region, and an especially valuable constraint on the bound-  
 1118 ary currents and overflow waters, not captured by Argo.

## 1119 6 Summary and Outlook

1120 We have presented the first release of the Arctic Subpolar gyre sTate Estimate, *ASTE\_R1*  
 1121 , a data-constrained and dynamically consistent ocean-sea ice synthesis spanning the pe-  
 1122 riod 2002–2017. *ASTE\_R1* is produced using the ECCO adjoint-based state estimation  
 1123 framework, in which an ocean general circulation model, the MITgcm serves as a dynam-  
 1124 ical interpolator, spreading the influence of  $O(10^9)$  incorporated observations through  
 1125 space and time by way of linearized adjustment processes encapsulated in an adjoint model.  
 1126 Importantly, the model-data misfit is reduced via iterative adjustments to the initial hy-  
 1127 drographic conditions, atmospheric forcing and model mixing parameters alone, ensur-  
 1128 ing adherence to the governing equations throughout the entire estimation period. This  
 1129 distinguishes our approach from ocean reanalysis, in which violation of conservation laws  
 1130 complicates application for climate research (Stammer et al., 2016). The ability to as-  
 1131 sess closed tracer and momentum budgets in *ASTE\_R1* is a key strength of the prod-  
 1132 uct. As all sources and sinks are accounted for, full heat, salt and momentum (or vor-  
 1133 ticity) budgets can be analyzed to identify dominant sources contributing to the observed  
 1134 changes. These closed budget analyses can also be performed in  $T, S, \sigma$  space follow-  
 1135 ing R. P. Abernathey et al. (2016), enabling diagnosis of watermass evolution and de-  
 1136 struction in the *ASTE\_R1* solution. In addition, the adjoint modeling infrastructure al-  
 1137 lows for linear sensitivity studies using *ASTE\_R1* for investigation of causal mechanisms  
 1138 underlying variability in key quantities of climate interest (e.g., Bigdeli et al., 2020; Nguyen  
 1139 et al., 2020b; Pillar et al., 2016).

1140 During production of *ASTE\_R1* we have strived to utilize all observational constraints  
 1141 known to us and that the state estimation machinery can handle. *ASTE\_R1* thus arguably  
 1142 represents the biggest effort undertaken to date with the aim of producing a specialized  
 1143 Arctic ocean-ice estimate, freely available to the research community. This complements  
 1144 existing global ECCO solutions (Forget et al., 2015a; Fukumori et al., 2018a), the South-  
 1145 ern Ocean State Estimation (SOSE, (Mazloff et al., 2010)) and other global and regional  
 1146 ECCO derivatives (e.g., Köhl & Stammer, 2008; Gopalakrishnan et al., 2013; Zaba et  
 1147 al., 2018; Köhl, 2020).

1148 For this initial assessment of *ASTE\_R1* , we have focused on comparison to avail-  
 1149 able observational constraints. Many of these were actively employed in the optimiza-  
 1150 tion procedure, but some (e.g., all volume and tracer transport estimates) were withheld,  
 1151 allowing independent verification. The optimized solution serves as a significant improve-  
 1152 ment from the unconstrained state, achieving consistency with the majority of incorpo-  
 1153 rated observations, including both the set used in the optimization and that retained for  
 1154 post-validation (Table 3).

1155 The most substantial misfit reduction in *ASTE\_R1* are sea ice cover in the marginal  
 1156 ice zone, western Arctic hydrography, and subtropical North Atlantic sea level anomaly  
 1157 and subsurface salinity (Table 3, Fig. 6). In the Arctic Mediterranean, using only a proxy  
 1158 sea ice adjoint, *ASTE\_R1* achieves a 83% reduction in misfit to satellite-derived sea ice  
 1159 concentration constraints, mainly via improved representation of the sea-ice edge (Fig. 7).  
 1160 The solution faithfully reproduces both the observed seasonal cycle and low frequency  
 1161 trend of sea-ice extent.

1162 At Fram Strait, the mooring array is crucial to constraining the important AW in-  
 1163 flow and local hydrographic properties. At this important Arctic gateway, *ASTE\_R1* ex-  
 1164 hibits a 58% misfit reduction through the water column across the strait relative to the  
 1165 unconstrained simulation. In the Arctic interior, ITPs provide unique information on the  
 1166 subsurface hydrography. Because 71% of the ITP profiles are located within the upper

1167 5–800 m in the Canada Basin interior, the most significant misfit reduction was seen here  
1168 (85% in  $T$  and 62% in  $S$ , Fig. 10). In the remaining Arctic basin, low data coverage, com-  
1169 bined with large uncertainty in the mean circulation and mixing parameters, resulted  
1170 in less notable improvement (reductions of 89% in  $T$  and 31% in  $S$ ), but biases persist,  
1171 especially at depth below the AW core (Fig. 21).

1172 Accompanying improved fit to hydrographic data used to constrain the solution,  
1173 we find improvements in basin-scale heat and freshwater content. Interannual variabil-  
1174 ity and low frequency trends in both heat and FW content are well represented in the  
1175 Arctic Mediterranean and SPNA of *ASTE\_R1*. In the Beaufort Sea, *ASTE\_R1* captures  
1176 the observed steady increase in upper halocline heat content from 2004–2017. Both the  
1177 observed heat content increase in the upper water column within the Barents Sea and  
1178 the heat content decrease in the east SPNA are also consistently captured (Fig. 18).

1179 We have been careful to clearly outline the notable biases remaining in the *ASTE\_R1*  
1180 solution. These include a warm bias below the AW core in the eastern Arctic and in the  
1181 east SPNA. The cause is a combination of lack of constraint here for the hydrography,  
1182 mean circulation, and the adjustable initial condition and parametric controls. Additional  
1183 biases exists in FW transports and contents in the Arctic Mediterranean due to the omis-  
1184 sion of increased runoff from Arctic rivers and Greenland freshwater discharge.

1185 An advantage of our approach is that the use of a dynamical interpolator can im-  
1186 prove spectral representation of the estimated state compared to gridded products pro-  
1187 duced using statistical interpolations (e.g., Verdy et al., 2017). This has not been ad-  
1188 dressed here, but it is a useful avenue for future ASTE assessments and ongoing devel-  
1189 opment.

1190 Looking toward the next *ASTE\_R1* release, we expect the greatest progress will  
1191 be made by incorporating new model physics. In particular, improving the stability of  
1192 the sea ice thermodynamic adjoint (Bigdeli et al., 2020) will enable its use in ASTE, pro-  
1193 viding stronger constraint of air-ice-sea exchanges and ocean ventilation. Future efforts  
1194 will target hydrographic improvements along the Arctic shelf-basin slope in the eastern  
1195 Arctic to reduce the *ASTE\_R1* AW layer warm bias. Additionally, updated estimates  
1196 of runoff and calving fluxes and inclusion of a parameterization of sub-glacial discharge  
1197 will enable improved estimate of freshwater redistribution and interbasin exchange. New  
1198 constraints, including datasets from the OSNAP mooring array (Lozier et al., 2017, 2019),  
1199 sea surface salinity (Vinogradova & Ponte, 2012; Fournier et al., 2019), and sea ice thick-  
1200 ness (Tian-Kunze et al., 2014; Ricker et al., 2017) will also be fully utilized in the pro-  
1201 duction of a further improved next ASTE release.

## 1202 **Appendix A *ASTE\_R1* Product Distribution**

### 1203 **A1 Configuration set up**

1204 The model configuration and all necessary inputs, including the optimized control  
 1205 adjustments, required for *ASTE\_R1* re-runs are available to the public, as discussed in  
 1206 the next section. The code base employed for *ASTE\_R1* production was MITgcm check-  
 1207 point c65q. *ASTE\_R1* was built using the full state estimation infrastructure, includ-  
 1208 ing specialized packages for misfit and adjustment evaluation, developed for ECCOv4r1  
 1209 (Forget et al., 2015a). In addition, two code developments specific to *ASTE* include the  
 1210 implementation of a vertical diffusivity power control ( $\log_{10}\mathcal{K}_z$ ) and the capability to switch  
 1211 between daily and monthly SSH costs.

1212 To ensure numerical stability during *ASTE\_R1* production, the following model choices  
 1213 were important: (a) a staggered time-step for momentum advection and Coriolis terms;  
 1214 (b) third-order advection for tracers (scheme code 30 in Table 2.2 in Adcroft et al., 2018),  
 1215 (c) linear free surface approximation, and (d) application of freshwater forcing via a vir-  
 1216 tual salt flux (i.e., no accompanying change in mass). These choices permitted a time-  
 1217 step of 1200 s. After 62 iterations, better model choices were used for the final forward  
 1218 run that produces more accurate physics in the distributed version of *ASTE\_R1*. These  
 1219 include (i) seventh order advection for tracers (scheme code 7 in Table 2.2 in Adcroft et  
 1220 al., 2018); (ii) nonlinear free surface with scaled  $z^*$  coordinates (Adcroft & Campin, 2004),  
 1221 and (iii) application of freshwater forcing via a real freshwater flux (i.e., with accompa-  
 1222 nying change in mass, Campin et al., 2004). These choices required a shorter time-step  
 1223 of 600 s. The *ASTE\_R1* solution described and assessed in this paper is from the re-run  
 1224 of iteration 62 with the model choices (i)–(iii) described above.

1225 In the distributed code, at compile and run-time, the user has the choice to use the  
 1226 more stable set up with a time-step of 1200 s or employ the more accurate numerics and  
 1227 physics with a time-step of 600 s as described above. We found that these small changes  
 1228 in the model configuration for the final forward run did not have a significant impact on  
 1229 the solution. This result is consistent with published studies suggesting small differences  
 1230 in ocean dynamics between LFS vs NLFS in combination with virtual salt or real fresh-  
 1231 water flux (Roulet & Madec, 2000; Campin et al., 2004; Yin et al., 2010). The advan-  
 1232 tage of their application here is in enabling more accurate physical interpretation of mass  
 1233 and freshwater budgets. However, since these options also require a shorter timestep (for  
 1234 the nonlinear free surface) and a larger stencil (for the higher order advection), their use  
 1235 demands significantly more computational resources (twice the wallclock time). For this  
 1236 reason, it was not feasible to employ these options until the final stages of *ASTE\_R1* de-  
 1237 velopment.

### 1238 **A2 Distribution of the *ASTE\_R1* solution**

1239 The full *ASTE\_R1* solution is publicly available through the NSF Arctic Data Cen-  
 1240 ter as follows:

- 1241 a. Time varying fields as monthly averages and monthly snapshots (Nguyen et al., 2021a);
- 1242 b. Depth-integrated time varying fields as monthly averages and monthly snapshots  
 1243 (Nguyen et al., 2021b);
- 1244 c. Selected time varying state variables as daily averages (Nguyen et al., 2021c);
- 1245 d. 12-month climatological averages (Nguyen et al., 2021d);
- 1246 e. In situ profiles and model-equivalent (Nguyen et al., 2021e);
- 1247 f. *ASTE\_R1* Grid files, Documentations (user guide, domain layout) and MATLAB  
 1248 toolbox to help analyze the output fields (Nguyen et al., 2021f);
- 1249 g. Compile time and run time inputs necessary to reproduce *ASTE\_R1* with the MIT-  
 1250 gcm (Nguyen et al., 2021g).

1251 All model output fields are available here as NetCDF files. In addition to being archived  
 1252 at the Arctic Data Center, *ASTE\_R1* NetCDF data are also mirrored at the UT-Austin  
 1253 ECCO portal at: <https://web.corral.tacc.utexas.edu/OceanProjects/ASTE/>, which  
 1254 is provided by the Texas Advanced Computing Center (TACC). Alternative to NetCDF  
 1255 format, the monthly mean fields are additionally hosted in a compressed format on Ama-  
 1256 zon Web Services (AWS) servers, provided by TACC at [http://aste-release1.s3-website](http://aste-release1.s3-website.us-east-2.amazonaws.com/)  
 1257 [.us-east-2.amazonaws.com/](http://aste-release1.s3-website.us-east-2.amazonaws.com/). These files are meant to be accessed with the `llcreader`  
 1258 module of the open source python package `xmitgcm` (R. Abernathey et al., 2020), which  
 1259 allows users to analyze the data without the need to actually download it. An interac-  
 1260 tive demonstration of this capability, which shows some sample calculations enabled by  
 1261 `xgcm` (R. P. Abernathey et al., 2020) and `ECCOV4-py` ([github.com/ECCO-GROUP/ECCOV4](https://github.com/ECCO-GROUP/ECCOV4-py)  
 1262 `-py`), is available through the Binder Project (Project Jupyter et al., 2018) at [github](https://github.com/crios-ut/aste)  
 1263 [.com/crios-ut/aste](https://github.com/crios-ut/aste) (T. Smith, 2021). This repository additionally contains environ-  
 1264 ment files so that any user can reproduce the computing environment necessary to an-  
 1265 alyze *ASTE\_R1*, for instance on their own laptop.

### 1266 **A3 Observational constraints from ECCOV4r3 standard suite**

1267 As described in Section 2.1, the observational constraints used in *ASTE* include  
 1268 the standard ECCOV4r3 suite (Fukumori et al., 2018b) and additional high-latitude data  
 1269 as listed in Table 2. For a quick reference, we list the data from the ECCOV4r3 suite  
 1270 in Table A1 and refer the readers to Fukumori et al. (2018b) for further details on the  
 data description and preparation.

Variable	Observations
Sea level	TOPEX/Poseidon (1993-2005), Jason-1 (2002-2008), Jason-2 (2008-2015), Geosat-Follow-On (2001-2007), CryoSat-2 (2011-2015), ERS-1/2 (1992-2001), ENVISAT (2002-2012), SARAL/AltiKa (2013-2015)
Temperature profiles	Argo floats (1995-2015), XBTs (1992-2008), CTDs (1992-2011), Southern Elephant seals as Oceanographic Samplers (SEaOS; 2004-2010), Ice-Tethered Profilers (ITP, 2004-2011)
Salinity profiles	Argo floats (1997-2015), CTDs (1992-2011), SEaOS (2004-2010)
Sea surface temperature	AVHRR (1992-2013)
Ocean bottom pressure	GRACE (2002-2014), including global mean ocean mass
TS climatology	World Ocean Atlas 2009
Mean dynamic topography	DTU13 (1992-2012)

**Table A1.** The standard ECCOV4r3 data suite used to constrain *ASTE\_R1*. The entries in this table are duplicates from Table 1 in Fukumori et al. (2018b).

1271

## 1272 **Appendix B Transport Calculation with Referenced $\theta/S$**

1273 Here we describe heat and freshwater transport calculations used in *ASTE\_R1* with  
 1274 respect to reference values of potential temperature ( $\theta_r$ ) and salinity ( $S_r$ ), respectively.  
 1275 This serves to (1) provide calculation details for comparison to those used by previously  
 1276 published estimates (supplementing results presented in section 4), and (2) expose where  
 1277 calculation differences may prevent meaningful comparisons (following discussion in sec-

1278 tion 2.3). For budget calculations, we refer the readers to detailed descriptions provided  
 1279 in Piecuch (2017) and Forget et al. (2015a).

1280 In the literature, transports are often computed with nonzero referenced values  $\theta_r/S_r$ .  
 1281 In section 4 we provided online transport estimates for *ASTER1* made using non-zero  
 1282 references (e.g., for the heat flux through the Bering Strait). We emphasize that all of-  
 1283 fline transport calculations made using available diagnostics from *ASTER1* (and all stan-  
 1284 dard configurations of the MITgcm) will be exact only with  $\theta_r = 0$  and  $S_r = 0$ , as these  
 1285 are the values used in all online tracer equations. To support users seeking to compute  
 1286 *ASTER1* transports offline assuming nonzero references, we now examine the loss of ac-  
 1287 curacy that will be incurred. This loss of accuracy depends on the amplitude of various  
 1288 missing terms (e.g., bolus transports and diffusive fluxes) relative to the contributions  
 1289 (e.g., Eulerian advection) contained in the available diagnostics. By deriving these ap-  
 1290 proximations here and comparing their magnitudes with the accurate online values across  
 1291 important Arctic and GIN Seas gateways, we aim to identify which transports reported  
 1292 in Fig. 16-17 are reliable and which ones require caution for interpretation.

### 1293 B1 Accurate transport calculations

The horizontal transports of volume, heat, and freshwater (FW) across the Arc-  
 tic Mediteranean gateways are calculated by summing the total horizontal convergence  
 in the mass, heat, and salinity budgets, respectively, (Piecuch, 2017) as follows,

$$F_V = \int_L \int_{-D}^{\eta} \mathbf{u}_E \cdot \hat{\mathbf{n}} \, dz \, dl \quad (\text{B1.0})$$

$$\begin{aligned} F_H &= \rho_0 C_p \int_L \int_{-D}^{\eta} (\theta - \theta_r)(\mathbf{u}_E + \mathbf{u}_b) \cdot \hat{\mathbf{n}} \, dz \, dl + \rho_0 C_p F_{\theta,dif} + F_{H_i,adv} + F_{H_{sn},adv} \\ &= F_{H_{\theta},adv} + F_{H_{\theta},dif} + F_{H_i,adv} + F_{H_{sn},adv} \end{aligned} \quad (\text{B2.0})$$

$$\begin{aligned} F_{FW} &\approx \int_L \int_{-z_{S_r}}^{\eta} \frac{(S_r - S)}{S_r} (\mathbf{u}_E + \mathbf{u}_b) \cdot \hat{\mathbf{n}} \, dz \, dl + \left(1 + \frac{\eta}{D}\right) \frac{F_{S,dif}}{S_r} + \int_L \left( \frac{S_r - S_i}{S_r} \frac{\rho_i}{\rho_0} h_i \mathbf{u}_i + \frac{\rho_{sn}}{\rho_0} h_{sn} \mathbf{u}_{sn} \right) \cdot \hat{\mathbf{n}} \, dl \\ &= F_{FW_S,adv} + F_{FW_S,dif} + F_{FW_i,adv} + F_{FW_{sn},adv} \end{aligned} \quad (\text{B3.0})$$

1294 where  $t$  is the time,  $\mathbf{u}_E, \mathbf{u}_b$  the (partial-cell-weighted) ocean resolved Eulerian and un-  
 1295 resolved bolus velocities, and  $\mathbf{u}_i, \mathbf{u}_{sn}$  the sea ice and snow Eulerian velocities. For each  
 1296 gateway across which the transports are computed,  $\hat{\mathbf{n}}$  is the normal direction at each model  
 1297 grid point along the transport gate and  $L$  the section length along the gate. Vertical in-  
 1298 tegration is between  $\eta$  the sea surface and  $-D$  the ocean floor depth for volume and heat  
 1299 transports. Constants  $\rho_0 = 1029, \rho_i = 910$  and  $\rho_{sn} = 330$  are the seawater, sea ice,  
 1300 and snow densities in  $\text{kg/m}^3$ .  $C_p = 3996 \text{ J}^\circ\text{C}^{-1}\text{kg}^{-1}$  is the specific heat capacity of sea  
 1301 water,  $\theta_r$  the reference temperature,  $S_r = 34.8$  ppt the reference salinity, and  $S_i = 4$  ppt  
 1302 the constant sea ice salinity used in ASTE.  $\theta$  and  $S$  are the ocean potential temperature  
 1303 and salinity in  $^\circ\text{C}$  and ppt, respectively;  $h_i$  and  $h_{sn}$  are the thickness of sea ice and snow  
 1304 in m.  $F_{\theta,dif}$  and  $F_{S,dif}$  are the parameterized diffusive flux of potential temperature and  
 1305 salinity  $\theta_r = 0$  and  $S_r = 0$ . For both advective and diffusive contributions to fresh-  
 1306 water transports (eqn. B3.0), vertical integration is only down to the depth of the refer-  
 1307 ence isohaline  $-z_{S_r}$ .

1308 Exact closure of heat budgets (see equations in Forget et al. (2015a) and Piecuch  
 1309 (2017)) and exact (to within numerical precision) calculation of heat transports (eqn. B2.0)  
 1310 can be achieved when  $\theta_r = 0$  and all diagnostics terms are computed online. Near ex-  
 1311 act freshwater budgets (see equations in Forget et al. (2015a) and Tesdal and Haine (2020))  
 1312 and transports (eqn. B3.0) can be achieved with  $S_r = 0$ . Additionally the vertical in-  
 1313 tegral must be computed every time step, continuously updating the time-evolving  $z_{S_r}$ .

1314

## B2 Approximations for nonzero $\theta_r/S_r$

1315

1316

1317

1318

1319

1320

1321

1322

When using nonzero reference values (e.g.,  $\theta_r = -0.1^\circ\text{C}$  or  $S_r = 34.8$  ppt as in Østerhus et al., 2019), neither heat nor freshwater diffusion terms are available in the offline diagnostics. To gauge orders of magnitudes, however, we approximate the diffusion term for FW using  $F_{S,dif}$  scaled by the non-linear free-surface factor  $(1 + \frac{\eta}{D})$  following Piecuch (2017), then further scale by  $\frac{1}{S_r}$ . For the advection terms, the long-term mean transport can be derived exactly for heat and approximated for FW using a combination of readily available offline diagnostics for volume and heat/salt budgets as follows:

$$\begin{aligned} \langle F_{H_\theta,adv} \rangle &= \rho_0 C_p \left\langle \int_{-D}^{\eta} \int_L \left( (\theta - \theta_r) (\mathbf{u}_E + \mathbf{u}_b) \right) \cdot \hat{\mathbf{n}} \, dz \, dl \right\rangle \\ &= \rho_0 C_p \left\langle \int_{-D}^{\eta} \int_L \theta (\mathbf{u}_E + \mathbf{u}_b) \cdot \hat{\mathbf{n}} \, dz \, dl \right\rangle - \rho_0 C_p \theta_r \left\langle \int_{-D}^{\eta} \int_L \mathbf{u}_E \cdot \hat{\mathbf{n}} \, dz \, dl \right\rangle \end{aligned} \quad (\text{B2.1})$$

$$\begin{aligned} \langle F_{FW_S,adv} \rangle &\approx \left\langle \int_{-z_{S_r}}^{\eta} \int_L \frac{(S_r - S)}{S_r} (\mathbf{u}_E + \mathbf{u}_b) \cdot \hat{\mathbf{n}} \, dz \, dl \right\rangle \\ &\approx \left\langle \int_{-z_{S_r}}^{\eta} \int_L \left( \frac{S_r}{S_r} (\mathbf{u}_E + \mathbf{u}_b) - \frac{S}{S_r} (\mathbf{u}_E + \mathbf{u}_b) \right) \cdot \hat{\mathbf{n}} \, dz \, dl \right\rangle \\ &\approx \left\langle \int_{-z_{S_r}}^{\eta} \int_L \mathbf{u}_E \cdot \hat{\mathbf{n}} \, dz \, dl \right\rangle - \frac{1}{S_r} \left\langle \int_{-z_{S_r}}^{\eta} \int_L S (\mathbf{u}_E + \mathbf{u}_b) \cdot \hat{\mathbf{n}} \, dz \, dl \right\rangle \end{aligned} \quad (\text{B3.1})$$

1323

1324

1325

where the  $\langle \cdot \rangle$  is the multi-year mean which ensures  $\langle \mathbf{u}_b \rangle \equiv 0$  by definition. The approximation in  $F_{FW_S,adv}$  is due, again, to the reliance in the offline average of  $\langle S \rangle$  in determining  $-z_{S_r}$ .

1326

## B3 Approximations using monthly mean $\theta$ , $S$ and $\mathbf{u}_E$ ,

1327

1328

1329

1330

1331

1332

1333

Lastly, we note that due to disk space and I/O restrictions, it is typical for modeling studies to save and subsequently provide only monthly-averaged Eulerian velocity  $\langle \mathbf{u}_E \rangle$  and tracers  $\langle \theta \rangle$  and  $\langle S \rangle$  for offline calculations of heat/FW transports and contents (e.g., Jahn et al., 2012; Kinney et al., 2014; Q. Wang et al., 2016b, 2016a; Ilicak et al., 2016; Heuzé & Årthun, 2019). In this case, the calculation for the advective terms in heat and FW transports are further approximated due to the cross-terms involving the bolus velocity  $S\mathbf{u}_b$  and  $\theta\mathbf{u}_b$  being excluded:

$$F_{H_\theta,adv} \approx \rho_0 C_p \int_{-D}^{\eta} \int_L (\theta - \theta_r) \mathbf{u}_E \cdot \hat{\mathbf{n}} \, dz \, dl \quad (\text{B2.2})$$

$$F_{FW_S,adv} \approx \int_{-z_{S_r}}^{\eta} \int_L \frac{(S_r - S)}{S_r} \mathbf{u}_E \cdot \hat{\mathbf{n}} \, dz \, dl \quad (\text{B3.2})$$

1334

1335

1336

1337

As before, inaccuracies will be incurred when  $z_{S_r}$  is determined using the monthly mean  $\langle S \rangle$ . This is the case for all results shown for FW because no diagnostics pertinent to FW, including those of  $S - S_r$  or  $z_{S_r}$ , are available standard MITgcm diagnostic outputs.

1338

## B4 Interpretation of Transports: Confidence and Caution

1339

1340

Fig. B1-B2 show time-series of heat and FW transports for key gateways using both the most accurate online method and approximated offline method described above. The

1341 diffusion terms for both heat and FW are at least two orders of magnitude smaller than  
 1342 the advection terms and can be ignored almost everywhere. The exception is at the Den-  
 1343 mark Strait and Iceland-Faroe channels where omission of the diffusive contribution to  
 1344 the total heat transport leads to large errors of 30% and 100%, respectively. This shows  
 1345 that the estimates of tracer transports across these two gates should be interpreted with  
 1346 caution when computed offline using only model monthly outputs of the Eulerian veloc-  
 1347 ity and tracer averages.

1348 For FW, as all methods are approximated, the largest error is likely due to not track-  
 1349 ing the time-evolving depth of the reference isohaline  $z_{S_r}$ . Since there is no exact cal-  
 1350 culation for comparison, it is not possible to conclude which method, “adv” using the  
 1351 online advective term (eqn. B3.0) or “off” using the monthly mean Eulerian velocity and  
 1352 tracers (eqn. B3.2, is “more” correct in Fig. B2 and Table B1. It is likely that for gates  
 1353 where these two methods provide almost identical estimates (e.g., Bering, Davis and Fram  
 1354 Straits) we have higher confidence in our estimated FW transport. Across the CAA and  
 1355 the GSR the FW transport calculation depends strongly on the method employed and  
 1356 caution should be used in confidently reporting FW fluxes and comparing between dif-  
 1357 ferent studies.

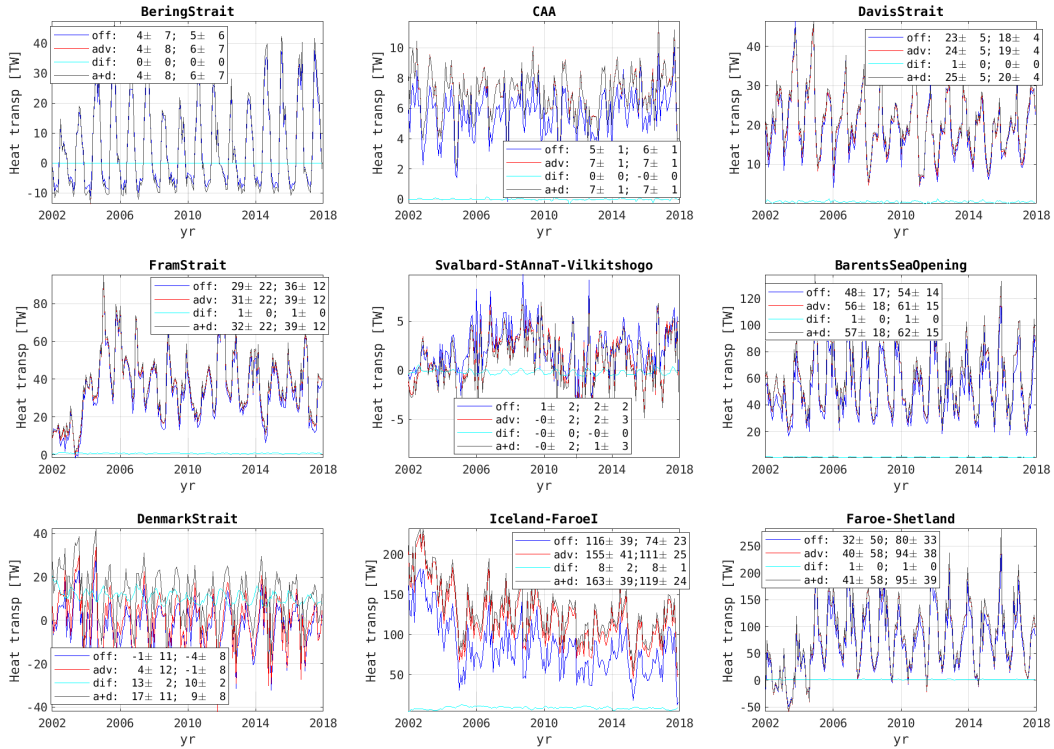


**Figure B1.** Time series of ocean heat transports (assuming a reference potential temperature  $\theta_r=0$ ) across important Arctic Mediterranean gateways using online (eqn. B2.0) and offline methods (“off”, eqn. B2.2), with the latter using outputs of monthly-averaged Eulerian velocity  $\langle \mathbf{u}_E \rangle$  and potential temperature  $\langle \theta \rangle$ . “adv” and “dif” are online calculations of the advective ( $F_{H\theta,adv}$ ) and diffusive ( $F_{H\theta,dif}$ ) terms for ocean transports on the RHS of eqn. (B2.0), and their sum is given by “a+d”. The quantities listed in the legend are the 2002–2006 and 2007–2017 means and month-to-month variability. The variability is computed after the seasonal cycle has been removed. As explained in the main text, statistics are reported separately for these two periods due to large observed changes in the Arctic around 2006/2007.

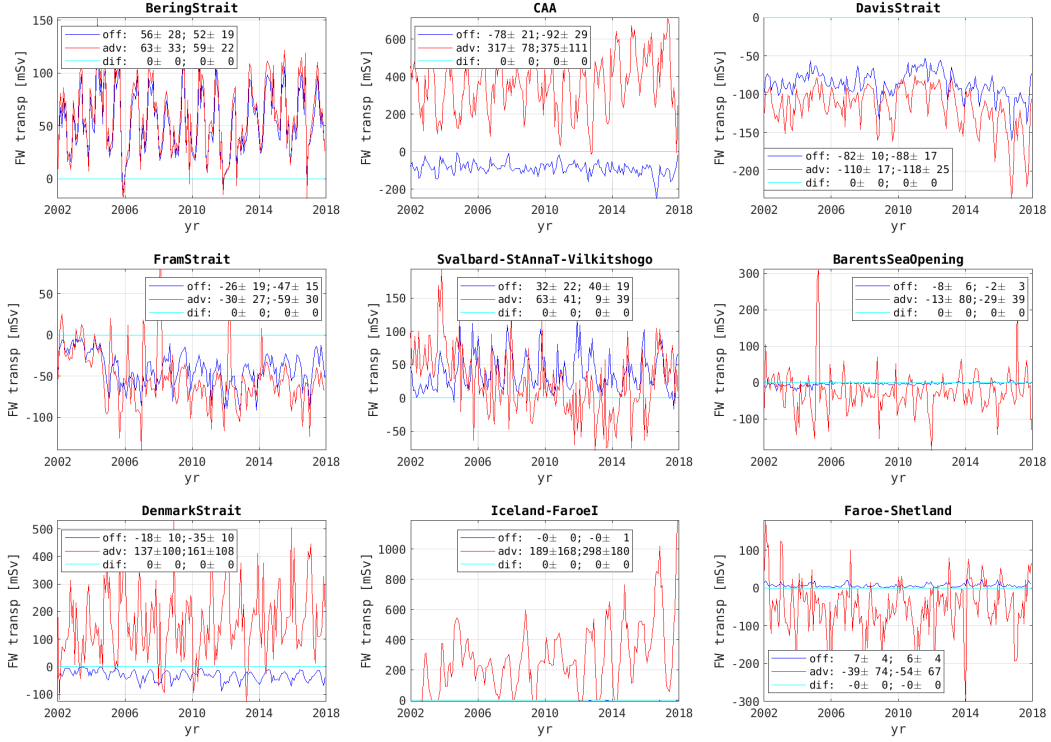


**Figure B2.** Time series of ocean freshwater transports (assuming a reference salinity  $S_r = 34.8$ ) across important Arctic Mediterranean gateways using online (eqn. B3.0) and of-line (eqn. B3.2) methods. Both methods incur errors due to reliance of the monthly  $\langle S \rangle$  for determining the depth of the reference isohaline  $z_{S_r}$  serving as the integral limit. “off” refers to eqn. (B3.2) which computes the transport offline using outputs of monthly-averaged Eulerian velocity  $\langle \mathbf{u}_E \rangle$  and salinity  $\langle S \rangle$ . “adv” and “dif” are the approximated online calculations of advective ( $F_{FW_S,adv}$ ) and diffusive ( $F_{FW_S,dif}$ ) terms on the RHS of eqn. (B3.0). The quantities listed in the legend are the 2002–2006 and 2007–2017 means and month-to-month variability. The variability is computed after the seasonal cycle has been removed. Note that “adv” is consistently larger than “off” (and with larger variability), but it is not possible to conclude that the online calculation is superior due to imperfect treatment of  $z_{S_r}$ . Instead, we assume higher confidence in both our FW flux estimation and our FW flux comparisons where “adv” and “off” converge.

Gate	FW Transports [mSv]	
(1) Bering Strait	<sup>a</sup> 61.32 ± 23.82	<sup>b</sup> 54.24 ± 20.62
(2) CAA	372.06 ± 109.98	-94.19 ± 31.60
(3) Fram Strait	-96.56 ± 34.85	-84.83 ± 23.29
(4) Svalbard-FJL <sup>1</sup> -SZ <sup>2</sup>	14.60 ± 43.37	45.23 ± 31.14
(5) Barents Sea Opening	-30.15 ± 38.18	-3.25 ± 3.30
(6) Davis Strait	-133.47 ± 26.66	-103.32 ± 19.59
(7) Denmark Strait	153.85 ± 106.71	-42.61 ± 12.21
(8) Iceland-Faroe	297.85 ± 178.35	-0.29 ± 0.69
(9) Faroe-Shetland	-53.61 ± 64.84	6.25 ± 4.29
(10) Newfoundland-Gr	-441.55 ± 242.66	-110.67 ± 23.44
(11) 48.3°N	-119.30 ± 38.67	-111.60 ± 22.80

**Table B1.** *ASTER1* Transports of freshwater ( $S_r=34.8$  ppt) for the combined ocean and ice system for the period 2006–2017. FW fluxes are estimated using <sup>a</sup>eqn. (B3.0) and <sup>b</sup>eqn. (B3.2). <sup>1</sup> Franz Josef Land, <sup>2</sup> Severnaya Zemlya.

## 1358 Appendix C Watermass definition in *ASTER1*

1359 Suitable specification of the characteristic salinity, potential temperature and density  
1360 ( $S$ ,  $\theta$ ,  $\sigma$ ) defining known watermasses can differ between observations and models  
1361 due to model biases, as shown in Fig. 14 in the main text for water properties in the Irminger  
1362 and Labrador Seas. Watermasses can be clearly identified in *ASTER1* as large volumes  
1363 with a common formation history and distinct properties from surrounding waters, con-  
1364 sistent with their definition in the literature. However in regions of hydrographic bias,  
1365 these watermasses will not be identified – or correctly quantified – as their observed coun-  
1366 terparts if they are tracked following the observed values too strictly. In this appendix,  
1367 we summarize the choices made in determining watermass and explore the sensitivity  
1368 to these choices where appropriate.

### 1369 C1 Volume transports of watermass

1370 Table C1 lists the watermass properties at Fram Strait (FS) and across the Greenland-  
1371 Scotland Ridge (GSR) used to identify the transports reported in Fig. 15 in the main  
1372 text. At the FS, the mean transports can be decomposed approximately into the West  
1373 Spitsbergen Current (WSC, east of 5°E, Beszczynska-Möller et al., 2012), recirculated  
1374 Atlantic Water (AW) (between 3.2°W and 5°E), and the East Greenland Current (EGC,  
1375 west of 3.2°W,  $S \leq 34$  ppt,  $T \leq 1^\circ\text{C}$ ). At the GSR definitions of watermasses such  
1376 as the surface outflow, dense outflow, modified water, and inflow AW from Østerhus et  
1377 al. (2019) and Hansen and Østerhus (2000) can be problematic when strictly applied to  
1378 grid-scale average quantities. For example, the densewater in the outflow through Den-  
1379 mark Strait (DS) is defined in Østerhus et al. (2019) as having density anomaly  $\sigma_\theta >$   
1380  $27.8$ , but in *ASTER1* outflow at the lowest depths of the strait are characterized by a  
1381 lower bound of  $\sigma_\theta$  ranging between  $27.28$  and  $27.81$ . For this range, the corresponding  
1382 southward transports are  $-1.6 \pm 0.9$  to  $0.5 \pm 0.3$  Sv (see Fig. 15, blue color text). Sim-  
1383 ilarly, over the Iceland-Faroe (IF) ridge, the southward transports of densewater defined  
1384 by  $\sigma_\theta \geq 22.44$  or  $\sigma_\theta \geq 27.55$  in *ASTER1* yield a range of  $-0.4$  to  $-0.3$  Sv, compared  
1385 to  $-0.4 \pm 0.3$  Sv of water with  $\sigma_\theta \geq 27.8$  in Østerhus et al. (2019). Similar considera-  
1386 tions applied also to dense water properties at the Faroe-Shetland (FSh) ridge ( $\sigma_\theta \geq$   
1387  $27.81$  in *ASTER1* compared to  $27.8$  in Østerhus et al., 2019). For the northward flow,  
1388 in addition to salinity thresholds ( $S \geq [34.8, 35, 35.25]$  ppt), temperature thresholds of  $\theta \geq$

1389  
1390

[5,4,5]<sup>°</sup>C are used in *ASTE\_R1* to identify the warm AW across the DS, IF, and FSh channels.

Gate	Watermass	Properties		Reference
		Obs	ASTE	
FS	WSC	lon > 5°E, T ≥ 2°C, σ <sub>θ</sub> ~ 27.97 kg/m <sup>3</sup>	lon ≥ 4°E, T ≥ 2°C	Beszczynska-Möller et al. (2012), Schauer and Beszczynska-Möller (2009)
		Recirc AW	-3.2°E < lon < 4°E, T ≥ 1°C, S > 34 ppt	
	deep AW	-2.5°E < lon < 5°E lon < -3°E	-3.2°E < lon < 4°E, T < 1°C,	Beszczynska-Möller et al. (2012)
	return flow		S > 34 ppt lon < -3.2°E	
	EGC	lon < -1°E	S < 34 ppt T ≤ 1°C	de Steur et al. (2014)
	DS	inflow AW	-	S > 34.8 ppt T > 5
dense outflow		σ <sub>θ</sub> > 27.8 kg/m <sup>3</sup>	S > 34.5, 34.8 ppt T < 3.5°C	
surface outflow		σ <sub>θ</sub> < 27.8 kg/m <sup>3</sup>	σ <sub>θ</sub> > 27.44, 27.81 kg/m <sup>3</sup> S ≤ 34.5 ppt	
IF	inflow AW	-	S > 35 ppt T > 5°C	Østerhus et al. (2019)
	dense outflow	σ <sub>θ</sub> > 27.8 kg/m <sup>3</sup>	35 ≥ S > 34.5, 34.7 ppt T ≤ 4, 5°C σ <sub>θ</sub> > 27.44, 27.55 kg/m <sup>3</sup>	
FSh	inflow AW	-	S > 35.25 ppt T > 5°C	Østerhus et al. (2019)
	dense outflow	σ <sub>θ</sub> > 27.8 kg/m <sup>3</sup>	σ <sub>θ</sub> > 27.87 kg/m <sup>3</sup> 35 ≥ S > 34.8 ppt T ≤ 2°C σ <sub>θ</sub> > 27.81, 27.97 kg/m <sup>3</sup>	

**Table C1.** Watermass at important Arctic Mediterranean gateway defined based on observations and in *ASTE\_R1*.

1391

## C2 Heat content of upper halocline watermass

1392  
1393  
1394  
1395  
1396  
1397  
1398  
1399

The upper halocline watermass, defined by Timmermans et al. (2018) as a layer within lower and upper salinity bounds of  $S_l=31.0$  ppt and  $S_u=33.0$  ppt, respectively, was identified based on subsurface in situ observations with fine vertical sampling resolution. In *ASTE\_R1*, with vertical grid spacing of 15–20 m within the water column depths 50–160 m, average salinity in the water column changes more abruptly than in the observations. For more accurate estimation of halocline-integrated quantities one approach is to “interpolate” the salinity in the vertical to a finer grid to find the exact depths at which salinity fits within the given bounds. Though this is often done during model-

1400 data comparisons (e.g., Grabon, 2020), the interpolation introduces additional informa-  
 1401 tion that was not strictly solved for by the model. An alternate approach is to vary the  
 1402 salinity bounds to gauge the sensitivity of the heat content within this watermass to the  
 1403 vertical discretization in the model. As an example, Fig. C1 shows a vertical section in  
 1404 *ASTE\_R1* through the Beaufort Gyre region as defined in Timmermans et al. (2018),  
 1405 with the watermass bounded between a temperature maximum at depths  $\sim 50$ – $60$  m (Pa-  
 1406 cific Summer Water, PSW,  $S_l=31$  salinity contour) and a temperature minimum at depths  
 1407  $\sim 150$  m (Pacific Winter Water, PWW,  $S_u=33$ ). In *ASTE\_R1*, negligible sensitivity is  
 1408 found with changes to  $S_u$ , but the heat content within the upper halocline in this region  
 1409 changes by approximately 1–2.5% per 0.1 ppt change in  $S_l$ . A change in  $S_l$  of  $\sim 0.5$  ppt  
 1410 corresponds approximately to one depth level in *ASTE\_R1*, and the heat content change  
 1411 associated with this is shown in shade in Fig. 18 in the main text.

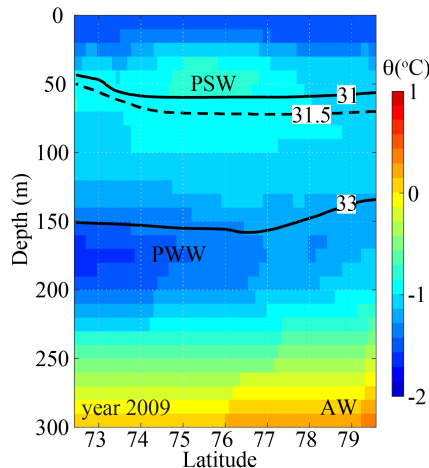


**Figure C1.** Vertical mean temperature for the year 2009 in a section across the Beaufort Gyre. Salinity contours are shown in black with white label, with the upper halocline watermass defined based on Timmermans et al. (2018) as bounded by  $S_l=31$  ppt (through the temperature maximum associated with the Pacific Summer Water PSW) and  $S_u=33$  ppt (through the temperature minimum associated with the Pacific Winter Water PWW). A change of  $S_l$  by 0.5 ppt corresponds approximately to 1 vertical depth level change in *ASTE\_R1*.

## 1412 Acknowledgments

1413 This work was supported by NSF-OPP-1603903, NSF-OPP-1708289, and NSF-OCE-1924546.  
 1414 Additional funding was provided from the ECCO project through a JPL/Caltech sub-  
 1415 contract. Computing resources were provided by the University of Texas at Austin Texas  
 1416 Advanced Computing Center (TACC) and NASA Advanced Supercomputing Division  
 1417 at the Ames Research Center. Adjoint code was generated using the TAF software tool,  
 1418 created and maintained by FastOpt GmbH (<http://www.fastopt.com/>). The *ASTE\_R1*  
 1419 model configuration, inputs, and monthly and daily outputs are available at the Arctic  
 1420 Data Center <https://arcticdata.io> and mirrored at  
 1421 <https://web.corral.tacc.utexas.edu/OceanProjects/ASTE/> and Amazon Web Services  
 1422 provided by TACC at  
 1423 <http://aste-release1.s3-website.us-east-2.amazonaws.com/>. Author ATN thanks M.-L.  
 1424 Timmermans and N. Foukal for providing heat content time-series for the Arctic halo-  
 1425 cline and eastern SPNA, and W. von Appen for the 2012–2017 processed Fram Strait  
 1426 mooring data used for *ASTE* post validation. We thank three anonymous reviewers for  
 1427 comments that greatly improved the manuscript.

1428

**References**

- 1429 Abernathey, R., Dussin, R., Smith, T., Bourgault, P., Bot, S., Doddridge, E.,  
 1430 ... Losch, M. (2020, November). *Mitgcm/xmitgcm: v0.5.0*. Zenodo.  
 1431 Retrieved from <https://doi.org/10.5281/zenodo.4288974> doi:  
 1432 10.5281/zenodo.4288974
- 1433 Abernathey, R. P., Busecke, J., Smith, T., Bot, S., Banihirwe, A., Zhang, C., ...  
 1434 Rath, W. (2020, October). *xgcm/xgcm: v0.5.1*. Zenodo. Retrieved from  
 1435 <https://doi.org/10.5281/zenodo.4097223> doi: 10.5281/zenodo.4097223
- 1436 Abernathey, R. P., Cerovecki, I., Holland, P. R., Newsom, E., Mazloff, M., & Talley,  
 1437 L. D. (2016). Water-mass transformation by sea ice in the upper branch of the  
 1438 Southern Ocean overturning. *Nature Geoscience*. doi: 10.1038/NNGEO2749
- 1439 Adcroft, A., & Campin, J.-M. (2004). Rescaled height coordinates for accurate rep-  
 1440 resentation of free-surface flows in ocean circulation models. *Ocean Modelling*,  
 1441 7(2004), 269–284. doi: 10.1016/j.ocemod.2003.09.003
- 1442 Adcroft, A., Campin, J.-M., Dutkiewicz, S., Evangelinos, C., Ferreira, D., Forget, G.,  
 1443 ... Molod, A. (2018). *MITgcm user manual*. doi: 1721.1/117188
- 1444 Adcroft, A., Campin, J.-M., Hill, C., & Marshall, J. (2004). Implementation of an  
 1445 atmosphere-ocean general circulation model on the expanded spherical cube.  
 1446 *Mon. Wea. Rev.*, 132(12), 2845–2863.
- 1447 Adcroft, A., Hill, C., & Marshall, J. (1997). Representation of topography by shaved  
 1448 cells in a height coordinate ocean model. *Mon. Wea. Rev.*, 125, 2293–2315.
- 1449 Adler, R., Sapiano, M. R. P., Huffman, G. J., Wang, J.-J., Gu, G., Bolvin, D., ...  
 1450 Shin, D.-B. (2018). The Global Precipitation Climatology Project (GPCP)  
 1451 Monthly Analysis (New Version 2.3) and a Review of 2017 Global Precipita-  
 1452 tion. *Atmosphere*, 9(138). doi: <https://doi.org/10.3390/atmos9040138>
- 1453 Andersen, O. B., P., K., & L., S. (2015). The DTU13 MSS (Mean Sea Surface) and  
 1454 MDT (Mean Dynamic Topography) from 20 Years of Satellite Altimetry. In  
 1455 J. S. & B. R. (Eds.), *Igfs 2014. international association of geodesy symposia*.  
 1456 Springer, Cham. doi: 10.1007/1345\_2015\_182
- 1457 Antonov, J. I., Seidov, D., Boyer, T. P., Locarnini, R. A., Mishonov, A. V., Garcia,  
 1458 H. E., ... Johnson, D. R. (2010). Volume 2: Salinity. In S. Levitus (Ed.), .  
 1459 NOAA Atlas NESDIS 68, U.S. Government Printing Office, Washington, D.C.
- 1460 Årthun, M., & Eldevik, T. (2016). On anomalous ocean heat transport toward the  
 1461 Arctic and associated climate predictability. *J. Clim.*, 29, 689–704. doi: 10  
 1462 .1175/JCLI-D-15-0448.1
- 1463 Asbjørnsen, H., Årthun, M., Skagseth, Ø., & Eldevik, T. (2019). Mechanisms of  
 1464 ocean heat anomalies in the norwegian sea. *Journal of Geophysical Research:  
 1465 Oceans*, 124(4), 2908–2923. Retrieved from [https://agupubs.onlinelibrary](https://agupubs.onlinelibrary.wiley.com/doi/abs/10.1029/2018JC014649)  
 1466 [.wiley.com/doi/abs/10.1029/2018JC014649](https://agupubs.onlinelibrary.wiley.com/doi/abs/10.1029/2018JC014649) doi: 10.1029/2018JC014649
- 1467 Balmaseda, M. A., Hernandez, F., Storto, A., Palmer, M. D., Alves, O., Shi, L.,  
 1468 ... Gaillard, F. (2015). The Ocean Reanalyses Intercomparison Project  
 1469 (ORA-IP). *Journal of Operational Oceanography*, 8(sub1), s80–s97. doi:  
 1470 10.1080/1755876X.2015.1022329
- 1471 Bamber, J. L., Tedstone, A. J., King, M. D., Howat, I. M., Enderlin, E. M., van den  
 1472 Broeke, M. R., & Noel, B. (2018). Land ice freshwater budget of the Arc-  
 1473 tic and North Atlantic Oceans: 1. Data, methods, and results. *Journal of  
 1474 Geophysical Research*, 123, 1827–1837. doi: 10.1002/2017JC013605
- 1475 Bamber, J. L., van den Broeke, M., Etema, J., Lenaerts, J., & Rignot, E. (2012).  
 1476 Recent large increases in freshwater fluxes from greenland into the North At-  
 1477 lantic. *Geophys. Res. Lett.*, 39. doi: 10.1029/2012GL052552
- 1478 Baringer, M. O., & Larsen, J. C. (2001). Sixteen years of Florida Current transport  
 1479 at 27°N. *Geophys. Res. Lett.*, 28(16), 3179–3182. doi: 10.1029/2001GL013246
- 1480 Bauch, D., Dmitrenko, I. A., Wegner, C., Hölemann, J., Kirillov, S. A., Timokhov,  
 1481 L. A., & Kassens, H. (2009). Exchange of laptev sea and arctic ocean halocline

- 1482 waters in response to atmospheric forcing. *J. Geophys. Res.*, *114*(C05008).  
 1483 (doi:10.1029/2008JC005062)
- 1484 Bauch, D., van der Loeff, M. R., Andersen, N., Torres-Valdes, S., Bakker, K., &  
 1485 Abrahamsen, E. (2011). Origin of freshwater and polynya water in the arctic  
 1486 ocean halocline in summer 2007. *Progress in Oceanography*, *91*, 482–495.  
 1487 (doi:10.1016/j.pocean.2011.07.017)
- 1488 Baumann, T. M., Polyakov, I. V., Pnyushkov, A. V., Rember, R., Ivanov, V. V.,  
 1489 Alkire, M. B., ... Carmack, E. C. (2018, 06). On the seasonal cycles observed  
 1490 at the continental slope of the eastern Eurasian Basin of the Arctic Ocean.  
 1491 *Journal of Physical Oceanography*, *48*(7), 1451–1470. Retrieved from [https://](https://doi.org/10.1175/JPO-D-17-0163.1)  
 1492 [doi.org/10.1175/JPO-D-17-0163.1](https://doi.org/10.1175/JPO-D-17-0163.1) doi: 10.1175/JPO-D-17-0163.1
- 1493 Beaird, N. L., Straneo, F., & Jenkins, W. (2018). Export of strongly diluted Green-  
 1494 land meltwater from a major glacial fjord. *Geophysical Research Letters*, *45*,  
 1495 4163–4170. doi: 10.1029/2018GL077000
- 1496 Bebieva, Y., & Timmermans, M.-L. (2016). An examination of double-diffusive  
 1497 processes in a mesoscale eddy in the Arctic Ocean. *Journal of Geophysical Re-*  
 1498 *search*, *121*, 457–475. doi: 10.1002/2015JC011105
- 1499 Beesley, J. A., Bretherton, C. S., Jakob, C., Andreas, E. L., Intrieri, J. M., & Ut-  
 1500 tal, T. A. (2000). A comparison of cloud and boundary layer variables in  
 1501 the ECMWF forecast model with observations at Surface Heat Budget of the  
 1502 Arctic Ocean (SHEBA) ice camp. *J. Geophys. Res.*, *105*(D10), 12337–12349.
- 1503 Bengtsson, L., Hagemann, S., & Hodges, K. I. (2004). Can climate trends be  
 1504 calculated from reanalysis data? *Journal of Geophysical Research: Oceans*,  
 1505 *109*(D11111). doi: 10.1029/2004JD004536
- 1506 Beszczynska-Möller, A., Fahrbach, E., Schauer, U., & Hansen, E. (2012). Vari-  
 1507 ability in Atlantic water temperature and transport at the entrance to  
 1508 the Arctic Ocean, 1997–2010. *ICES Journal of Marine Science*. doi:  
 1509 10.1093/icesjms/fss056
- 1510 Beszczynska-Möller, A., Woodgate, R. A., Lee, C., Melling, H., & Karcher, M.  
 1511 (2011). A synthesis of exchanges through the main oceanic gateways to the  
 1512 Arctic Ocean. *Oceanography*, *24*(3), 82–99. doi: [http://dx.doi.org/10.5670/](http://dx.doi.org/10.5670/oceanog.2011.59)  
 1513 [oceanog.2011.59](http://dx.doi.org/10.5670/oceanog.2011.59)
- 1514 Bigdeli, A., Loose, B., Nguyen, A. T., & Cole, S. T. (2017). Numerical investigation  
 1515 of the Arctic ice-ocean boundary layer and implications for air-sea gas fluxes.  
 1516 *Ocean Sci.*, *13*, 61–75. doi: 10.5194/os-13-61-2017
- 1517 Bigdeli, A., Nguyen, A. T., Pillar, H. R., na, V. O., & Heimbach, P. (2020). Atmo-  
 1518 spheric warming drives growth in Arctic sea-ice: A key role for snow. *Geophys-*  
 1519 *ical Research Letters*. (submitted)
- 1520 Buckley, M. W., Ponte, R. M., Forget, G., & Heimbach, P. (2014). Low-frequency  
 1521 SST and upper-ocean heat content variability in the North Atlantic. *J. Cli-*  
 1522 *mate*, *27*(13), 4996–5018. doi: 10.1175/JCLI-D-13-00316.1
- 1523 Buckley, M. W., Ponte, R. M., Forget, G., & Heimbach, P. (2015). Determining  
 1524 the origins of advective heat transport convergence variability in the North  
 1525 Atlantic. *J. Climate*, *28*, 3943–3956. doi: 10.1175/JCLI-D-14-00579.1
- 1526 Campin, J.-M., Adcroft, A., Hill, C., & Marshall, J. (2004). Conservation of proper-  
 1527 ties in a free-surface model. *Ocean Modelling*, *6*, 221–244. doi: 10.1016/S1463  
 1528 -5003(03)00009-X
- 1529 Carmack, E. C., Yamamoto-Kawai, M., Haine, T. W. N., Bacon, S., Bluhm, B. A.,  
 1530 Lique, C., ... Williams, W. J. (2016). Freshwater and its role in the Arctic  
 1531 marine system: Sources, disposition, storage, export, and physical and biogeo-  
 1532 chemical consequences in the Arctic and global oceans. *Journal of Geophysical*  
 1533 *Research: Biogeosciences*, *121*(3), 675–717. doi: 10.1002/2015JG003140
- 1534 Carton, J. A., Penny, S. G., & Kalnay, E. (2019, 04). Temperature and salinity  
 1535 variability in the SODA3, ECCO4r3, and ORAS5 ocean reanalyses, 1993–2015.  
 1536 *Journal of Climate*, *32*(8), 2277–2293. Retrieved from <https://doi.org/>

- 1537 10.1175/JCLI-D-18-0605.1 doi: 10.1175/JCLI-D-18-0605.1
- 1538 Chassignet, E. P., & Garraffo, Z. D. (2001). Viscosity parameterization and the Gulf  
1539 Stream separation. In P. Muller & D. Henderson (Eds.), *From stirring to mix-*  
1540 *ing in a stratified ocean* (pp. 37–41).
- 1541 Chassignet, E. P., & Marshall, D. P. (2013). Gulf stream separation in numerical  
1542 ocean models. In *Ocean modeling in an eddying regime* (p. 39–61). American  
1543 Geophysical Union (AGU). doi: 10.1029/177GM05
- 1544 Chassignet, E. P., & Xu, X. (2017). Impact of horizontal resolution ( $1/12^\circ$  to  $1/50^\circ$ )  
1545 on Gulf Stream separation, penetration, and variability. *Journal of Physical*  
1546 *Oceanography*, *47*, 1999–2021. doi: 10.1175/JPO-D-17-0031.1
- 1547 Chaudhuri, A. H., Ponte, R. M., Forget, G., & Heimbach, P. (2013). A Comparison  
1548 of Atmospheric Reanalysis Surface Products over the Ocean and Implications  
1549 for Uncertainties in Air–Sea Boundary Forcing. *J. Climate*, *26*(1), 153–170.  
1550 doi: 10.1175/JCLI-D-12-00090.1
- 1551 Chaudhuri, A. H., Ponte, R. M., & Nguyen, A. T. (2014). A comparison of  
1552 atmospheric reanalysis products for the Arctic Ocean and implications  
1553 for uncertainties in air–sea fluxes. *J. Climate*, *27*(14), 5411–5421. doi:  
1554 10.1175/JCLI-D-13-00424.1
- 1555 Cole, S. T., Timmermanns, M.-L., Toole, J. M., Krishfield, R. A., & Thwaites, F. T.  
1556 (2014). Ekman veering, internal waves, and turbulence observed under Arctic  
1557 sea ice. *J. Phys. Oceanogr.*, *44*, 1306–1328.
- 1558 Curry, B., Lee, C., & Petrie, B. (2011). Volume, freshwater, and heat fluxes through  
1559 Davis Strait, 2004–05. *Journal of Physical Oceanography*, *41*, 429–436. doi: 10  
1560 .1175/2010JPO4536.1
- 1561 Curry, B., Lee, C., Petrie, B., Moritz, R. E., & Kwok, R. (2014). Multiyear volume,  
1562 liquid freshwater, and sea ice transports through Davis Strait, 2004–10. *Jour-*  
1563 *nal of Physical Oceanography*, *44*, 1244–1266. doi: 10.1175/JPO-D-13-0177.1
- 1564 Dee, D. P., Uppala, S. M., Simmons, A. J., Berrisford, P., Poli, P., Kobayashi, S., ...  
1565 Vitart, F. (2011). The ERA-Interim reanalysis: configuration and performance  
1566 of the data assimilation system. *Q. J. R. Meteorol. Soc.*, *137*(656), 553–597.
- 1567 Dengg, J. (1993). The problem of Gulf Stream separation: A barotropic ap-  
1568 proach. *Journal of Physical Oceanography*, *23*(10), 2182–2200. doi:  
1569 10.1175/1520-0485(1993)023<2182:TPOGSS>2.0.CO;2
- 1570 de Steur, L., Hansen, E., Gerdes, R., Karcher, M., Fahrbach, E., & Holfort, J.  
1571 (2009). Freshwater fluxes in the East Greenland current: A decade of ob-  
1572 servations. *Geophys. Res. Lett.*, *36*(L23611). doi: 10.1029/2009GL041278
- 1573 de Steur, L., Hansen, E., Mauritzen, C., Beszczynska-Möller, A., & Fahrbach, E.  
1574 (2014). Impact of recirculation on the East Greenland Current in Fram Strait:  
1575 Results from moored current meter measurements between 1997 and 2009.  
1576 *Deep Sea Res.*, *92*, 26–40. doi: 10.1016/j.dsr.2014.05.018
- 1577 de Steur, L., Peralta Ferriz, C., & Pavlova, O. (2018). Freshwater export in the East  
1578 Greenland Current freshens the North Atlantic. *Geophysical Research Letters*,  
1579 *45*(24), 13359–13366. doi: 10.1029/2018GL080207
- 1580 Dmitrenko, I. A., Ivanov, V. V., Kirillov, S. A., Vinogradova, E. L., Torres-Valdes,  
1581 S., & Bauch, D. (2011). Properties of the Atlantic derived halocline waters  
1582 over the Laptev Sea continental margin: Evidence from 2002 to 2009. *J. Geo-*  
1583 *phys. Res.*, *116*(C10024). doi: 10.1029/2011JC007269
- 1584 Dmitrenko, I. A., Kirillov, S. A., Ivanov, V. V., Woodgate, R. A., Polyakov, I. V.,  
1585 Koldunov, N., ... Timokhov, L. A. (2009). Seasonal modification of the  
1586 Arctic Ocean intermediate water layer off the eastern Laptev Sea continental  
1587 shelf break. *Journal of Geophysical Research: Oceans*, *114*(C6). Retrieved  
1588 from [https://agupubs.onlinelibrary.wiley.com/doi/abs/10.1029/](https://agupubs.onlinelibrary.wiley.com/doi/abs/10.1029/2008JC005229)  
1589 [2008JC005229](https://agupubs.onlinelibrary.wiley.com/doi/abs/10.1029/2008JC005229) doi: 10.1029/2008JC005229
- 1590 Docquier, D., Grist, J. P., Roberts, M. J., Roberts, C. D., Semmler, T., Ponsoni,  
1591 L., ... Fichfet, T. (2019). Impact of model resolution on Arctic sea ice and

- 1592 North Atlantic Ocean heat transport. *Climate Dynamics*, *53*, 4989–5017. doi:  
1593 10.1007/s00382-019-04840-y
- 1594 Drange, H., Gerdes, R., Gao, Y., Karcher, M., Kauker, F., & Bentsen, M. (2005).  
1595 Ocean general circulation modelling of the Nordic Seas. In H. Drange,  
1596 T. Dokken, T. Furevik, R. Gerdes, & W. Berger (Eds.), *From the Nordic*  
1597 *Seas: An integrated perspective* (Vol. 158, pp. 199–220). American Geophysical  
1598 Union, Washington DC: AGU Monograph.
- 1599 Dukhovskoy, D. S., Myers, P. G., Platov, G., Timmermans, M.-L., Curry, B.,  
1600 Proshutinsky, A., . . . Somavilla, R. (2016). Greenland freshwater pathways in  
1601 the sub-Arctic seas from model experiments with passive tracers. *Journal of*  
1602 *Geophysical Research: Oceans*, *121*(1), 877–907. doi: 10.1002/2015JC011290
- 1603 Dukhovskoy, D. S., Yashayaev, I., Proshutinsky, A., Bamber, J. L., Bashmach-  
1604 nikov, I. L., Chassignet, E. P., . . . Tedstone, A. J. (2019). Role of Green-  
1605 land freshwater anomaly in the recent freshening of the subpolar North At-  
1606 lantic. *Journal of Geophysical Research: Oceans*, *124*(5), 3333–3360. doi:  
1607 10.1029/2018JC014686
- 1608 Ezer, T. (2016). Revisiting the problem of the Gulf Stream separation: on the repre-  
1609 sentation of topography in ocean models with different types of vertical grids.  
1610 *Ocean Modelling*, *104*, 15–27. doi: 10.1016/j.ocemod.2016.05.008
- 1611 Fahrback, E., Meincke, J., Osterhus, S., Rohardt, G., Schauer, U., Tverberg, V., &  
1612 Verduin, J. (2001). Direct measurements of volume transports through Fram  
1613 Strait. *Polar Research*, *20*(2), 217–224.
- 1614 Fenty, I., & Heimbach, P. (2013a). Coupled Sea Ice–Ocean–State Estimation in the  
1615 Labrador Sea and Baffin Bay. *J. Phys. Oceanogr.*, *43*(5), 884–904. doi: 10  
1616 .1175/JPO-D-12-065.1
- 1617 Fenty, I., & Heimbach, P. (2013b). Hydrographic preconditioning for seasonal sea  
1618 ice anomalies in the labrador sea. *J. Phys. Oceanogr.*, *43*(5), 863–883. doi: 10  
1619 .1175/JPO-D-12-064.1
- 1620 Fenty, I., Menemenlis, D., & Zhang, H. (2015). Global coupled sea ice-ocean state  
1621 estimate. *Clim. Dyn.* doi: 10.1007/s00382-015-2796-6
- 1622 Fer, I. (2014). Near-internal mixing in the central Arctic Ocean. *J. Phys. Oceanogr.*,  
1623 *44*, 2031–2049. doi: 10.1175/JPO-D-13-0133.1
- 1624 Forget, G., Campin, J.-M., Heimbach, P., Hill, C. N., Ponte, R. M., & Wunsch, C.  
1625 (2015a). ECCO version 4: an integrated framework for non-linear inverse mod-  
1626 eling and global ocean state estimation. *Geosci. Model Dev. Discuss.*, *8*(5),  
1627 3653–3743.
- 1628 Forget, G., Ferreira, D., & Liang, X. (2015b). On the observability of turbulent  
1629 transport rates by argo: supporting evidence from an inversion experiment.  
1630 *Ocean Sciences Diss.*, *12*(3), 1107–1143.
- 1631 Forget, G., & Wunsch, C. (2007). Global hydrographic variability and the data  
1632 weights in ocean state estimates. *J. Phys. Oceanogr.*, *37*, 1997–2008.
- 1633 Foukal, N. P., & Lozier, M. S. (2018). Examining the origins of ocean heat content  
1634 variability in the eastern North Atlantic subpolar gyre. *Geophysical Research*  
1635 *Letters*, *45*, 11,275–11,283. doi: <https://doi.org/10.1029/2018GL079122>
- 1636 Fournier, S., Lee, T., Tang, W., Steele, M., & Omeldo, E. (2019). Evaluation and  
1637 intercomparison of SMOS, Aquarius and SMAP sea surface salinity products  
1638 in the Arctic Ocean. *Remote Sensing*, *11*(3043). doi: 10.3390/rs11243043
- 1639 Fowler, C., Emery, W., & Tschudi, M. (2013). *Polar pathfinder daily 25 km ease-grid*  
1640 *sea ice motion vectors. version 2, northern hemisphere* (Tech. Rep.). Boulder,  
1641 Colorado, USA: National Snow and Ice Data Center. (NSIDC Technical Re-  
1642 port)
- 1643 Fox-Kemper, B., & Menemenlis, D. (2008). Can large eddy simulation techniques  
1644 improve mesoscale rich ocean models? In M. W. Hecht & H. Hasumi (Eds.),  
1645 *Ocean modeling in an eddying regime* (pp. 319–337). Washington, D. C.:  
1646 American Geophysical Union.

- 1647 Freville, H., Brun, E., Picard, G., Tatarinova, N., Arnaud, L., Lanconelli, C., ...  
 1648 van den Broeke, M. (2014). Using MODIS land surface temperatures and  
 1649 the Crocus snow model to understand the warm bias of ERA-Interim re-  
 1650 analyses at the surface in Antarctica. *The Cryosphere*, 8, 1361–1373. doi:  
 1651 10.5194/tc-8-1361-2014
- 1652 Fukumori, I., Fenty, I., Forget, G., Heimbach, P., King, C., Nguyen, A., ... Wang,  
 1653 O. (2018b). *Data sets used in ECCO Version 4 Release 3*. Retrieved from  
 1654 <http://hdl.handle.net/1721.1/120472>
- 1655 Fukumori, I., Heimbach, P., Ponte, R. M., & Wunsch, C. (2018a). A dynamically  
 1656 consistent, multi-variable ocean climatology. *Bulletin of the American Meteorolo-*  
 1657 *gical Society*, 0(0), null. (in press) doi: 10.1175/BAMS-D-17-0213.1
- 1658 Gent, P. R., & McWilliams, J. C. (1990). Isopycnal mixing in ocean circulation  
 1659 models. *J. Phys. Oceanogr.*, 20, 150–155.
- 1660 Germe, A., Houssais, M., Herbaut, C., & Cassou, C. (2011). Greenland Sea sea ice  
 1661 variability over 1979–2007 and its link to the surface atmosphere. *J. Geophys.*  
 1662 *Res.*, 116(C10034). doi: 10.1029/2011JC006960
- 1663 Giering, R., Kaminski, T., & Slawig, T. (2005, October). Generating efficient deriva-  
 1664 tive code with TAF. *Future Generation Computer Systems*, 21(8), 1345–1355.
- 1665 Gilbert, J., & Lemaréchal, C. (1989). Some numerical experiments with variable-  
 1666 storage quasi-newton algorithms. *Math. Program.*, 45(B), 407–435.
- 1667 Gopalakrishnan, G., Cornuelle, B. D., Hoteit, I., Rudnick, D. L., & Owens, W. B.  
 1668 (2013). State estimates and forecasts of the loop current in the Gulf of Mexico  
 1669 using the MITgcm and its adjoint. *Journal of Geophysical Research: Oceans*,  
 1670 118(7), 3292–3314. doi: 10.1002/jgrc.20239
- 1671 Grabon, J. S. (2020). *An analysis of Atlantic Water in the Arctic Ocean using the*  
 1672 *Arctic Subpolar gyre sTate Estimate and observations* (Unpublished master’s  
 1673 thesis). Massachusetts Institute of Technology, Cambridge, MA, USA. (90pp)
- 1674 Griffies, S. M. (2004). *Fundamentals of ocean climate models*. Princeton, NJ: Prince-  
 1675 ton University Press. (518pp)
- 1676 Griffies, S. M., Yin, J., Durack, P. J., Goddard, P., Bates, S. C., Behrens, E., ...  
 1677 Zhang, X. (2014). An assessment of global and regional sea level for years  
 1678 1993–2007 in a suite of interannual CORE-II simulations. *Ocean Modelling*,  
 1679 78(C), 35–89. doi: 10.1016/j.ocemod.2014.03.004
- 1680 Haine, T. W. N., Curry, B., Gerdes, R., Hansen, E., Karcher, M., Lee, C., ...  
 1681 Woodgate, R. A. (2015). Arctic freshwater export: Status, mechanisms, and  
 1682 prospects. *Global Planet. Change*, 125, 13–35. doi: [https://doi.org/10.1016/](https://doi.org/10.1016/j.gloplacha.2014.11.013)  
 1683 [j.gloplacha.2014.11.013](https://doi.org/10.1016/j.gloplacha.2014.11.013)
- 1684 Hansen, B., Larsen, K. M. H., Hátún, H., Kristiansen, R., Mortensen, E., & Øster-  
 1685 hus, S. (2015). Transport of volume, heat, and salt towards the Arctic in the  
 1686 Faroe Current 1993–2013. *Ocean. Sci.*, 11, 743. doi: [https://doi.org/10.5194/](https://doi.org/10.5194/os-11-743-2015)  
 1687 [os-11-743-2015](https://doi.org/10.5194/os-11-743-2015)
- 1688 Hansen, B., & Østerhus, S. (2000). North Atlantic–Nordic Seas exchanges. *Progress*  
 1689 *in Oceanography*, 45(2), 198–208. doi: [https://doi.org/10.1016/S0079-6611\(99\)](https://doi.org/10.1016/S0079-6611(99)00052-X)  
 1690 [00052-X](https://doi.org/10.1016/S0079-6611(99)00052-X)
- 1691 Hattermann, T., Isachsen, P. E., Appen, W.-J., Albretsen, J., & Sundfjord, A.  
 1692 (2016, April). Eddy-driven recirculation of Atlantic Water in Fram Strait.  
 1693 *Geophysical Research Letters*, 43(7), 3406–3414.
- 1694 Heimbach, P., Fukumori, I., Hill, C. N., Ponte, R. M., Stammer, D., Wunsch, C., ...  
 1695 Zhang, H. (2019, March). Putting It All Together: Adding Value to the Global  
 1696 Ocean and Climate Observing Systems With Complete Self-Consistent Ocean  
 1697 State and Parameter Estimates. *Frontiers in Marine Science*, 6, 769–10.
- 1698 Heimbach, P., Hill, C., & Giering, R. (2005). An efficient exact adjoint of the  
 1699 parallel MIT general circulation model, generated via automatic differentia-  
 1700 tion. *Future Generation Computer Systems*, 21(8), 1356–1371. doi:  
 1701 10.1016/j.future.2004.11.010

- 1702 Heimbach, P., Menemenlis, D., Losch, M., Campin, J.-M., & Hill, C. (2010). On  
 1703 the formulation of sea-ice models. Part 2: Lessons from multi-year adjoint  
 1704 sea-ice export sensitivities through the Canadian Arctic Archipelago. *Ocean*  
 1705 *Modelling*, *33*(1-2), 145–158. doi: 10.1016/j.ocemod.2010.02.002
- 1706 Heuzé, C., & Arthun, M. (2019). The Atlantic inflow across the Greenland-Scotland  
 1707 ridge in global climate models (CMIP5). *Elem. Sci. Anth.*, *7*(16). doi: <https://doi.org/10.1525/elementa.354>
- 1709 Holloway, G., Dupont, F., Golubeva, E., Hakkinen, S., Hunke, E., Jin, M., ...  
 1710 Zhang, J. (2007). Water properties and circulation in arctic ocean models.  
 1711 *J. Geophys. Res.*, *112*(C04S03). doi: 10.1029/2006JC003642
- 1712 Holmes, R. M., Coe, M. T., Fiske, G. J., Gurtovaya, T., McClelland, J. W., Shik-  
 1713 lomanov, A. I., ... Zhulidov, A. V. (2012). Climate change impacts on the  
 1714 hydrology and biogeochemistry of Arctic rivers. In *Climatic change and*  
 1715 *global warming of inland waters* (p. 1-26). John Wiley & Sons, Ltd. doi:  
 1716 <https://doi.org/10.1002/9781118470596.ch1>
- 1717 Ilicak, M., Drange, H., Wang, Q., Gerdes, R., Aksenov, Y., Bailey, D., ... Yeager,  
 1718 S. G. (2016). An assessment of the Arctic Ocean hydrography in a suite of  
 1719 interannual CORE-II simulations. part III: Hydrography and fluxes. *Ocean*  
 1720 *Modelling*, *100*, 141–161. doi: 10.1016/j.ocemod.2016.02.004
- 1721 Ivanov, V. V., Alexeev, V. A., Repina, I., Koldunov, N. V., & Smirnov, A. (2012).  
 1722 Tracing Atlantic water signature in the Arctic sea ice cover east of Svalbard.  
 1723 *Advances in Meteorology*, *2012*. doi: 10.1155/2012/201818
- 1724 Jackson, J. M., Carmack, E. C., McLaughlin, F. A., Allen, S. E., & Ingram, R. G.  
 1725 (2010). Identification, characterization, and change of the nearsurface tem-  
 1726 perature maximum in the Canada Basin, 1993–2008. *J. Geophys. Res.*,  
 1727 *115*(C05021). doi: 10.1029/2009JC005265
- 1728 Jahn, A., Aksenov, Y., de Cuevas, B. A., de Steur, L., Häkkinen, S., Hansen, E.,  
 1729 ... Zhang, J. (2012). Arctic ocean freshwater: How robust are model  
 1730 simulations? *Journal of Geophysical Research: Oceans*, *117*(C8). doi:  
 1731 10.1029/2012JC007907
- 1732 Jakobson, E., Vihma, T., Palo, T., Jakobson, L., Keemik, H., & Jaagus, J. (2012).  
 1733 Validation of atmospheric reanalyses over the central Arctic Ocean. *Geophys.*  
 1734 *Res. Lett.*, *39*(L10802). doi: 10.1029/2012GL051591
- 1735 Jakobsson, M., Mayer, L. A., Coakley, B., Dowdeswell, J. A., Forbes, S., Fridman,  
 1736 B., ... Weatherall, P. (2012). The International Bathymetric Chart of the  
 1737 Arctic Ocean (IBCAO) Version 3.0. *Geophysical Research Letters*. doi:  
 1738 10.1029/2012GL052219
- 1739 Janjić, T., Bormann, N., Bocquet, M., Carton, J. A., Cohn, S. E., Dance, S. L., ...  
 1740 Weston, P. (2017). On the representation error in data assimilation. *Quar-*  
 1741 *terly Journal of the Royal Meteorological Society*, *144*(713), 1257–1278. doi:  
 1742 10.1002/qj.3130
- 1743 Jochum, M., Danabasoglu, G., Holland, M., Kwon, Y.-O., & Large, W. G. (2008).  
 1744 Ocean viscosity and climate. *Journal of Geophysical Research*, *113*(C6). doi:  
 1745 10.1029/2007JC004515
- 1746 Johns, W. E., Townsend, T. L., Fratantoni, D. M., & Wilson, W. D. (2002). On the  
 1747 Atlantic inflow to the Caribbean Sea. *Deep-Sea Research Part I: Oceanographic*  
 1748 *Research Papers*, *49*(2), 211–243. doi: 10.1016/S0967-0637(01)00041-3
- 1749 Johnson, M., Gaffigan, S., Hunke, E., & Gerdes, R. (2007). A comparison of Arctic  
 1750 Ocean sea ice concentration among the coordinated AOMIP model experi-  
 1751 ments. *J. Geophys. Res.*, *112*(C04S11). doi: 10.1029/2006JC003690
- 1752 JPL\_MUR\_MEaSURES\_Project. (2015). *GHRSSST level 4 MUR global foundation*  
 1753 *sea surface temperature analysis (v4.1). ver. 4.1*. [https://doi.org/10.5067/](https://doi.org/10.5067/GHGMR-4FJ04)  
 1754 [GHGMR-4FJ04](https://doi.org/10.5067/GHGMR-4FJ04). (Dataset Accessed: 2017-11-08) doi: 10.5067/GHGMR-4FJ04
- 1755 Karcher, M., Smith, J. N., Kauker, F., Gerdes, R., & Jr., W. M. S. (2012). Recent  
 1756 changes in Arctic Ocean circulation revealed by iodine-129 observations and

- 1757 modeling. *J. Geophys. Res.*, *117*(C08007). doi: 10.1029/2011JC007513
- 1758 Kinney, J. C., Maslowski, W., Aksenov, Y., de Cuevas, B., Nguyen, A. T., Osinski,
- 1759 R., . . . Zhang, J. (2014). On the flow through Bering Strait: a synthesis of
- 1760 model results and observations. In J. Grebeier & W. Maslowski (Eds.), (pp.
- 1761 167–198). Dordrecht: Springer Dordrecht.
- 1762 Kobayashi, S., Ota, Y., Harada, Y., Ebata, A., Moriya, M., Onoda, H., . . . Taka-
- 1763 hashi, K. (2015). The JRA-55 Reanalysis: General Specifications and Basic
- 1764 Characteristics. *Journal of the Meteorological Society of Japan*, *93*(1), 5–48.
- 1765 doi: <https://doi.org/10.2151/jmsj.2015-001>
- 1766 Köhl, A. (2020). Evaluating the GECCO3 1948-2018 ocean synthesis a config-
- 1767 uration for initializing the MPIESM climate model. *Quarterly Journal of the*
- 1768 *Royal Meteorological Society*, *146*(730), 2250–2273. doi: 10.1002/qj.3790
- 1769 Köhl, A., & Stammer, D. (2008, 05). Decadal Sea Level Changes in the 50-Year
- 1770 GECCO Ocean Synthesis. *Journal of Climate*, *21*(9), 1876–1890. doi: 10.1175/  
1771 2007JCLI2081.1
- 1772 Krishfield, R. A. (2020). pers. comm.
- 1773 Krishfield, R. A., Toole, J. M., Proshutinsky, A., & Timmermans, M.-L. (2008).
- 1774 Automated ice-tethered profilers for seawater observations under pack
- 1775 ice in all seasons. *J. Atmos. Oceanic Technol.*, *25*(11), 2091–2105. doi:  
1776 10.1175/2008JTECHO587.1
- 1777 Kwok, R., & Cunningham, G. F. (2008). Icesat over arctic sea ice: Estima-
- 1778 tion of snow depth and ice thickness. *J. Geophys. Res.*, *113*(C08010).
- 1779 (doi:10.1029/2008JC004753)
- 1780 Kwok, R., & Cunningham, G. F. (2015). Variability of Arctic sea ice thickness and
- 1781 volume from CryoSat-2. *Phil. Trans. Royal Soc. A*, *373*. doi: 10.1098/rsta.2014  
1782 .0157
- 1783 Kwok, R., Cunningham, G. F., Wensnahan, M., Rigor, I., Zwally, H. J., & Yi, D.
- 1784 (2009). Thinning and volume loss of the arctic ocean sea ice cover: 2003-2008.
- 1785 *J. Geophys. Res.*, *114*(C07005). (10.1029/2009JC005312)
- 1786 Kwok, R., & Morison, J. (2016, January). Sea surface height and dynamic topogra-
- 1787 phy of the ice-covered oceans from CryoSat-2: 2011-2014. *Journal of Geophysi-*  
1788 *cal Research: Oceans*, *121*(1), 674–692.
- 1789 Lammers, R. B., & Shiklomanov, A. I. (2001). Assessment of contemporary Arc-
- 1790 tic river runoff based on observational discharge records. *J. Geophys. Res.*,  
1791 *106*(D4), 3321.
- 1792 Large, W. G., McWilliams, J., & Doney, S. (1994). Oceanic vertical mixing: A re-
- 1793 view and a model with nonlocal boundary layer parameterization. *Rev. Geo-*  
1794 *phys.*, *32*, 363–403.
- 1795 Large, W. G., & Yeager, S. G. (2008). The global climatology of an interannually
- 1796 varying air–sea flux data set. *Clim. Dyn.*, *33*(2–3), 341–364.
- 1797 Lavergne, T., Sørensen, A. M., Kern, S., Tonboe, R., Notz, D., Aaboe, S., . . . Ped-
- 1798 ersen, L. T. (2019). Version 2 of the EUMETSAT OSI SAF and ESA CCI
- 1799 sea-ice concentration climate data records. *The Cryosphere*, *13*(1), 49–78. doi:  
1800 10.5194/tc-13-49-2019
- 1801 Leith, C. E. (1968). Diffusion approximation for two-dimensional turbulence. *Phys.*  
1802 *Fluids*, *10*, 1409–1416.
- 1803 Leith, C. E. (1996). Stochastic models of chaotic systems. *Physica D*, *98*, 481–491.
- 1804 Levitus, S. (Ed.). (2010). *World ocean atlas 2009*. NOAA Atlas NESDIS 68, U.S.  
1805 Government Printing Office, Washington, D.C.
- 1806 Liang, X., Piecuch, C. G., Ponte, R. M., Forget, G., Wunsch, C., & Heimbach, P.
- 1807 (2017). Change of the global ocean vertical heat transport over 1993-2010.
- 1808 *Journal of Climate*, *14*(30), 5319–5327. doi: 10.1175/jcli-d-16-0569.1
- 1809 Lind, S., Ingvaldsen, R. B., & Furevik, T. (2018). Arctic warming hotspot in
- 1810 the northern Barents Sea linked to declining sea-ice import. *Nature climate*  
1811 *change*, *8*, 634–639. doi: <https://doi.org/10.1038/s41558-018-0205-y>

- 1812 Liu, C., Liang, X., Ponte, R. M., Vinogradova, N., & Wang, O. (2019). Vertical  
1813 redistribution of salt and layered changes in global ocean salinity. *Nat. Com-*  
1814 *mun.*, *10*(3445). doi: 10.1038/s41467-019-11436-x
- 1815 Locarnini, R. A., Mishonov, A. V., Antonov, J. I., Boyer, T. P., Garcia, H. E., Bara-  
1816 nova, O. K., . . . Johnson, D. R. (2010). Volume 1: Temperature. In S. Levitus  
1817 (Ed.), . NOAA Atlas NESDIS 68, U.S. Government Printing Office, Washing-  
1818 ton, D.C.
- 1819 Locarnini, R. A., Mishonov, A. V., Baranova, O. K., Boyer, T. P., Zweng, M. M.,  
1820 Garcia, H. E., . . . Smolyar, I. (2018). Volume 1: Temperature. In A. Mis-  
1821 honov (Ed.), . NOAA Atlas NESDIS 82, U.S. Government Printing Office,  
1822 Washington, D.C.
- 1823 Losch, M., Menemenlis, D., Campin, J.-M., Heimbach, P., & Hill, C. (2010). A  
1824 dynamic-thermodynamic sea ice model for ocean climate modeling on an  
1825 Arakawa C-grid: Part 1: Forward model sensitivities. *omod*, *33*(1-2), 129-144.  
1826 doi: 10.1016/j.ocemod.2009.12.008
- 1827 Lozier, M. S., Bacon, S., Bower, A. S., Cunningham, S. A., Femke de Jong, M., de  
1828 Steur, L., . . . Zika, J. D. (2017). Overturning in the Subpolar North Atlantic  
1829 Program: a new international ocean observing system. *Bull. Amer. Meteor.*  
1830 *Soc.*, *98*(4), 737–752.
- 1831 Lozier, M. S., Li, F., Bacon, S., Bahr, F., Bower, A. S., Cunningham, S. A., . . .  
1832 Zhao, J. (2019). A sea change in our view of overturning in the subpolar North  
1833 Atlantic. *Science*, *363*(6426), 516–521. doi: 10.1126/science.aau6592
- 1834 Lupkes, C., Vihma, T., Jakobson, E., Konig-Langlo, G., & Tetzlaff, A. (2010). Mete-  
1835 orological observations from ship cruises during summer to the central Arctic:  
1836 A comparison with reanalysis data. *Geophys. Res. Lett.*, *37*(L09810). doi:  
1837 10.1029/2010GL042724
- 1838 Manucharyan, G. E., & Isachsen, P. E. (2019). Critical role of continental slopes in  
1839 halocline and eddy dynamics of the Ekman-driven Beaufort Gyre. *Journal of*  
1840 *Geophysical Research*, *124*, 2679–2696. doi: 10.1029/2018JC014624
- 1841 Marnela, M., Rudels, B., Goszczko, I., Beszczynska-Möller, A., & Schauer, U.  
1842 (2016). Fram Strait and Greenland Sea transports, water masses, and wa-  
1843 ter mass transformations 1999–2010 (and beyond). *Journal of Geophysical*  
1844 *Research*, *121*(4), 2314–2346. doi: 10.1002/2015JC011312
- 1845 Marshall, J., Adcroft, A., Hill, C., Perelman, L., & Heisey, C. (1997). A finite-  
1846 volume, incompressible Navier stokes model for studies of the ocean on parallel  
1847 computers. *J. Geophys. Res.*, *102*, 5753–5766.
- 1848 Martin, T., Steele, M., & Zhang, J. (2014). Seasonality and long-term trend of Arc-  
1849 tic Ocean surface stress in a model. *J. Geophys. Res.*, *119*, 1723–1738. doi: 10  
1850 .1002/2013JC009425
- 1851 Mashayek, A., Ferrari, R., Merrifield, S., Ledwell, J. R., St Laurent, L., & Garabato,  
1852 A. N. (2017). Topographic enhancement of vertical turbulent mixing in the  
1853 Southern Ocean. *Nat. Commun.*, *8*(14197). doi: 10.1038/ncomms14197
- 1854 Mazloff, M. R., Heimbach, P., & Wunsch, C. (2010). An eddy-permitting Southern  
1855 Ocean State Estimate. *Journal of Physical Oceanography*, *40*(5), 880-899. doi:  
1856 10.1175/2009JPO4236.1
- 1857 Meneghello, G., Marshall, J., Cole, S. T., & Timmermans, M.-L. (2017). Obser-  
1858 vational inferences of lateral eddy diffusivity in the halocline of the Beau-  
1859 fort Gyre. *Geophysical Research Letters*, *44*(24), 12,331–12,338. doi:  
1860 10.1002/2017GL075126
- 1861 Meneghello, G., Marshall, J., Timmermans, M.-L., & Scott, J. (2018, 04). Ob-  
1862 servations of seasonal upwelling and downwelling in the Beaufort Sea me-  
1863 diated by sea ice. *Journal of Physical Oceanography*, *48*(4), 795-805. doi:  
1864 10.1175/JPO-D-17-0188.1
- 1865 Menemenlis, D., Hill, C., Adcroft, A., Campin, J.-M., Cheng, B., Ciotti, B., . . .  
1866 Zhang, J. (2005). Towards eddy permitting estimates of the global ocean and

- 1867 sea-ice circulation. *EOS Transactions AGU*, 86(9), 89.
- 1868 Mishonov, A. (Ed.). (2018). *World ocean atlas 2018*. NOAA Atlas NESDIS 82, U.S.  
1869 Government Printing Office, Washington, D.C.
- 1870 Moore, G. W. K., Straneo, F., & Oltmanns, M. (2014). Trend and inter-annual vari-  
1871 ability in southeast Greenland sea ice: Impacts on coastal Greenland climate  
1872 variability. *Geophys. Res. Lett.*, 41, 8619–8626. doi: 10.1002/2014GL062107
- 1873 Mu, L., Losch, M., Yang, Q., Ricker, R., Losa, S. N., & Nerger, L. (2018). Arc-  
1874 ticwide sea ice thickness estimates from combining satellite remote sens-  
1875 ing data and a dynamic iceocean model with data assimilation during the  
1876 CryoSat2 period. *Journal of Geophysical Research: Oceans*, 123, 7763–7780.  
1877 doi: 10.1029/2018JC014316
- 1878 Muilwijk, M., Smedsrud, L. H., Ilicak, M., & Drange, H. (2018). Atlantic water heat  
1879 transport variability in the 20th century Arctic Ocean from a global ocean  
1880 model and observations. *Journal of Geophysical Research: Oceans*, 123(11),  
1881 8159–8179.
- 1882 Munk, W. (1966). Abyssal recipes. *Deep Sea Research*, 13, 707–730.
- 1883 Nguyen, A. T., Heimbach, P., Garg, V. V., Ocaña, V., Lee, C., & Rainville, R.  
1884 (2020a). Impact of synthetic Arctic Argo-type floats in a coupled ocean-sea ice  
1885 state estimation framework. *J. Atmos. Ocean. Tech.*, 37(8), 1477–1495. doi:  
1886 10.1175/JTECH-D-19-0159.1.
- 1887 Nguyen, A. T., Menemenlis, D., & Kwok, R. (2011). Arctic ice-ocean simulations  
1888 with optimized model parameters: approach and assessment. *J. Geophys. Res.*,  
1889 116(C4), C04025. doi: 10.1029/2010JC006573
- 1890 Nguyen, A. T., Ocaña, V., Garg, V. V., Heimbach, P., Toole, J. M., Krishfield,  
1891 R. A., ... Rainville, R. (2017). On the benefit of current and future ALPS  
1892 data for improving Arctic coupled ocean-sea ice state estimation. *Oceanogra-*  
1893 *phy*, 30(2), 69–73. (ALPS II Special Issue) doi: 10.5670/oceanog.2017.223
- 1894 Nguyen, A. T., Pillar, H., Ocaña, V., Smith, T., & Heimbach, P. (2021a). *Arctic*  
1895 *Subpolar gyre sTate Estimate Release 1 (ASTE\_R1) data 2002–2017, monthly*  
1896 *averages and snapshots*, Arctic Data Center. [https://doi.org/10.18739/](https://doi.org/10.18739/A2CV4BS5K)  
1897 [A2CV4BS5K](https://doi.org/10.18739/A2CV4BS5K).
- 1898 Nguyen, A. T., Pillar, H., Ocaña, V., Smith, T., & Heimbach, P. (2021b). *Arctic*  
1899 *Subpolar gyre sTate Estimate Release 1 (ASTE\_R1) data 2002–2017,*  
1900 *depth-integrated monthly averages and snapshots*, Arctic Data Center.  
1901 <https://doi.org/10.18739/A2833N015>.
- 1902 Nguyen, A. T., Pillar, H., Ocaña, V., Smith, T., & Heimbach, P. (2021c). *Arctic*  
1903 *Subpolar gyre sTate Estimate Release 1 (ASTE\_R1) data 2002–2017, daily*  
1904 *averages*, Arctic Data Center. <https://doi.org/10.18739/A24B2X58W>.
- 1905 Nguyen, A. T., Pillar, H., Ocaña, V., Smith, T., & Heimbach, P. (2021d). *Arctic*  
1906 *Subpolar gyre sTate Estimate Release 1 (ASTE\_R1) data 2002–2017, 12-month*  
1907 *climatology*, Arctic Data Center. <https://doi.org/10.18739/A20P0WR8J>.
- 1908 Nguyen, A. T., Pillar, H., Ocaña, V., Smith, T., & Heimbach, P. (2021e). *Arctic*  
1909 *Subpolar gyre sTate Estimate Release 1 (ASTE\_R1) data 2002–2017, in-situ*  
1910 *profiles*, Arctic Data Center. <https://doi.org/10.18739/A2VX0643Z>.
- 1911 Nguyen, A. T., Pillar, H., Ocaña, V., Smith, T., & Heimbach, P. (2021f). *Arctic*  
1912 *Subpolar gyre sTate Estimate Release 1 (ASTE\_R1) data 2002–2017,*  
1913 *Grid files, Documentations and post-processing toolbox*, Arctic Data Center.  
1914 <https://doi.org/10.18739/A2MC8RH3V>.
- 1915 Nguyen, A. T., Pillar, H., Ocaña, V., Smith, T., & Heimbach, P. (2021g). *Arctic*  
1916 *Subpolar gyre sTate Estimate Release 1 (ASTE\_R1) data 2002–2017, re-*  
1917 *run\_ASTE\_R1*, Arctic Data Center. <https://doi.org/10.18739/A2R49G98G>.
- 1918 Nguyen, A. T., Woodgate, R. A., & Heimbach, P. (2020b). Elucidating large-  
1919 scale atmospheric controls on Bering Strait throughflow variability using a  
1920 data-constrained ocean model and its adjoint. *J. Geophys. Res.*, 125. doi:  
1921 10.1029/2020JC016213

- 1922 Nurser, A. J. G., & Bacon, S. (2014). The rossby radius in the Arctic Ocean. *Ocean.*  
 1923 *Sci.*, *10*, 967–975. Retrieved from [www.ocean-sci.net/10/967/2014](http://www.ocean-sci.net/10/967/2014) doi: 10  
 1924 .5194/os-10-967-2014
- 1925 Østerhus, S., Woodgate, R. A., Valdimarsson, H., Turrell, B., de Steur, L., Quad-  
 1926 fassel, D., ... Berx, B. (2019). Arctic Mediterranean exchanges: a consistent  
 1927 volume budget and trends in transports from two decades of observations.  
 1928 *Ocean. Sci.*, *15*, 379–399. doi: <https://doi.org/10.5194/os-15-379-2019>
- 1929 Padman, L., & Dillon, T. M. (1988). On the horizontal extent of thermohaline steps  
 1930 in the Canada Basin. *J. Phys. Oceanogr.*, *18*, 1458–1462.
- 1931 Peralta-Ferriz, C., Morison, J. H., Wallace, J. M., Bonin, J. A., & Zhang, J. (2014).  
 1932 Arctic Ocean circulation patterns revealed by GRACE. *J. Climate*, *27*(4),  
 1933 1445–1468. doi: 10.1175/JCLI-D-13-00013.1
- 1934 Peralta-Ferriz, C., & Woodgate, R. A. (2015). Seasonal and interannual vari-  
 1935 ability of pan-Arctic surface mixed layer properties from 1979 to 2012  
 1936 from hydrographic data, and the dominance of stratification for multiyear  
 1937 mixed layer depth shoaling. *Progress in Oceanography*, *134*, 19–53. doi:  
 1938 10.1016/j.pocean.2014.12.005
- 1939 Perovich, D. K., Richter-Menge, J., Jones, K., Light, B., Elder, B. C., Polashenski,  
 1940 C., ... Lindsay, R. (2011). Arctic sea-ice melt in 2008 and the role of solar  
 1941 heating. *Annals of Glaciology*, *52*(57), 355–359.
- 1942 Piecuch, C. G. (2017). *A note on practical evaluation of budgets in ecco version*  
 1943 *4 release 3* (Tech. Rep.). Retrieved from [http://hdl.handle.net/1721.1/  
 1944 111094](http://hdl.handle.net/1721.1/111094)
- 1945 Piecuch, C. G., & Ponte, R. M. (2012). Importance of circulation changes to At-  
 1946 lantic heat storage rates on seasonal and interannual time scales. *J. Climate*,  
 1947 *25*(1), 350–362. doi: 10.1175/JCLI-D-11-00123.1
- 1948 Piecuch, C. G., & Ponte, R. M. (2013). Mechanisms of global-mean steric sea level  
 1949 change. *Journal of Climate*, *27*, 824–834. doi: 10.1175/JCLI-D-13-00373.1
- 1950 Piecuch, C. G., Ponte, R. M., Little, C. M., Buckley, M. W., & Fukumori, I.  
 1951 (2017). Mechanisms underlying recent decadal changes in subpolar North  
 1952 Atlantic ocean heat content. *J. Geophys. Res.*, *122*, 7181–7197. doi:  
 1953 10.1002/2017JC012845
- 1954 Pillar, H. R., Heimbach, P., Johnson, H. L., & Marshall, D. P. (2016). Dynamical at-  
 1955 tribution of recent variability in Atlantic overturning. *J. Clim.*, *29*, 3339–3352.  
 1956 doi: 10.1175/JCLI-D-15-0727.1
- 1957 Pilo, G. S., Oke, P. R., Coleman, R., Rykova, T., & Ridgway, K. (2018). Impact  
 1958 of data assimilation on vertical velocities in an eddy resolving ocean model.  
 1959 *Ocean Modelling*, *131*, 71–85. doi: 10.1016/j.ocemod.2018.09.003
- 1960 Pnyushkov, A. V., Polyakov, I. V., Ivanov, V. V., Aksenov, Y., Coward, A. C.,  
 1961 Janout, M., & Rabe, B. (2015). Structure and variability of the boundary  
 1962 current in the Eurasian Basin of the Arctic Ocean. *Deep Sea Research Part I:  
 1963 Oceanographic Research Papers*, *101*, 80–97. doi: 10.1016/j.dsr.2015.03.001
- 1964 Pnyushkov, A. V., Polyakov, I. V., Ivanov, V. V., & Kikuchi, T. (2013). Structure of  
 1965 the Fram Strait branch of the boundary current in the Eurasian Basin in the  
 1966 Arctic Ocean. *Polar Science*, *7*(2). (10.1016/j.polar.2013.02.001)
- 1967 Pnyushkov, A. V., Polyakov, I. V., Padman, L., & Nguyen, A. T. (2018). Structure  
 1968 and dynamics of mesoscale eddies over the Laptev Sea continental slope in  
 1969 the Arctic Ocean. *Ocean Sci.*, *14*, 1329–1347. doi: [https://doi.org/10.5194/  
 1970 os-14-1329-2018](https://doi.org/10.5194/os-14-1329-2018)
- 1971 Polyakov, I. V., Alexeev, V. A., Ashik, I. M., Bacon, S., Beszczynska-Möller, A.,  
 1972 Carmack, E. C., ... Woodgate, R. A. (2011). Fate of early 2000s Arc-  
 1973 tic warm water pulse. *Bull. Amer. Meteor. Soc.*, *92*(5), 561–566. doi:  
 1974 10.1175/2010BAMS2921.1
- 1975 Polyakov, I. V., Pnyushkov, A. V., Alkire, M. B., Ashik, I. M., Baumann, T. M.,  
 1976 Carmack, E. C., ... Yulin, A. (2017). Greater role for Atlantic inflows on

- 1977 sea-ice loss in the Eurasian Basin of the Arctic Ocean. *Science*, *356*, 285–291.  
1978 doi: 10.1126/science.aai8204
- 1979 Polyakov, I. V., Pnyushkov, A. V., & Timokhov, L. A. (2012). Warming of the in-  
1980 termediate atlantic water of the arctic ocean in the 2000s. *J. Climate*, *25*(23),  
1981 8362–8370. doi: 10.1175/JCLI-D-12-00266.1
- 1982 Polyakov, I. V., Rippeth, T. P., Fer, I., Alkire, M. B., Baumann, T. M., Carmack,  
1983 E. C., ... Rember, R. (2020). Weakening of cold halocline layer exposes sea  
1984 ice to oceanic heat in the eastern Arctic Ocean. *Journal of Climate*. (in press)  
1985 doi: 10.1175/JCLI-D-19-0976.1
- 1986 Pradal, M.-A., & Gnanadesikan, A. (2014). How does the Redi parameter for  
1987 mesoscale mixing impact global climate in an Earth System Model? *J. Adv.*  
1988 *Model. Earth Syst.*, *6*, 586–601. doi: 10.1002/2013MS000273
- 1989 Project Jupyter, Matthias Bussonnier, Jessica Forde, Jeremy Freeman, Brian  
1990 Granger, Tim Head, ... Carol Willing (2018). Binder 2.0 - Reproducible,  
1991 interactive, sharable environments for science at scale. In Fatih Akici, David  
1992 Lippa, Dillon Niederhut, & M. Pacer (Eds.), *Proceedings of the 17th Python in*  
1993 *Science Conference* (p. 113 - 120). doi: 10.25080/Majora-4af1f417-011
- 1994 Proshutinsky, A., Krishfield, R. A., & Timmermans, M. L. (2020). Introduction  
1995 to special collection on Arctic Ocean modeling and observational synthe-  
1996 sis (FAMOS) 2: Beaufort Gyre phenomenon. *J. Geophys. Res.*, *125*. doi:  
1997 https://doi.org/10.1029/2019JC015400
- 1998 Proshutinsky, A., Krishfield, R. A., Timmermans, M.-L., Toole, J. M., Carmack, E.,  
1999 McLaughlin, F., ... Shimada, K. (2009). Beaufort Gyre freshwater reservoir:  
2000 State and variability from observations. *J. Geophys. Res.*, *114*(C1), C00A10.  
2001 doi: 10.1029/2008JC005104
- 2002 Proshutinsky, A., Krishfield, R. A., Toole, J. M., Timmermans, M.-L., Williams,  
2003 W., Zimmermann, S., ... Zhao, J. (2019). Analysis of the Beaufort Gyre  
2004 freshwater content in 20032018. *J. Geophys. Res.*, *124*, 9658–9689. doi:  
2005 https://doi.org/10.1029/2019JC015281
- 2006 Rabe, B., Karcher, M., Kauker, F., Schauer, U., Toole, J. M., Krishfield, R. A., ...  
2007 Su, J. (2014). Arctic Ocean basin liquid freshwater storage trend 1992–2012.  
2008 *Geophys. Res. Lett.*, *41*, 961–968. doi: 10.1002/2013GL058121
- 2009 Rainville, L., & Woodgate, R. A. (2009). Observations of internal wave generation in  
2010 the seasonally ice-free Arctic. *Geophys. Res. Lett.*, *36*(23), L23604.
- 2011 Redi, M. H. (1982). Oceanic isopycnal mixing by coordinate rotation. *J. Phys.*  
2012 *Oceanogr.*, *12*, 1154–1158.
- 2013 Richter-Menge, J., & Jeffries, M. (2011). The Arctic. *Bulletin American Meteorolog-*  
2014 *ical Society*, *92*, S143-S160.
- 2015 Ricker, R., Tian-Kunze, S. H. L. K. X., King, J., & Haas, C. (2017). A weekly Arc-  
2016 tic sea-ice thickness data record from merged CryoSat-2 and SMOS satellite  
2017 data. *The Cryosphere*, *11*, 1607–1623. doi: 10.5194/tc-11-1607-2017
- 2018 Rossby, T., Flagg, C., Chafik, L., Harden, B., & Søiland, H. (2018). A direct  
2019 estimate of volume, heat, and freshwater exchange across the Greenland-  
2020 Iceland-Faroe-Scotland ridge. *J. Geophys. Res.*, *123*, 7139–7153. doi:  
2021 https://doi.org/10.1029/2018JC014250
- 2022 Roulet, G., & Madec, G. (2000). Salt conservation, free surface, and varying lev-  
2023 els: a new formulation for ocean general circulation models. *J. Geophys. Res.*,  
2024 *105*(C10), 23927–23942.
- 2025 Rudels, B. (2012). Arctic ocean circulation and variability - advection and external  
2026 forcing encounter constraints and local processes. *Ocean Science*, *8*(2), 261–  
2027 286. doi: 10.5194/os-8-261-2012
- 2028 Rudels, B. (2015). Arctic Ocean circulation, processes and water masses: A de-  
2029 scription of observations and ideas with focus on the period prior to the Inter-  
2030 national Polar Year 2007–2009. *Progress in Oceanography*, *132*, 22–67. doi:  
2031 10.1016/j.pocean.2013.11.006

- 2032 Rudels, B., Jones, E. P., Schauer, U., & Eriksson, P. (2004). Atlantic sources of the  
2033 Arctic Ocean surface and halocline waters. *Polar Research*, *23*(2), 81–208.
- 2034 Schauer, U., & Beszczynska-Möller, A. (2009). Problems with estimation and  
2035 interpretation of oceanic heat transport—conceptual remarks for the case  
2036 of Fram Strait in the Arctic Ocean. *Ocean Science*, *5*, 487–494. doi:  
2037 <https://doi.org/10.5194/os-5-487-2009>
- 2038 Schauer, U., & Fahrbach, E. (2004). Arctic warming through the Fram Strait:  
2039 Oceanic heat transport from 3 years of measurements. *J. Geophys. Res.*,  
2040 *109*(C06026). doi: 10.1029/2003JC001823
- 2041 Schauer, U., & Losch, M. (2019). “freshwater” in the ocean is not a useful parameter  
2042 in climate research. *Journal of Physical Oceanography*, *49*(9), 2309–2321. doi:  
2043 10.1175/JPO-D-19-0102.1
- 2044 Sciascia, R., Straneo, F., Cenedese, C., & Heimbach, P. (2013). Seasonal variability  
2045 of submarine melt rate and circulation in an East Greenland fjord. *Journal of*  
2046 *Geophysical Research*, *118*, 2492–2506. doi: 10.1002/jgrc.20142
- 2047 Shiklomanov, A. I., Déry, S., Tretiakov, M., Yang, D., Magritsky, D., Georgiadi, A.,  
2048 & Tang, W. (2020, August). River Freshwater Flux to the Arctic Ocean. In  
2049 *Arctic hydrology, permafrost and ecosystems* (pp. 703–738). Cham: Springer  
2050 International Publishing.
- 2051 Shiklomanov, A. I., Yakovleva, T. I., Lammers, R. B., Karasev, I. P., Vörösmarty,  
2052 C. J., & Linder, E. (2006). Cold region river discharge uncertainty—estimates  
2053 from large Russian rivers. *Journal of Hydrology*, *326*(1–4), 231–256.
- 2054 Sirevaag, A., & Fer, I. (2012). Vertical heat transfer in the Arctic Ocean: the role  
2055 of double-diffusive mixing. *J. Geophys. Res.*, *117*(C07010). doi: doi:10.1029/  
2056 2012JC007910
- 2057 Sivareddy, S., Paul, A., Sluka, T., Ravichandran, M., & Kalnay, E. (2017). The  
2058 pre-Argo ocean reanalyses may be seriously affected by the spatial coverage of  
2059 moored buoys. *Scientific Reports*, *7*(46685). doi: 10.1038/srep46685
- 2060 Skagseth, O., Furevik, T., Ingvaldsen, R., Loeng, H., Mork, K. A., Orvik, K. A.,  
2061 & Ozhigin, V. (2008). Chapter: Volume and heat transports to the Arctic  
2062 Ocean via the Norwegian and Barents Seas. In R. R. Dickson, J. Meincke,  
2063 & P. Rhines (Eds.), *Arctic subarctic ocean fluxes* (pp. 45–64). Netherlands:  
2064 Springer. doi: [https://doi.org/10.1007/978-1-4020-6774-7\\_3](https://doi.org/10.1007/978-1-4020-6774-7_3)
- 2065 Smedsrud, L. H., Ingvaldsen, R., Nilsen, J. E. O., & Skagseth, O. (2010). Heat in  
2066 the Barents Sea: Transport, storage and surface fluxes. *Ocean Sci.*, *6*(1), 219–  
2067 234. doi: <https://doi.org/10.5194/os-6-219-2010>
- 2068 Smith, T. (2021, January). *crios-ut/aste: Aste release 1*. Zenodo. Retrieved from  
2069 <https://doi.org/10.5281/zenodo.4479779> doi: 10.5281/zenodo.4479779
- 2070 Smith, W., & Sandwell, D. T. (1997). Global sea floor topography from satellite al-  
2071 timetry and ship depth soundings. *Science*, *277*(5334), 1956–1962.
- 2072 Spall, M. A. (2020, 08). Potential vorticity dynamics of the Arctic halocline. *Journal*  
2073 *of Physical Oceanography*, *50*(9), 2491–2506. doi: 10.1175/JPO-D-20-0056.1
- 2074 Spreen, G., Kern, S., Stammer, D., & Hansen, E. (2009). Fram Strait sea ice volume  
2075 export estimated between 2003 and 2008 from satellite data. *Geophys. Res.*  
2076 *Lett.*, *36*(L19502). doi: 10.1029/2009GL039591
- 2077 Stammer, D., Balmaseda, M., Heimbach, P., Köhl, A., & Weaver, A. (2016). Ocean  
2078 data assimilation in support of climate applications: Status and perspectives.  
2079 *Annu. Rev. Mar. Sci.*, *8*(accepted). doi: 10.1146/annurev-marine-122414  
2080 -034113
- 2081 Stammer, D., Wunsch, C., Giering, R., Eckert, C., Heimbach, P., Marotzke, J., ...  
2082 Marshall, J. (2002). Global ocean circulation during 1992–1997, estimated  
2083 from ocean observations and a general circulation model. *Journal of Geophys-  
2084 ical Research*, *107*(C9), 3118–1–27.
- 2085 Steele, M., Morley, R., & Ermold, W. (2001). PHC: A global ocean hydrography  
2086 with a high-quality arctic ocean. *J. Clim.*, *14*, 2079–2087.

- 2087 Straneo, F., & Cenedese, C. (2015). The dynamics of Greenlands glacial fjords and  
 2088 their role in climate. *Annu. Rev. Mar. Sci.*, *7*, 89112. doi: 10.1146/annurev-  
 2089 -marine-010213-135133
- 2090 Tesdal, J.-E., & Haine, T. W. N. (2020). Dominant terms in the freshwater and  
 2091 heat budgets of the subpolar North Atlantic Ocean and Nordic Seas from  
 2092 1992 to 2015. *J. Geophys. Res.*. (submitted) doi: [https://doi.org/10.1002/](https://doi.org/10.1002/essoar.10503232.1)  
 2093 [essoar.10503232.1](https://doi.org/10.1002/essoar.10503232.1)
- 2094 Tian-Kunze, X., Kaleschke, L., Maass, N., Maekynen, M., Serra, N., Drusch, M., &  
 2095 Krumpfen, T. (2014). SMOS-derived sea ice thickness: algorithm baseline,  
 2096 product specifications and initial verification. *The Cryosphere*, *8*, 997–1018.  
 2097 (doi:10.5194/tc-8-997-2014)
- 2098 Timmermans, M.-L., Cole, S., & Toole, J. M. (2012). Horizontal density struc-  
 2099 ture and restratification of the Arctic Ocean surface layer. *J. Phys. Oceanogr.*,  
 2100 *42*(4), 659–668. doi: 10.1175/JPO-D-11-0125.1
- 2101 Timmermans, M.-L., & Jayne, S. R. (2016). The Arctic Ocean spices up. *Journal of*  
 2102 *Physical Oceanography*, *46*, 1277–1284. doi: 10.1175/JPO-D-16-0027.1
- 2103 Timmermans, M.-L., & Marshall, J. (2020). Understanding Arctic Ocean circulation:  
 2104 A review of ocean dynamics in a changing climate. *Journal of Geophysical Re-*  
 2105 *search*, *125*(4), e2018JC014378. doi: 10.1029/2018JC014378
- 2106 Timmermans, M.-L., Toole, J. M., & Krishfield, R. A. (2018). Warming of the in-  
 2107 terior Arctic Ocean linked to sea ice losses at the basin margins. *Science Ad-*  
 2108 *vances*, *4*(8). doi: 10.1126/sciadv.aat6773
- 2109 Toohey, R. C., Herman-Mercer, N. M., Schuster, P. F., Mutter, E. A., & Koch, J. C.  
 2110 (2016). Multidecadal increases in the Yukon River Basin of chemical fluxes as  
 2111 indicators of changing flowpaths, groundwater, and permafrost. *Geophys. Res.*  
 2112 *Let.*, *43*, 12120–12,130. doi: 10.1002/2016GL070817
- 2113 Toole, J. M. (2007). Temporal characteristics of abyssal finescale motions above  
 2114 rough bathymetry. *Journal of Physical Oceanography*, *37*(3), 409-427. Re-  
 2115 trieved from <https://doi.org/10.1175/JP02988.1> doi: 10.1175/JPO2988  
 2116 .1
- 2117 Toole, J. M., Krishfield, R. A., & Timmermans, M.-L. (2011). The ice-tethered pro-  
 2118 filer: Argo of the Arctic. *Oceanography*, *24*(3), 126–135. doi: 10.5670/oceanog  
 2119 .2011.64
- 2120 Treguier, A. M., Deshayes, J., Le Sommer, J., Lique, C., Madec, G., Penduff,  
 2121 T., ... Talandier, C. (2014). Meridional transport of salt in the global  
 2122 ocean from an eddy-resolving model. *Ocean Science*, *10*(2), 243–255. doi:  
 2123 10.5194/os-10-243-2014
- 2124 Tsubouchi, T., Bacon, S., Aksenov, Y., Garabato, A. C. N., Beszczynska-Möller, A.,  
 2125 Hansen, E., ... Lee, C. M. (2018). The Arctic Ocean seasonal cycles of heat  
 2126 and freshwater fluxes: Observation-based inverse estimates. *Journal of Physical*  
 2127 *Oceanography*, *48*(9), 2029–2055. doi: 10.1175/JPO-D-17-0239.1
- 2128 Uotila, P., Goosse, H., Haines, K., Chevallier, M., Barthélemy, A., Bricaud, C., ...  
 2129 Zhang, Z. (2019). An assessment of ten ocean reanalyses in the polar regions.  
 2130 *Clim Dyn*, *52*, 1613–1650. doi: 10.1007/s00382-018-4242-z
- 2131 Verdy, A., Cornuelle, B., Mazloff, M. R., & Rudnick, D. L. (2017). Estimation of the  
 2132 tropical Pacific Ocean state 2010-13. *J. Atm. Oceanic Tech.*, *34*, 1501–1517.  
 2133 doi: 10.1175/JTECH-D-16-0223.1
- 2134 Vinogradova, N. T., & Ponte, R. M. (2012). Assessing temporal aliasing in satellite-  
 2135 based salinity measurements. *J. Atmos. Ocean. Technol.*, *29*(9), 1391–1400.  
 2136 doi: 10.1175/JTECH-D-11-00055.1
- 2137 von Appen, W.-J., Schauer, U., Hattermann, T., & Beszczynska-Möller, A. (2015a).  
 2138 Seasonal cycle of mesoscale instability of the West Spitsbergen Current. *Jour-*  
 2139 *nal of Physical Oceanography*, 1231–1254. doi: doi:10.1175/jpo-d-15-0184.1
- 2140 von Appen, W.-J., Schauer, U., Somavilla Cabrillo, R., Bauerfeind, E., &  
 2141 Beszczynska-Möller, A. (2015b). Exchange of warming deep waters across

- 2142 Fram Strait. *Deep Sea Res.*, 86–100. doi: doi:10.1016/j.dsr.2015.06.003
- 2143 Våge, K., Moore, G. W. K., Jónsson, S., & Valdimarsson, H. (2015). Water  
2144 mass transformation in the Iceland Sea. *Deep Sea Res. Part I*, 101, 98–109.  
2145 (doi:10.1016/j.dsr.2015.04.001)
- 2146 Wadhams, P., Comiso, J. C., Prussen, E., Wells, S., Brandon, M., Aldworth, E., ...  
2147 Crane, D. R. (1996). The development of the Oden ice tongue in the Green-  
2148 land Sea during winter 1993 from remote sensing and field observations. *J.*  
2149 *Geophys. Res.*, 101(C8), 18213–18235.
- 2150 Wang, C., Graham, R. M., Wang, K., Gerland, S., & Granskog, M. A. (2019).  
2151 Comparison of ERA5 and ERA-Interim near-surface air temperature, snowfall  
2152 and precipitation over Arctic sea ice: effects on sea ice thermodynamics and  
2153 evolution. *The Cryosphere*, 13(6), 1661–1679. doi: 10.5194/tc-13-1661-2019
- 2154 Wang, Q., Ilicak, M., Gerdes, R., Drange, H., Aksenov, Y., Bailey, D. A., ... Yeager,  
2155 S. G. (2016a). An assessment of the Arctic Ocean in a suite of interannual  
2156 CORE-II simulations. part ii: Liquid freshwater. *Ocean Modelling*, 99, 86–109.  
2157 Retrieved from [http://www.sciencedirect.com/science/article/pii/](http://www.sciencedirect.com/science/article/pii/S1463500315002450)  
2158 [S1463500315002450](http://www.sciencedirect.com/science/article/pii/S1463500315002450) doi: <https://doi.org/10.1016/j.ocemod.2015.12.009>
- 2159 Wang, Q., Ilicak, M., Gerdes, R., Drange, H., Aksenov, Y., Bailey, D. A., ... Yeager,  
2160 S. G. (2016b). An assessment of the Arctic Ocean in a suite of interannual  
2161 CORE-II simulations. part i: Sea ice and solid freshwater. *Ocean Modelling*,  
2162 99, 110–132. doi: <https://doi.org/10.1016/j.ocemod.2015.12.008>
- 2163 Wang, Q., Wekerle, C., Wang, X., Danilov, S., Koldunov, N., Sein, D., ... Jung,  
2164 T. (2020). Intensification of the Atlantic Water supply to the Arctic Ocean  
2165 through Fram Strait induced by Arctic sea ice decline. *Geophysical Research*  
2166 *Letters*, 47(3). doi: 10.1029/2019GL086682
- 2167 Watkins, M. M., Wiese, D. N., Yuan, D.-N., Böning, C., & Landerer, F. W. (2015).  
2168 Improved methods for observing earth’s time variable mass distribution with  
2169 GRACE using spherical cap mascons. *J. Geophys. Res.*, 120(4), 2648–2671.  
2170 doi: 10.1002/2014JB011547
- 2171 Weijer, W., Maltrud, M. E., Hecht, M. W., Dijkstra, H. A., & Kliphuis, M. A.  
2172 (2012). Response of the Atlantic Ocean circulation to Greenland Ice Sheet  
2173 melting in a strongly-eddy ocean model. *Geophys. Res. Lett.*, 39(L09606).  
2174 doi: 10.1029/2012GL051611
- 2175 Wiese, D., Yuan, N., Böning, C., Landerer, F. W., & Watkins, M. M. (2018). *JPL*  
2176 *GRACE mascon ocean, ice, and hydrology equivalent water height release 06*  
2177 *coastal resolution improvement (cri) filtered version 1.0. ver. 1.0. po.daac, ca,*  
2178 *usa.* <https://doi.org/10.5067/TEMSC-3MJC6>. (Dataset Accessed: 2019-11-  
2179 08) doi: 10.5067/TEMSC-3MJC6
- 2180 Wolfe, C. L., Hameed, S., & Chi, L. (2019). On the drivers of decadal variability of  
2181 the Gulf Stream North Wall. *J. Climate*, 32, 1235–1249. doi: 10.1175/JCLI-D  
2182 -18-0212.1
- 2183 Woodgate, R. A. (2018). Increases in the Pacific inflow to the Arctic from 1990  
2184 to 2015, and insights into seasonal trends and driving mechanisms from year-  
2185 round Bering Strait mooring data. *Progress in Oceanography*, 160, 124–154.  
2186 doi: <https://doi.org/10.1016/j.pocean.2017.12.007>
- 2187 Woodgate, R. A., Stafford, K. J., & Prah, F. G. (2015). A synthesis of year-round  
2188 interdisciplinary mooring measurements in the Bering Strait (1990–2014)  
2189 and the RUSALCA years (2004–2011). *Oceanography*, 28(3), 46–67. doi:  
2190 10.5670/oceanog.2015.57
- 2191 Wunsch, C. (2018). Towards determining uncertainties in global oceanic mean val-  
2192 ues of heat, salt, and surface elevation. *Tellus A: Dynamic Meteorology and*  
2193 *Oceanography*, 70(1), 1–14. doi: 10.1080/16000870.2018.1471911
- 2194 Wunsch, C., & Heimbach, P. (2007). Practical global oceanic state estimation. *Phys-*  
2195 *ica D: Nonlinear Phenomena*, 230(1-2), 197–208. doi: 10.1016/j.physd.2006.09  
2196 .040

- 2197 Wunsch, C., & Heimbach, P. (2013). Dynamically and Kinematically Consistent  
 2198 Global Ocean Circulation and Ice State Estimates. In *Ocean circulation and*  
 2199 *climate: A 21st century perspective* (pp. 553–579). Elsevier Ltd. doi: 10.1016/  
 2200 B978-0-12-391851-2.00021-0
- 2201 Yang, J. (2005). The Arctic and subarctic ocean flux of potential vorticity and the  
 2202 Arctic Ocean circulation. *J. Phys. Oceanogr.*, *35*, 2387–2407.
- 2203 Yin, J., Stouffer, R. J., Spelman, M. J., & Griffies, S. M. (2010). Evaluat-  
 2204 ing the uncertainty induced by the virtual salt flux assumption in climate  
 2205 simulations and future projections. *Journal of Climate*, *23*, 80–96. doi:  
 2206 10.1175/2009JCLI3084.1
- 2207 Zaba, K. D., Rudnick, D. L., Cornuelle, B. D., Gopalakrishnan, G., & Mazloff, M. R.  
 2208 (2018). Annual and interannual variability in the California Current System:  
 2209 comparison of an ocean state estimate with a network of underwater gliders. *J.*  
 2210 *Phys. Oceanogr.*, *48*, 2965–2988. doi: 10.1175/JPO-D-18-0037.1
- 2211 Zhang, J., & Rothrock, D. A. (2003). Modeling global sea ice with a thickness  
 2212 and enthalpy distribution model in generalized curvilinear coordinates. *Mon.*  
 2213 *Weather Rev.*, *131*, 845–861.
- 2214 Zhang, J., & Steele, M. (2007). Effect of vertical mixing on the atlantic wa-  
 2215 ter layer circulation in the arctic ocean. *J. Geophys. Res.*, *112*(C04S04),  
 2216 doi:10.1029/2006JC003732.
- 2217 Zhao, M., Timmermans, M.-L., Cole, S., Krishfield, R. A., & Toole, J. M. (2016).  
 2218 Evolution of the eddy field in the Arctic Oceans Canada Basin, 20052015.  
 2219 *Geophys. Res. Lett.*, *43*, 8106–8114. doi: 10.1002/2016GL069671
- 2220 Zlotnicki, V., Qu, Z., & Willis, J. (2019). *MEaSURES gridded sea surface height*  
 2221 *anomalies version 1812. ver. 1812. PO.DAAC, CA, USA.* [https://doi.org/](https://doi.org/10.5067/SLREF-CDRV2)  
 2222 [10.5067/SLREF-CDRV2](https://doi.org/10.5067/SLREF-CDRV2). (Dataset Accessed: 2019-11-08) doi: 10.5067/SLREF  
 2223 -CDRV2
- 2224 Zweng, M. M., Reagan, J. R., Seidov, D., Boyer, T. P., Locarnini, R. A., Garcia,  
 2225 H. E., ... Smolyar, I. (2018). Volume 2: Salinity. In A. Mishonov (Ed.), .  
 2226 NOAA Atlas NESDIS 82, U.S. Government Printing Office, Washington, D.C.